

Aus der  
Klinik und Poliklinik für Strahlentherapie und Radioonkologie  
Klinikum der Ludwig-Maximilians-Universität München



# ***Technical Advances in Image-Guided Radiation Therapy Systems***

Dissertation  
zum Erwerb des Doktorgrades der Humanbiologie  
an der Medizinischen Fakultät der  
Ludwig-Maximilians-Universität München

vorgelegt von  
Vanessa da Silva Mendes  
aus  
Leiria, Portugal

Jahr  
2023

---

Mit Genehmigung der Medizinischen Fakultät der  
Ludwig-Maximilians-Universität zu München

Erster Gutachter: Prof. Dr. Guillaume Landry

Zweiter Gutachter: PD Dr. Christian Thieke

Dritter Gutachter: Prof. Dr. Falk Roeder

ggf. weitere Gutachter: \_\_\_\_\_  
\_\_\_\_\_

Mitbetreuung durch den  
promovierten Mitarbeiter: \_\_\_\_\_

Dekan: Prof. Dr. med. Thomas Gudermann

Tag der mündlichen Prüfung: 10.10.2023

## Affidavit



Promotionsbüro  
Medizinische Fakultät



### Affidavit

Da Silva Mendes, Vanessa

\_\_\_\_\_  
Surname, first name

\_\_\_\_\_  
Street

\_\_\_\_\_  
Zip code, town, country

I hereby declare, that the submitted thesis entitled:

### Technical Advances in Image-Guided Radiation Therapy

is my own work. I have only used the sources indicated and have not made unauthorised use of services of a third party. Where the work of others has been quoted or reproduced, the source is always given.

I further declare that the dissertation presented here has not been submitted in the same or similar form to any other institution for the purpose of obtaining an academic degree.

Munich, 19.10.2023

place, date

Vanessa Filipa da Silva Mendes

Signature doctoral candidate

## Table of content

<b>Affidavit .....</b>	<b>3</b>
<b>Table of content.....</b>	<b>4</b>
<b>List of abbreviations .....</b>	<b>5</b>
<b>List of publications .....</b>	<b>7</b>
<b>Your contribution to the publications .....</b>	<b>9</b>
1.1 Contribution to Paper I: Dosimetric comparison of MR-linac-based IMRT and conventional VMAT treatment plans for prostate cancer.....	9
1.2 Contribution to Paper II: ExacTrac Dynamic workflow evaluation: combined surface optical/thermal imaging and X-ray positioning .....	9
<b>2. Introduction .....</b>	<b>10</b>
2.1 Physical background of Photon External Beam Radiotherapy .....	13
2.1.1 Interaction of X-ray Photons with Matter.....	13
2.1.2 Energy Transfer, Deposition and Absorbed Dose .....	17
2.1.3 Medical Linear Accelerators.....	19
2.1.4 Treatment Planning.....	23
2.1.5 Photon Dose Calculation .....	28
2.2 Workflow in External Beam Radiotherapy .....	35
2.3 Basics in Medical Imaging .....	37
2.3.1 Kilovoltage X-rays .....	37
2.3.2 Clinical Computed Tomography .....	40
2.3.3 Magnetic Resonance Imaging .....	43
2.4 Image Guided Radiotherapy .....	48
2.4.1 IGRT techniques and ART.....	48
2.4.2 SRT, SRS and SBRT .....	51
2.4.3 MRIdian linac .....	51
2.4.4 ExacTrac Dynamic.....	53
<b>3. Summary.....</b>	<b>56</b>
<b>4. Zusammenfassung .....</b>	<b>58</b>
<b>5. Paper I: Dosimetric comparison of MR-linac-based IMRT and conventional VMAT treatment plans for prostate cancer .....</b>	<b>60</b>
<b>6. Paper II: ExacTrac Dynamic workflow evaluation: Combined surface optical/thermal imaging and X-ray positioning.....</b>	<b>74</b>
<b>7. Conclusions .....</b>	<b>92</b>
<b>References .....</b>	<b>94</b>
<b>Acknowledgements.....</b>	<b>99</b>
<b>Curriculum vitae .....</b>	<b>Fehler! Textmarke nicht definiert.</b>



## List of abbreviations

2D	two-dimensional
3D	three-dimensional
3D CRT	three-dimensional conformal radiotherapy
ART	adaptive radiation therapy
BED	biological effective dose
CBCT	cone beam computed tomography
CC	collapsed cone
CPE	charged particle equilibrium
CT	computed tomography
CTV	clinical target volume
DNA	deoxyribonucleic acid
DoF	degrees of freedom
DRR	digitally reconstructed radiograph
DVH	dose-volume histogram
EBRT	external beam radiotherapy
EPID	electronic portal imaging device
EXTD	ExacTrac Dynamic
FID	free induction decay
FFF	flattening filter free
GRE	gradient echo
GTV	gross tumour volume
HU	Hounsfield units
ICRU	International Commission on Radiation Units and Measurement
IGRT	image-guided radiotherapy
IMRT	intensity modulated
ITV	internal target volume
KERMA	kinetic energy released per unit mass
keV	kilo electron volt
KMC	Kawrakow Monte Carlo
kV	kilovolt
LINAC	linear accelerator
LQM	linear quadratic model

---

MC	Monte Carlo
MeV	mega electron volt
MLC	multileaf collimator
MR	magnetic resonance
MRgRT	magnetic resonance-guided radiotherapy
MRI	magnetic resonance imaging
MR-linac	magnetic resonance linear accelerator
MU	monitor units
MV	megavolt
NMR	nuclear magnetic resonance
NTCP	normal tissue complication probability
OAR	organ at risk
PB	pencil beam
PCa	prostate cancer
PET	positron-emission tomography
PTV	planning target volume
QA	quality assurance
RF	radio frequency
SE	spin echo
SGRT	surface-guided radiotherapy
SRS	stereotactic radiosurgery
SRT	stereotactic radiotherapy
TCP	tumour control probability
TERMA	total energy released per unit mass
TPS	treatment planning system
US	ultrasound
VMC	voxel-based Monte Carlo
VMAT	volumetric modulated arc therapy
WHO	World Health Organization
XVMC	X-ray voxel Monte Carlo

## List of publications

### Publications

**V. da Silva Mendes**, L. Nierer, M. Li, S. Corradini, M. Reiner, F. Kamp, M. Niyazi, C. Kurz, G. Landry, C. Belka: Dosimetric comparison of MR-linac-based IMRT and conventional VMAT treatment plans for prostate cancer. *Radiation Oncology*. 2021; 16:133

L. Nierer, C. Eze, **V. da Silva Mendes**, J. Braun, P. Thum, R. von Bestenbostel, C. Kurz, G. Landry, M. Reiner, M. Niyazi, C. Belka, S. Corradini. Dosimetric benefit of MR- guided online adaptive radiotherapy in different tumor entities: liver, lung, abdominal lymph nodes, pancreas and prostate. *Radiation Oncology*. 2022; 17:53

**V. da Silva Mendes**, M. Reiner, L. Huang, D. Reitz, K. Straub, S. Corradini, M. Niyazi, C. Belka, C. Kurz, G. Landry, P. Freisleder. ExacTrac Dynamic workflow evaluation: Combined surface optical/thermal imaging and X-ray positioning. *Journal of Medical Clinical Medical Physics*. 2022; e13754

D. Reitz, J. Muecke, **V. da Silva Mendes**, G. Landry, M. Reiner, M. Niyazi, C. Belka, P. Freisleder, S. Corradini. Intrafractional monitoring of patients using four different immobilization mask systems for cranial radiotherapy. *Physics and Imaging in Radiation Oncology* 2022; 134-139

### Talks

**V. da Silva Mendes**, ExacTrac Dynamic: Evaluation of a combined surface optical/thermal and X-ray monitoring and positioning system for cranial radiosurgery, *DGMP Jahrestagung 2022*

### Posters

P. Freisleder, **V. da Silva Mendes**, K. Straub, C. Belka, M. Reiner: Brainlab ExacTrac Dynamic – First pre-clinical validation of differences between surface guidance and X-ray based tracking. *DGMP Jahrestagung 2019*

**V. da Silva Mendes**, K. Straub, C. Belka, M. Reiner, G. Landry, P. Freisleder: Brainlab ExacTrac Dynamic – First pre-clinical validation of surface- and X-ray positioning accuracy. *ESTRO 2020*

**V. da Silva Mendes**, M. Reiner, S. Corradini, M. Niyazi, C. Belka, C. Kurz, G. Landry, P. Freisle-  
derer: Validation of optical surface/thermal imaging and X-ray positioning accuracy for SRS treat-  
ments. *ESTRO 2021*

**V. da Silva Mendes**, M. Reiner, S. Corradini, M. Niyazi, C. Belka, C. Kurz, G. Landry, P. Freisle-  
derer: Validation of positioning accuracy for cranial treatments: optical surface/thermal imaging  
and X-ray. *DGMP Jahrestagung 2021*

D. Reitz, J. Muecke, **V. da Silva Mendes**, G. Landry , M. Reiner, M. Niyazi, C. Belka, P. Freisle-  
derer, S. Corradini: Intrafractional monitoring of patients using four different immobilization mask  
systems for cranial radiotherapy. *ESTRO 2021*

## **Your contribution to the publications**

### **1.1 Contribution to Paper I: Dosimetric comparison of MR-linac-based IMRT and conventional VMAT treatment plans for prostate cancer**

For this study, the first author (=author of this thesis) is responsible for the manuscript draft, the design of the study and literature revision (together with authors Guillaume Landry and Christopher Kurz). The first author (=author of this thesis) implemented the full workflow, carried out all data preparation and treatment planning. The first author (=author of this thesis) performed data evaluation and statistical interpretation. The first author (=author of this thesis) wrote the final manuscript.

### **1.2 Contribution to Paper II: ExacTrac Dynamic workflow evaluation: combined surface optical/thermal imaging and X-ray positioning**

For this study, the first author (=author of this thesis) is responsible for the manuscript draft, the design of the study and literature revision (together with author Philipp Freisleder). The first author (=author of this thesis) implemented the full workflow, carried out all data preparation, which was also partly prepared by author Philipp Freisleder. The first author (=author of this thesis) performed data evaluation and statistical interpretation. The first author (=author of this thesis) wrote the final manuscript.

## 2. Introduction

Cancer is characterised as a leading cause of death worldwide impairing life expectancy in every country in the world [1]. According to World Health Organisation (WHO) estimates in 2019, cancer is considered the first or second leading cause of death before the age of 70 in 112 of 183 countries [2]. In Europe, cancer is a major public concern since almost one-quarter of all global diagnosed cancer cases occur in this continent, even though it is home to only one-tenth of the world's population [3].

Every type of cancer requires a specific treatment, which depends on its type and stage, either to cure or to prolong the life of the patient as well as to improve quality of life. The three major types of treatments typically adopted in modern oncology are surgery, radiotherapy and chemotherapy, and they are either applied individually or more often in combination. Other less common approaches for cancer treatment are immunotherapy, epigenetic therapy or hormone therapy, nowadays very common for breast and prostate cancer [4].

Radiotherapy can be divided into brachytherapy, where radioactive sources are introduced into the patient, and external beam radiation therapy (EBRT), which refers to therapy delivered by an external radiation source, positioned at a certain distance from the body. Radiotherapy enables the treatment of abnormalities inside the body without a surgical procedure, allowing the possibility of a localised treatment of the tumour, in opposition to chemotherapy. A basic goal of this therapy is the use of ionising radiation (highly energetic photons, electrons, ions) and the consequent deposition of energy in human tissue, leading to the damage of the deoxyribonucleic acid (DNA) strands of the tumour cells, in turn leading to cell division failure. Radiotherapy aims at minimising the amount of radiation absorbed in adjacent healthy organs at risk (OAR). Sparing healthy tissue and critical structures can be performed by shaping the beam with a multileaf collimator (MLC), a device with up to 160 movable leaves of a radiation absorbing material, which can move nearly independently to form arbitrary apertures.

Conventional 3-dimensional conformal radiotherapy (3D CRT) is based on 3D anatomical information. In 3D CRT clinicians design and deliver treatment plans with several beams, whose shape adjusts as closely as possible to the planning target volume (PTV), aiming to deliver sufficient dose to the tumour and as little dose as possible to the surrounding normal tissues [5]. This technique is based on “forward treatment planning” and the treatments are delivered with a flattened beam with uniform intensity across the fields. These are delivered using several treatment beam angles, shaped to the form of the tumour.

Intensity-modulated radiotherapy (IMRT) is a type of radiation therapy and refers to a technique that evolved from 3D CRT. In this technique, the treatment plan is delivered from different directions (beams), divided in several segments [5]. Multiple small MLC apertures are created and added up from a certain direction, enabling the delivery of more than two intensity levels from a single beam direction and the non-uniform fluences, after being optimised, result in a final dose delivered to the tumour [6]. IMRT is based on “inverse treatment planning”, the final dose is calculated according to the introduced constraints and objectives, enabling the creation of more complex dose distributions with concave and convex shapes, and therefore critical OARs can be better spared [5, 7].

As a high-precision technique with a higher level of complexity, IMRT is relatively intolerant to patient setup uncertainties and anatomical variations, which can cause large variations in the

dose distribution, warranting periodic image-guidance [6, 8-10]. Image-guided radiotherapy (IGRT) is a method that uses imaging before and/or during treatment and its main goal is to guarantee an accurate and safe clinical application of the modern radiotherapy techniques [8]. It is therefore an essential component of modern radiation therapy, since it enables not only the adjustment of the patients' daily positioning before the start of the treatment, but it also provides monitoring of inter- and intra-fractional motion. Thus, knowledge of the organs' and targets' shapes, as well as their position, can be taken into consideration during treatment delivery [10].

The information provided by IGRT techniques can also be included into the plan and dose-delivery optimisation during the cycle of treatment. Hence, the treatment plan is adjusted to the anatomy of the day, guaranteeing that the patient can be irradiated as precisely and accurately as it was previously planned when delivering the baseline plan [11]. This process is named "adaptive radiation therapy" (ART) and, even though it is not state of the art, it is very important, especially when internal organs' and the tumour's motion, which represent a major concern, is to be considered. Currently, the adaptive workflow has been more often employed since the magnetic resonance-linear accelerator (MR-linac) was clinically introduced, taking advantage of the improved soft tissue contrast shown by the MR images. The MR-linac is a hybrid system, integrating a conventional linac with an MR scanner to perform MR-guided radiotherapy (MRgRT). Currently, both a low-field (0.35 T) MR-linac (ViewRay MRIdian ViewRay Inc., Oakwood Village, OH, USA), with the possibility of automated beam gating, as well as a high-field (1.5 T) MR-linac (Elekta Unity, Elekta AB, Stockholm, Sweden) are clinically available [12, 13]. Gating techniques are strategies routinely used by the implementation of different systems, such as real-time imaging (e.g. 2D cine sagittal MR images in the Viewray MRIdian linac), pressure systems that detect respiratory motion (e.g. Anzai belt) or surface monitoring (e.g. Catalyst system) [14]. When this technique is implemented, the treatment beam is only turned on during previously determined motion phases or when a previously defined part of the tumour (or a surrogate) is in a certain defined position.

Due to the implementation of the most recent IGRT techniques, radiotherapy has seen a significant improvement in the dose delivery accuracy, allowing for both clinical target volume (CTV) to PTV margin optimisation and dose escalation, enabling the surrounding healthy tissue to be better spared [8, 10, 15]. Imaging methods can be separated into ionising radiation- and non-ionising radiation- based systems and static or real time imaging. Transabdominal ultrasound (US), electromagnetic transponders, surface imaging and magnetic resonance imaging (MRI) systems are non-radiation-based systems, whilst cone beam computed tomography (CBCT) or stereoscopic X-ray imaging are two systems that make use of ionising radiation [8].

Without image guidance and thus, without accounting for geometric variations that can impact the treatment, the patient can be subjected to inappropriate radiation exposure and therefore receive less efficient therapy [10].

The Viewray MRIdian MR-linac and the ExacTrac Dynamic (EXTD) (Brainlab AG, Munich, Germany), two systems of interest in the current work, both represent good examples of innovative clinical technology, where different IGRT strategies are implemented:

- At the MRIdian improved treatment position verification, as well as a reduction of the target margins are enabled by ART, exploiting the improved soft tissue contrast of MRI, and target monitoring during treatment, with no extra dose delivered to the patient. Here

mainly tumours located in the abdominal and thoracic regions are treated, where organ motion is more pronounced [16];

- The EXT-D system is used for patient setup and monitoring in the radiotherapy environment, as an additional system to standard linacs, via optical/surface imaging and stereoscopic X-ray imaging. This system is mostly suitable when treating intracranial tumours or tumours in bony structures. However, the monitoring of the patient in real-time, the detection and compensation for intra-fraction tumour motion, also in extracranial regions, whether induced by patient movement or breathing, are also possible with this system [17].

Both systems, MRIdian and EXT-D, encompass complex sub-systems, whose performance need to be investigated individually as well as a whole, in order to guarantee a precise and accurate delivery of a radiotherapy treatment.

In this thesis, the equivalence of MRIdian dose distributions, when using a special double-stack MLC and in the presence of a low magnetic field (0.35 T), to those obtained with conventional linacs was verified. The study led to the conclusion that, under similar conditions, with the MRIdian system it is possible to generate prostate cancer treatment plans of similar dosimetric quality as conventional linac-based VMAT plans. Moreover, due to the PTV margin reduction enabled by online MR image guidance, a better sparing of the surrounding tissues and organs at risk (OARs) can be achieved.

In the second part of this thesis, the performance of the EXT-D system concerning positioning accuracy was investigated, including evaluations at the level of the different subcomponents. The experiments that this positioning and monitoring system was subjected to, showed that it was possible to efficiently and accurately position radiotherapy patients as well as monitor them throughout each treatment. Several systems were involved in the measurements, i.e. optical/thermal- and stereoscopic X-ray imaging, as well as CBCT and megavolt (MV) portal imaging. When analysing the results, it was concluded that the discrepancies between all systems were always below 1 mm, for both coplanar and non-coplanar couch angles. An advantage presented by the EXT-D system is that it can be used to both position and monitor the patient, for all couch angles, in opposition to CBCT that can only position correctly the patient before the treatment starts, and only when the treatment couch is at couch 0°.

The thesis is divided into the following chapters: in chapter 2.1, a general overview of the technological and physical background of external beam photon radiotherapy is provided, describing the generation of the high-energy photon beams in medical linear accelerators (linacs), including the interaction of X-ray photons with matter and how the dose is absorbed. The treatment planning process is also summarised as well as photon dose calculation methods. In chapter 2.2 the workflow in EBRT is described, starting from patient immobilization until when the patient treatment takes place. The “Quality Assurance and Verification” process is also described. Chapter 2.3 gives an overview of medical imaging relevant for IGRT and chapter 2.4 focusses on specifics of IGRT.

In chapter 7, the main research findings are summarised, and future perspectives are discussed.



## 2.1 Physical background of Photon External Beam Radiotherapy

### 2.1.1 Interaction of X-ray Photons with Matter

Radiation is categorised as non-ionising and ionising, depending on its ability to remove electrons from atoms or molecules.

Ionising radiation can be divided into directly and indirectly ionising forms, both of which are used in radiotherapy. The DNA molecules are the most sensitive cell components to irradiation, and thus the DNA of malignant cells represents the critical target. Directly ionising radiation refers to charged particles, such as electrons, protons, heavy ions,  $\alpha$  and  $\beta$  particles, which deposit energy in the medium through direct Coulomb interactions between the directly ionising charged particle and orbital electrons of atoms in the medium [18]. Indirectly ionising radiation refers to neutral particles, namely photons and neutrons. Energy deposition in the medium occurs in two-steps: in the first step, a charged particle is released in the medium, e.g. for primary photons mostly secondary electrons are released. After that, these secondary charged particles ionise many other atoms depositing energy in the medium through Coulomb interactions [18]. Ionising photon radiation used in radiotherapy comes either from the decay of radioisotopes, which emits gamma rays; or from the deceleration of electrons directed into a high density target, producing X-rays by the bremsstrahlung interaction (bremsstrahlung photons). Currently in radiotherapy, high-energy photon beams are most commonly generated by a medical linac, which is also the technology of interest in this work and therefore a more detailed description will follow in section 2.1.2.

Photon beams are primarily described by the number and energy of photons, as well as their direction of travel. Of main interest in radiotherapy is the amount of energy deposited in a medium (air, water, biological tissue) by a photon beam. In order to describe an ionising radiation beam leaving a medical linac, there are certain quantities and units that need to be defined, such as photon fluence and energy fluence.

The *photon fluence*,  $\Phi$  ( $\text{cm}^{-2}$ ), is defined as the quotient  $dN$  by  $dA$ , where  $dN$  is the number of photons that enter an imaginary sphere of cross-sectional area  $dA$ :

$$\Phi = \frac{dN}{dA} \quad (1)$$

The *energy fluence*,  $\Psi$  ( $\text{MeV} \cdot \text{cm}^{-2}$ ), describes the energy flow in a photon beam and is defined as the amount of energy  $dE$  crossing a unit area  $dA$ . The energy fluence can also be calculated from  $\Phi$  (assuming a monoenergetic photon beam);  $dN$  represents the number of photons with energy  $E$ :

$$\Psi = \frac{dE}{dA} = \frac{dN}{dA} E = \Phi E \quad (2)$$

Almost all realistic photon beams are polyenergetic and therefore the equations above need to be replaced by photon fluence spectrum and energy fluence spectrum, defined respectively by:

$$\Phi_E(E) = \frac{d\Phi}{dE}(E) \quad (3)$$

and

$$\Psi_E(E) = \frac{d\Psi}{dE}(E) = \frac{d\Phi}{dE}(E)E \quad (4)$$

where  $\Phi_E$  and  $\Psi_E$  are notations for photon fluence spectrum and the energy fluence spectrum differential in energy  $E$ , respectively [18].

The inverse square law governs a photon beam propagating through vacuum at distances where the source can be considered point-like, meaning that the photon fluence is inversely proportional to the square of the distance from the photon beam source [18]. However, when the photon beam enters any medium, it is not only affected by the inverse square law but also by the attenuation and scattering inside the medium (e.g. a patient or a phantom), causing a decrease of the particle number in the beam. The number of photons  $dN$  that reach a point behind a thickness of material  $dx$ , is proportional to the number of incident photons  $N(x)$  at depth  $x$  and the thickness of the absorber medium. The constant of proportionality is the *linear attenuation coefficient*  $\mu$ , that is the fraction of the beam intensity that is absorbed or scattered per unit thickness, describing how easily a certain material can be penetrated by a beam of photons [19]:

$$dN = -\mu \times N(x) dx \quad (5)$$

The following equation describes the attenuation of the intensity of the beam when passing through a certain material, where  $N(x)$  refers to the number of primary photons transmitted through the absorber. This equation shows that the intensity of the photons declines exponentially [19]:

$$N(x) = N_0 \times e^{-\mu x} \quad (6)$$

where  $N_0$  denotes the number of photons at  $x = 0$ , the incident photons.  $\mu$  depends on photon beam energy and characteristics of the medium such as its atomic number  $Z$  and density  $\rho$ . However, the dependency on the density can be removed by division of  $\mu$  by  $\rho$ , resulting in the mass attenuation coefficient  $\frac{\mu}{\rho}$ .

Photon interactions with matter are stochastic by nature and the probability of an interaction depends on the energy of the photon  $h\nu$  and the atomic number of the medium  $Z$ , which can be expressed in terms of a cross-section  $\sigma$ . The total cross-section can be written as the sum of the cross-sections of the different photon interactions: coherent (Rayleigh) and incoherent (Compton) scattering, photoelectric effect, pair and triplet production and photonuclear interactions.

Nevertheless, only three types of interaction are dominating in radiation oncology and medical X-ray imaging, with photon energies between approximately 25 keV (mammography) up to 25 MeV (EBRT) (see Figure 2.1.1).

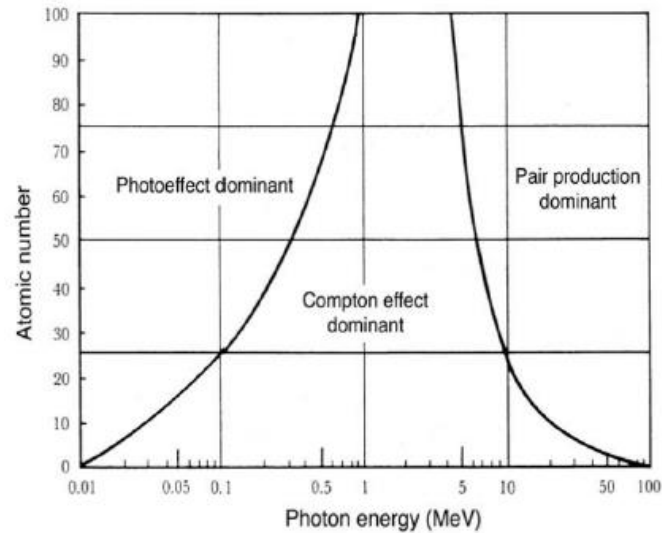


Figure 2.1.1: The main processes among interactions of photons with matter in relation to the atomic number, within the diagnostic and radiotherapy energy range. At low energies the photoelectric effect dominates, at intermediate energies the Compton effect and pair production at higher energies [18]. Figure reproduced with permission by the I.A.E.A.

### The photoelectric effect:

A photoelectric interaction happens when  $E_\gamma$ , the energy of the incoming photon  $h\nu$  is fully absorbed by the atom and transferred to an orbital electron of an inner shell. Consequently, an electron is ejected with a kinetic energy  $E_{\text{kin}}$ , that can be calculated by:

$$E_{\text{kin}} = h\nu - E_b \quad (7)$$

with  $E_b$  as the binding energy of the electron (see Figure 2.1.2, on the left-hand side). The ejected atomic electron creates a vacancy in the atomic shell. This vacancy must be filled by an electron from one of the outer shells, leading to an energy loss ( $\Delta E$ ) in the form of characteristic X-rays, or by emission of monoenergetic Auger electrons (see Figure 2.1.2, on the right-hand side).

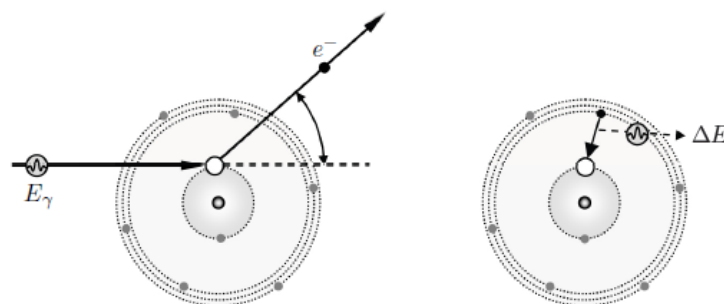


Figure 2.1.2: Diagram illustrating the photoelectric effect [20]. Figure reproduced with permission by Springer Nature.

For energies around and below 0.1 MeV the following equations demonstrate the relationship between mass attenuation coefficient and the energy of the incident photon, for high and low atomic numbers, respectively:

$$\left(\frac{\mu}{\rho}\right)_{\text{Photoelectric}} \propto \frac{Z^3}{E_\gamma^3} \quad (8)$$

$$\left(\frac{\mu}{\rho}\right)_{\text{Photoelectric}} \propto \frac{Z^{3.5}}{E_\gamma^3} \quad (9)$$

### (Incoherent) Compton Scattering:

Compton scattering happens when the incident photons interact with outer shell electrons. The incoming photon transfers part of its energy and momentum to the electron and the resulting photon, less energetic, is deflected. For Compton scattering to occur, the incoming photon's energy must be much larger compared to the electron's binding energy, so that the electron can be assumed as a free electron. Hence, this interaction yields a scattered photon, under an angle  $\theta$ , and an electron, ejected from the atomic shell with kinetic energy,  $E_{\text{kin}}$  (Compton electron) (see Figure 2.1.3).

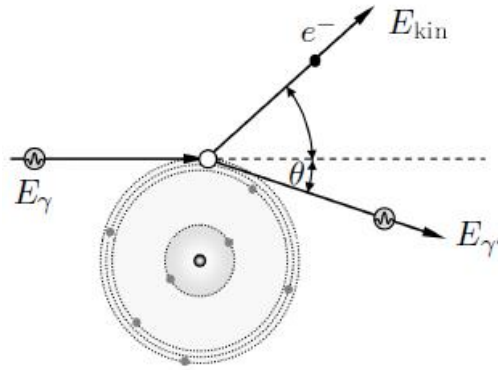


Figure 2.1.3: Diagram illustrating the Compton effect [20]. Figure reproduced with permission by Springer Nature.

The energy of the scattered photon  $E_{\gamma'}$  can be calculated by use of energy and momentum conservation as a function of the initial photon energy  $E_\gamma$ , the photon scattering angle  $\theta$  and the rest energy of the electron  $m_e c^2$ :

$$E_{\gamma'} = \frac{E_\gamma}{1 + \frac{E_\gamma}{m_e c^2} (1 - \cos(\theta))} \quad (10)$$

The kinetic energy transferred to the electron can be calculated as

$$E_{\text{kin}} = E_\gamma - E_{\gamma'} - E_b \quad (11)$$

where  $E_\gamma$  is the incident photon's initial energy,  $E_{\gamma'}$  is the remaining photon energy and  $E_b$  the electron's binding energy. Nevertheless,  $E_b$  is considered small when comparing to  $E_\gamma$  and  $E_{\gamma'}$ , and therefore can usually be neglected.

The mass attenuation coefficient  $\frac{\mu}{\rho}$  associated with Compton scattering is inversely proportional to the photon energy and can be approximated as

$$\left(\frac{\mu}{\rho}\right)_{\text{Compton}} \propto \frac{Z}{A} \frac{1}{E_\gamma} \quad (12)$$

for photon energies between 0.2 MeV and 10 MeV, where  $Z$  is the atomic number,  $A$  the atomic mass number (see Figure 2.1.3).

### Pair Production:

Photons can also interact with the electrical field of a nucleus. In case the energy of the incident photon exceeds  $2m_e c^2 = 2 \times 511 \text{ keV} = 1.022 \text{ MeV}$ , it can be absorbed and produce an electron-positron pair, with a maximum energy of  $E_{kin} = E_\gamma - 1.022 \text{ MeV}$  shared by the electron and the positron (see Figure 4.1.4).

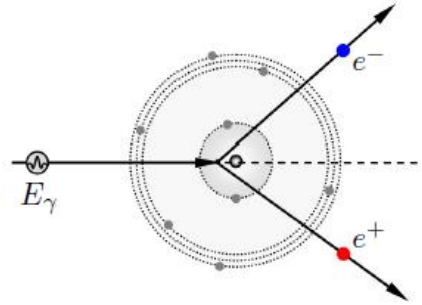


Figure 2.1.4: Diagram illustrating the pair production in the nuclear Coulomb field [20]. Figure reproduced with permission by Springer Nature.

The mass attenuation coefficient  $\frac{\mu}{\rho}$  associated with the pair production can be approximated as

$$\left(\frac{\mu}{\rho}\right)_{\text{pair}} \propto \frac{Z^2}{A} \log E_\gamma \quad (13)$$

### 2.1.2 Energy Transfer, Deposition and Absorbed Dose

In a beam of photons interacting with matter, their energy is transferred in a two-steps process: in the first step, a partial or complete energy transfer from the primary indirectly ionising radiation (photons) to secondary ionising radiation (electrons) occurs through the interactions described above. The energy transfer occurring in this first step is called KERMA, which stands for kinetic energy relaxed per unit mass [18].

Total KERMA can be divided into collision KERMA  $k_{col}$  and radiative KERMA  $k_{rad}$ . Collision KERMA  $k_{col}$  results in the production of electrons, which release their energy through ionisation and excitation processes because of the interaction of the charged particles (electrons) with the atomic electrons [19, 21]. Radiative KERMA  $k_{rad}$  results in the production of radiative photons

caused by the interaction between the charged particles (electrons) and the atomic nucleus (bremsstrahlung, electron-positron annihilation in flight and characteristic radiation) [19, 21]. KERMA is defined as the mean sum of all kinetic energy transferred from photons to electrons  $d\bar{E}_{tr}$  in a mass  $dm$  of a medium:

$$K = \frac{d\bar{E}_{tr}}{dm} = \Psi \left( \frac{\mu_{tr}}{\rho} \right) \quad (14)$$

where  $d\bar{E}_{tr}$  is the average energy transmitted to electrons as kinetic energy per interaction. The energy transfer coefficient  $\mu_{tr}$  describes the portion of photon energy that is transferred into kinetic energy of electrons per unit thickness of absorber/medium and it is related to  $\mu$  and  $h\nu$  of the photon beam by the following equation:

$$\mu_{tr} = \frac{\bar{E}_{tr}}{h\nu} \mu \quad (15)$$

The mass energy transfer coefficient is given by  $\frac{\mu_{tr}}{\rho}$ , where  $\rho$  is the density of the medium, and closely related to KERMA [5].

In the second stage, the kinetic energy from the secondary electrons is partly imparted to the medium through atomic excitations and ionisation events, which results in the absorbed dose  $D$ . The product of energy transfer coefficient  $\mu_{tr}$  and  $(1 - g)$  determines the energy absorption coefficient  $\mu_{en}$ .  $g$  is the fraction of the kinetic energy lost to photons as the secondary electrons slow down completely. This energy dissipates in the form of radiative losses such as bremsstrahlung, electron-positron annihilation in flight and characteristic radiation [19]:

$$\mu_{en} = \mu_{tr}(1 - g) \quad (16)$$

Similarly to  $\frac{\mu_{tr}}{\rho}$ , the mass energy absorption coefficient is given by  $\frac{\mu_{en}}{\rho}$ , which relates to dose, that is the energy absorbed per unit mass of the medium [5].

The energy transferred in a photon interaction to kinetic energy of secondary ionising particles (electrons) is of significant interest in dosimetry as the electrons have a rather small range and therefore they will impart their energies near to where they were released.

The absorbed dose quantifies the mean energy deposited per unit mass  $m$  in a finite volume  $V$ , defined by:

$$D = \frac{d\bar{E}}{dm} \quad (17)$$

and is responsible for the damage of tumour cells but also of other tissues.

In radiotherapy, KERMA is an important quantity due to the similarity to absorbed dose. Both share the same unit ( $Gy = J/Kg$ ), but they are not exactly the same. They differ mostly for high energy photons, since a higher amount of energy is transferred to the electrons and therefore they can travel larger distances and deposit energy in the medium along their track. This means that the absorption of energy does not occur at the same location as the transfer of energy (collision KERMA) [18]. However, when the number and energy distribution of electrons entering and

exiting a certain volume is equal, the so-called *charged particle equilibrium* (CPE), collision KERMA and absorbed dose are considered to be the same.

### 2.1.3 Medical Linear Accelerators

In modern radiotherapy, linear accelerators have become the most widely used machines for patient treatment. Figure 2.1.5 shows a scheme of the components of a standard linac.

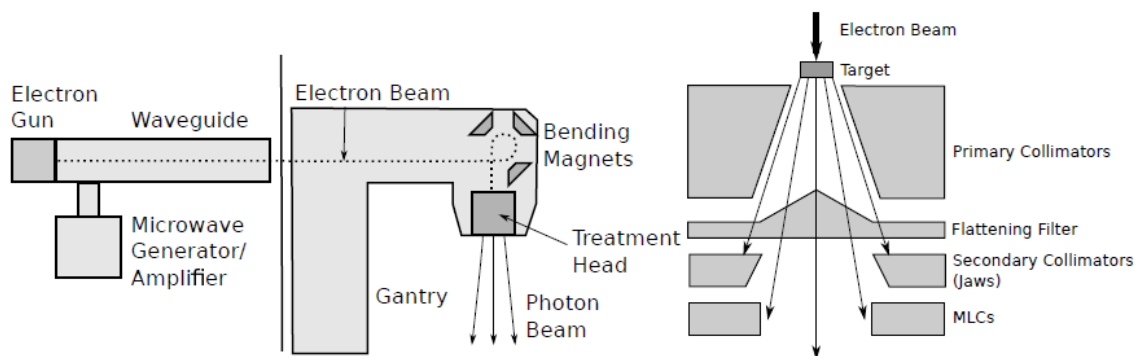


Figure 2.1.5: Scheme of a standard linac [22].

Medical linacs are used to produce a consistent stable mono-energetic and high-current electron beam, which serves to produce an X-ray beam. The linacs are commonly composed of an electron gun, an accelerating waveguide, a radio-frequency (RF) generator or amplifier (a magnetron or a klystron), a beam transport system and a beam collimation and monitoring system.

Electrons are produced in the injection system, known as “electron gun”, and then injected into the waveguide to be accelerated. The electrons are accelerated by an oscillating electric field, provided by an RF generator (typically a magnetron, or less commonly a klystron) and a pulsed modulator.

In standard medical linacs, while the waveguide is usually located in the gantry arm, the radiation beam is emitted from the treatment head in an approximately perpendicular direction relative to the waveguide, towards the isocentre. Due to the patient position and the limitation of gantry size, it is necessary to bend the electron beam, before it interacts with the X-ray target, using bending magnets. The treatment head comprises various elements that form the X-ray’s beam geometry, as well as monitoring devices. Among the components are an X-ray target, a flattening filter, ion chambers and collimators.

The electron beam itself can be used to treat patients with superficial lesions. However, most lesions are situated deeper inside the patients’ body. In order to treat these kind of lesions, a photon beam is necessary. The conversion of an electron beam into a photon beam is achieved by the use of the X-ray target, placed in the beamline. This component consists of a metal with a high atomic number  $Z$ , such as gold or tungsten [23, 24]. When the electron beam collides with the X-ray target, bremsstrahlung photons are produced, traveling mostly in forward direction.

Directly below the target there is a primary collimator, whose intent is to confine the beam and define the maximum beam size delivered by the linac, preventing leakage of radiation. The primary collimator is followed by a flattening filter, which is used to flatten the beam and create uniform dose profiles. The linac can also operate in a flattening filter free (FFF) mode, achieving increased dose rates and reducing treatment times, usually used for stereotactic treatments. The ionisation chambers are located below, monitoring the dose rate, the beam symmetry and beam homogeneity while the treatment is being delivered.

The beam is shaped by movable jaws and collimators, before it reaches the patient. The treatment head is mounted on the gantry, which can rotate 360° around one axis. The treatment beam direction is always perpendicular to the rotation axis and intersect in the isocentre, independently of gantry and collimator angles (within a certain tolerance). Moreover, the couch can be rotated around the isocentre, in order to place the patient in the desired position.

Figure 2.1.6 shows a schematic drawing of one the linacs used in this work, an Elekta Versa HD, where the most important components are depicted.

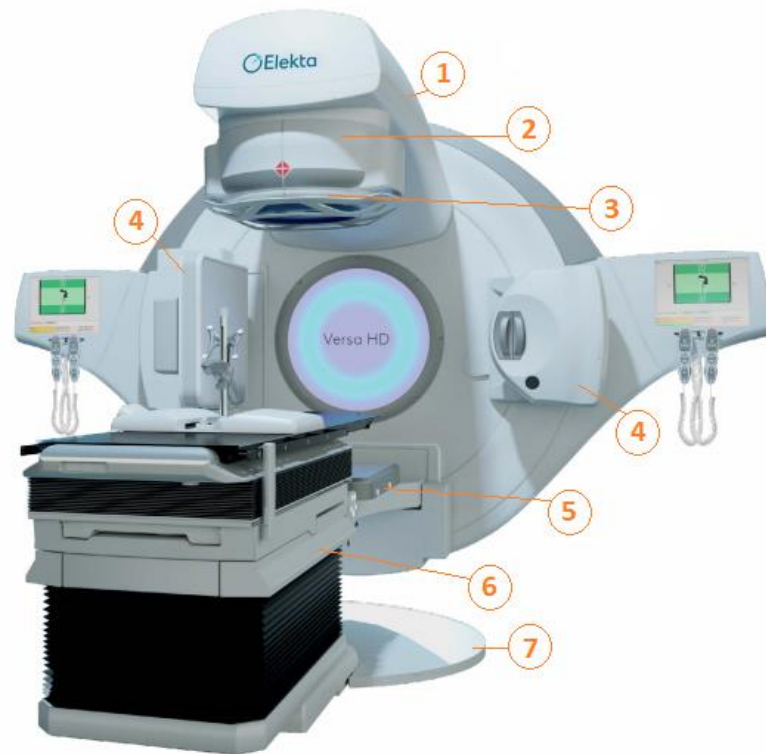


Figure 2.1.6: Design of an Elekta Versa HD linac: 1) rotating gantry, 2) treatment head, 3) MLC, 4) XVI imaging system – kV source and flat panel, 5) iView imaging system - MV panel, 6) treatment couch, 7) turntable [25]. Figure reproduced with permission by Elekta AB, Stockholm, Sweden.

Accurate planning and delivery of 3D CRT and IMRT treatments is highly dependent on the MLC available on the linac and is therefore important for our dosimetric comparison of MRIdian-based IMRT- and conventional VMAT treatment plans. The MLC installed on the Elekta Versa HD linac is the Agility MLC, with 160 tungsten alloy leaves, and a projected leaf-width in the isocentre of 5 mm (see Figure 2.1.7). The MLC is located below the Y-Jaws and its leaves are mounted on two



dynamic leaf guides, so that the leaves can be moved individually and the dynamic leaf guides are moveable as well, extending the movement range of the leaves and allowing overtravel by up to 15 cm [26]. The capability of interdigitation also enables the possibility to treat multiple small field openings together within one segment [27]. In order to optimise the penumbra for all possible leaf positions, the leaf edges are curved. Additionally, the vertical surface of the leaves is tilted, according to the divergence of the beam and also to minimise inter-leaf leakage, replacing a tongue-and-groove design of the leaves [28].

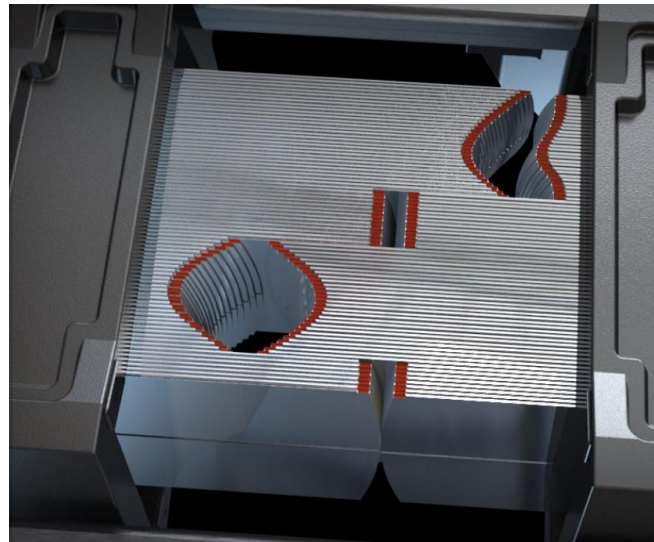


Figure 2.1.7: Field geometry with the Agility MLC [29]. Figure reproduced with permission by Elekta AB, Stockholm, Sweden.

The MRIdian linac combines a linac mounted on a gantry and a low-field MR scanner (0.35 T) for MR-guided radiotherapy (MRgRT), differing from a standard linac's configuration.

A schematic drawing of the 0.35 T MR-linac is shown in Figure 2.1.8, depicting the main hardware elements, such as the radiation gantry ring, the super-conducting double-toroid magnet and the treatment couch. Moreover, in Figure 2.1.9 linac components mounted upon the circular gantry assembly are presented.

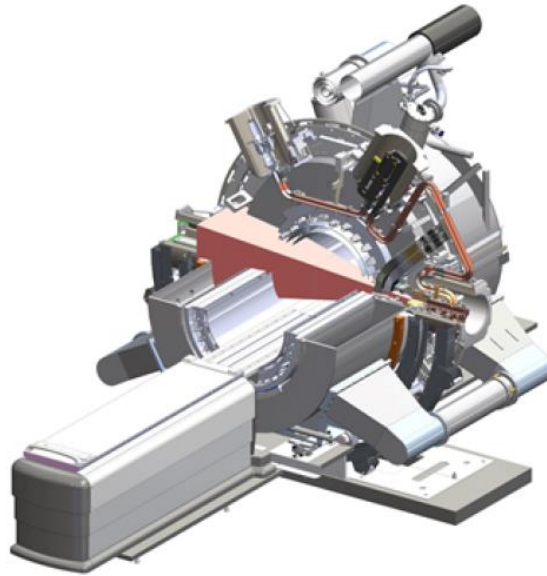


Figure 2.1.8: Schematic drawing of the MRIdian linac [30]. Figure reproduced with permission by Viewray Inc.

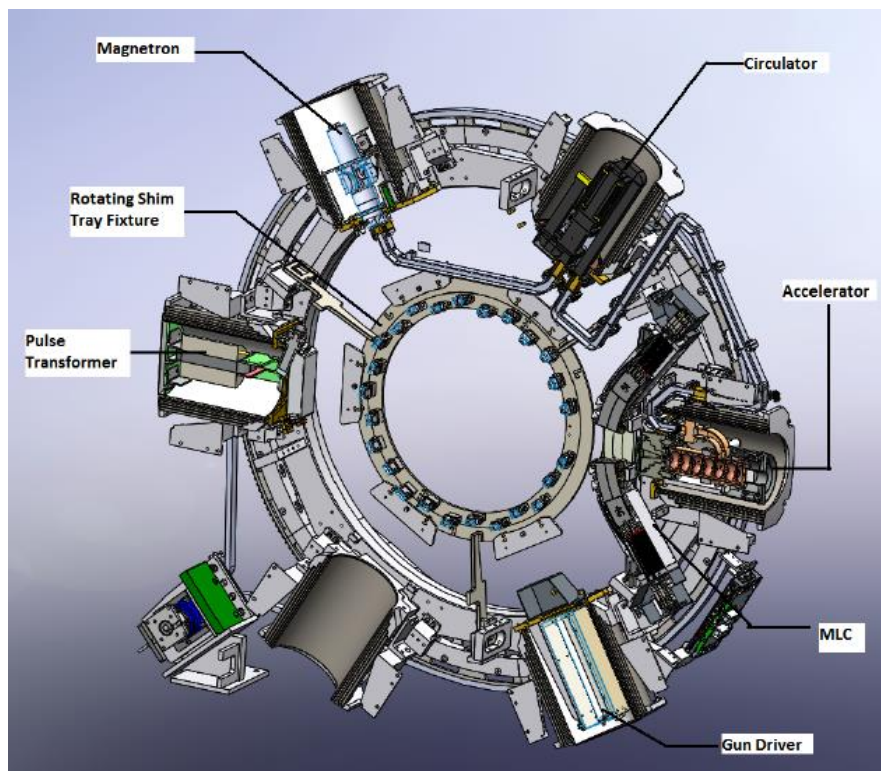


Figure 2.1.9: Simplified scheme of the rotating gantry including linac components and MLC [30]. Figure reproduced with permission by Viewray Inc.

The MR scanner consists of a 0.35 T split coil superconducting magnet with a 28 cm space between the two halves, where the radiation gantry ring is built. The linac itself and the linac components, such as the magnetron, the pulse transformer, the gun driver, are mounted on the gantry inside shielding compartments. These shielding compartments consist of concentric ferromagnetic cylinders used to avoid the interference of the static magnetic field with the operation of the

linac [31]. Nevertheless, these compartments have also another important purpose, which is preventing RF emissions, generated because of linac operation, from disturbing the quality of MR images. Several layers of RF absorbing carbon fibre and RF reflecting copper allow for RF shielding to be performed [31].

The radiation gantry ring provides structural support for the shielding compartments, their contents and the MLC, and can rotate 360° around the patient during treatment delivery. The pulsed electron beam is generated in the electron gun, the magnetron is used as an RF source to accelerate the electrons in the resonating cavity. Contrarily to a standard linac, the MR-linac has an MV beam line that is directed to the patient and does not need to be bent. For this reason, there are no adjustable bending magnets. The high energy electrons are directed at a tungsten target, generating a more intense photon beam in the centre, due to the absence of a flattening filter, shaped by a double-stacked and double-focused MLC and converging in the isocentre [30]. The MLC consists of two banks, with 138 tungsten leaves and a total leaf height of 11 cm, and each bank is divided in half along the direction of leaf travel, arranged in a stacked configuration (see Figure 2.1.10) [30]. The leaf sides are flat as they move on a divergence compensated trajectory (contrarily to most leaf edges, which present a rounded design). The width of a single leaf is 8.3 mm at the isocentric plane and as the two MLC stacks are shifted against each other by half a leaf width, it results in an effective leaf width of 4.15 mm at the isocentric plane, one half the physical leaf width [31]. Since the leaf layers are offset in the leaf-side direction, it eliminates the need of the “tongue and groove” mechanism [30, 32]. Similar to the Agility MLC, full interdigitation and overtravel are possible [31]. The minimum and maximum field size are  $0.2 \times 0.415 \text{ cm}^2$  and  $27.4 \times 24.1 \text{ cm}^2$ , respectively, and the collimator is permanently at 0°.

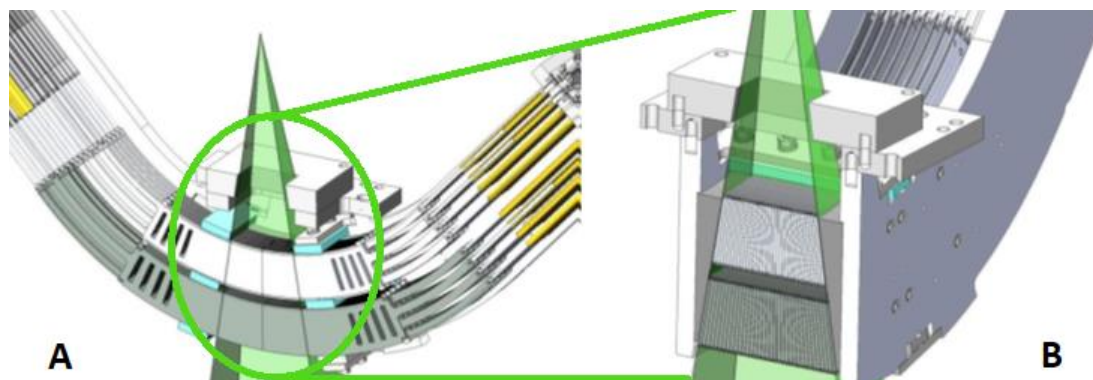


Figure 2.1.10: Schematic drawing of the MLC installed in the MRIdian linac: (A) view of the fully upper and lower opposing leaf stacks; (B) cross-sectional view of the MLC leaf stacks [32]. Figure reproduced with permission by Viewray Inc.

### 2.1.4 Treatment Planning

In radiotherapy, treatment planning is the process in which several teams, such as radiation oncologists, radiation therapists and medical physicists work together in order to create a treatment plan with the most appropriate radiotherapy technique to treat the patient.

The planning process can be divided into several procedures:

- Acquisition of the computed tomography (CT) scan;
- Definition of the target volume and the OARs;
- Definition of the treatment technique;
- Treatment plan optimisation using dose calculation;
- Visualisation and evaluation of dose distributions.

The treatment planning process begins with the acquisition of a CT scan, also denominated planning CT. The CT image plays a very important role in not only tumour (or lesion) identification, localisation and delineation, but it is also fundamental for the calculation of the final dose to be delivered during the treatment, as well as its distribution. This is done via conversion of the kilovoltage X-ray photon linear attenuation coefficient provided by the CT scan to relative electron density for dose calculation.

The delineation of the regions of interest, which include tumour and surrounding OARs, is usually performed on the planning CT as the primary imaging modality. Nevertheless, other functional and/or anatomical imaging modalities, such as MRI, US or positron emission tomography (PET) are also used to complement the anatomical information provided by the CT images and therefore to help improving precision in delineation of the relevant patient structures.

Both the ICRU reports 50 and 62 standardised the nomenclature used for treatment planning and are currently considered as the standard in radiation treatment planning, defining the anatomically based terms gross tumour volume (GTV), clinical tumour volume (CTV) and planning target volume (PTV), as well as the treated volume and the irradiated volume (see Figure 2.1.11) [33].

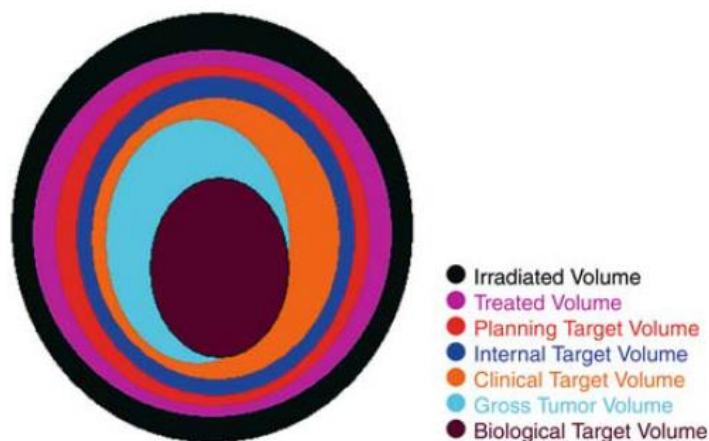


Figure 2.1.11: Concepts used in target volume definition for radiation treatment [33]. Figure reproduced with permission by Springer Nature.

The GTV, whose delineation is usually derived from data obtained from CT and MRI, contains the visible, macroscopic tumour volume to be treated and it is of major importance as in many cases the gross tumour tissue is irradiated with higher doses [33].

The CTV, on the other hand, is usually constituted by the GTV and a margin added to take into account the probable surrounding microscopic tumour infiltration. In some occasions, the CTV can be defined however without the presence of a GTV, such as in a regional lymph node, where there is no obvious GTV [34].

The internal target volume (ITV) was first introduced by the ICRU 62 and it includes the GTV/CTV and additionally internal margins of GTV/CTV created to take into account possible physiological movements of organs and/or cancerous tissue, such as respiration, pulsation, filling of the rectum, or changes of tumour size or shape [33]. Another margin is then added, either to the CTV or to the ITV, to create the PTV, to account for systematic and random errors and uncertainties in patient positioning during radiotherapy, which can happen within one fraction or between fractions. These margins (especially the one that creates the PTV) should ideally reflect the geometrical uncertainty of the target localisation. Movements to the GTV/CTV within the PTV should not induce any change to the delivered radiation dose to those structures. The amount of radiation dose is usually prescribed to the PTV structure to ensure that the irradiated dose is delivered to the CTV and/or to the GTV. The margins applied depend on the treatment technique and the clinical protocols used, as well as on image guidance [33].

The OARs are anatomical structures, located near the target volume and need to be spared from radiation so that their functional attributes are not lost. The corresponding contours are delineated on the planning CT, so that the dose to be delivered to these structures can be quantified and evaluated. The OARs can be in three distinct situations, which have to be considered in the treatment planning: they can be either located at a certain distance from the PTV, close to the PTV or be part of the PTV. In case they are included in the tumour tissue, a compromise needs to be achieved by taking into consideration the tolerance dose of the different OARs and simultaneously delivering sufficient dose to the target volume [33].

### Planning Techniques

Conventional planning is also known as “forward planning” and is considered a rather simplified form of IMRT, for which a trial-and-error method is applied in terms of beam angles, leaf positions and beam weight have to be defined and then the dose can be calculated. After evaluating the plan by visualisation of a three-dimensional dose distribution and a dose-volume histogram (DVH), the planner can inspect whether the plan is clinically acceptable or not and whether the goals are met or not. In case the plan does not meet the expectations, changes have to be performed as well as a dose calculation, until a satisfactory plan is found. An example of forward planning is 3D CRT, where the MLC leaves are used to fit the field with the shape of the PTV and homogeneous beam fluences are planned (in case no wedges are used). In this case the planner can adjust the relative weight of each beam.

With an increasing demand of a higher plan complexity and the need for more conformal dose distributions along with a better sparing of the surrounding tissues, inverse planning techniques, such as IMRT, have been introduced and nowadays are widely clinically used. In this technique, predefined treatment plan goals are used as an input for the treatment planning system (TPS), and known as “objectives and constraints”. This information is transformed and converted by computer algorithms into beam intensity maps, which a treatment machine is able to deliver [35]. The calculation of the linac parameters that enable the achievement of the criteria given as input, such as the beam weights, the number and shape of the MLC apertures, number of monitor units (MU), is performed, i.e. the planner does not have direct control over these parameters at any

point in the treatment planning process [36]. These dose distributions can be more complex than the ones achieved by conventional planning and include concave dose distributions or intentionally inhomogeneous dose distributions. Cost functions can be founded upon biological criteria or on dose-based criteria. Biological-based cost functions use a calculated radiobiological response, with calculations based on a certain model which builds the relation between radiation dose and volume of irradiated tissue to predicted biological response [36]. Although the use of biologically weighted objective functions might be more relevant since treatment outcome is determined by the biological response, most of the inverse planning algorithms still rely on dose-based cost functions [33, 36].

The evaluation of the quality of a treatment plans is verified by examining the 3D isodose distributions, the DVHs for targets and critical structures, as well patient-specific quality assurance (QA) data [37].

In IMRT, the division of each beam into several beam elements, the so-called bixels, creates intensity maps, where the intensity (fluence) for each of the bixels is optimised [33]. However, since it is not possible to deliver intensity-modulated photon beams directly, the intensity maps need to be transformed into several sequences of MLC shapes, called segments, via a process called leaf sequencing [33]. It is essential to know the mechanical limitations of the delivery system, such as the MLC leaf width, leaf-end leakage, leaf transmission and leaf travel, the speed of each leaf or the clinical dose rate by the leaf sequencing algorithms in order to link optimisation and leaf sequencing [33, 36, 37].

There are different techniques to implement IMRT delivery: a static technique and dynamic techniques. The static technique is the “step-and-shoot” technique, for which the beam is only turned on when the gantry is at specific angle positions and delivers several shaped field segments sequentially [37].

When IMRT is delivered dynamically, there is at least one element of the machine that is moving during the delivery of the treatment. “Sliding window” is a technique currently used where the MLC leaves move continuously while the beam is on [37]. Here, the fluence modulation is achieved by varying the trajectories of the leaves, taking into account their speed and a constant or variable dose rate of the linac. Tomotherapy and Volume-Modulated Arc Therapy (VMAT) are both techniques in which the gantry rotates while the beam is delivered. In Tomotherapy the dose is delivered by a fan beam, collimated by a binary MLC; whilst in VMAT, additionally to the continuous movement of the leaves (as in sliding window) and a gantry in continuous motion, the gantry is also rotating with a variable speed and variable dose rate [38]. The availability of all angles to deliver the therapy and the reduction of the treatment delivery time as well as the use of less MUs are other advantages brought by VMAT [39].

Multiple studies have been published to demonstrate the dosimetric advantages of IMRT over 3D CRT in terms of the conformity of the high dose region of the target, while avoiding the delivery of high doses to critical surrounding structures, allowing for dose escalation. The benefits of IMRT come at the cost of higher healthy tissue volumes receiving low doses of radiation, the so-called low dose bath, and a higher inhomogeneity within the targets [40]. Furthermore, IMRT plans are characterised by a higher complexity, take longer time to be delivered, prolonging the time that a patient spends on the treatment couch and decreasing patient throughput [39].



### Conventional and hypofractionated radiotherapy

The aim of radiotherapy is to deliver sufficient dose to the tumour in order to reach local control, however, without inducing severe complications in the surrounding normal tissue. Dose-response curves for the tumour control probability (TCP) and normal tissue complication probability (NTCP) can describe the conflicting goals (see Figure 2.1.12), where the TCP increases with increasing dose. Nevertheless, a dose escalation increases the NTCP, which is often the limiting factor in clinical situations. The area delimited by the TCP and the NTCP curves represent “the therapeutic window”, where the probability of tumour control without normal tissue complications reaches a maximum, at the optimum dose  $D_{opt}$  [33].

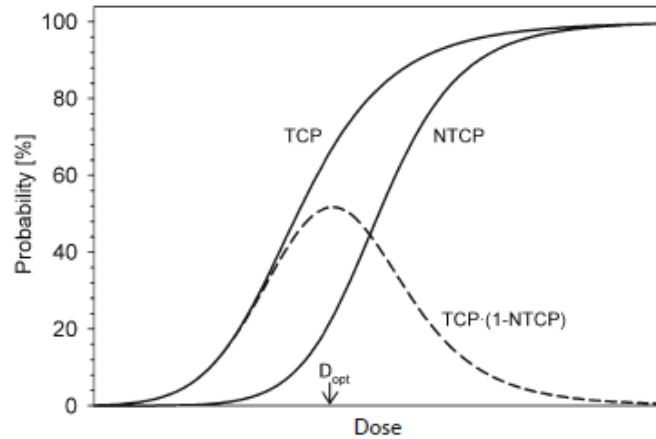


Figure 2.1.12: Dose-response curves for the tumour control probability (TCP) and normal tissue complication probability (NTCP) [33]. Figure reproduced with permission by Springer Nature.

The dose-response curves depend, however, on several biological and physical variables. The Linear Quadratic Model (LQM) is one of the most often used biological models, which aims to model and predict the fraction of cell killing for both tumour control and normal tissue complications when ionising radiation is delivered. The effect  $E$  (radiation cell kill) of a single radiation dose ( $d$ ) can be expressed by:

$$E = \alpha d + \beta d^2 \quad (18)$$

This linear-quadratic equation is considered to derive from a cell-surviving relationship of the form:

$$SF = e^{-\alpha d - \beta d^2} \quad (19)$$

$\alpha$  and  $\beta$  are parameters that estimate the amount of lethal and sub-lethal cell damage, respectively, whereas the  $\alpha/\beta$  ratio represents the dose at which both linear and quadratic components cause the same amount of cell killing. In a logarithmic plot, the higher the  $\alpha/\beta$  ratio is, the more linear the cell survival curve is; the lower the  $\alpha/\beta$  ratio is, the more curved the cell survival curve is [33, 41]. Due to the different radiosensitivity presented by different tissues (and their cells), each tissue is affected distinctly when receiving the same amount of radiation dose: tissues with a low  $\alpha/\beta$  ratio are relatively resistant to low doses in relation to tissues with high  $\alpha/\beta$  ratio. As a consequence, late responding tissues, or slowly proliferating tumours, have a low  $\alpha/\beta$  ratio, whilst early responding tissues, or rapidly proliferating tumours have a higher  $\alpha/\beta$ . This introduces the concept of “fractionation”, which refers to the total treatment dose being received in one single

session or over a period of several days or weeks. The choice of fractionation parameters is of great importance as the higher the dose per fraction is, the more damage it is going to induce (for a given total dose) and is often greater for short overall treatment times [19]. The biological effective dose (BED) is an inherent part of the LQM of radiation effect, and it would represent the physical dose, required to achieve a certain radiation cell kill, if the dose were to be delivered by infinitely small doses per fraction, or at an infinitely low dose-rate, in the case of continuous radiation rates [42, 43]. This concept has been suggested as a measure of effect  $E$ , in dose units, where  $d$  represents a single radiation dose,  $D$  the total dose delivered in  $n$  fractions ( $D = n \times d$ ), and for a given biological tissue (where  $\alpha$  and  $\beta$  are constant), indicating how much damage a particular fractionation regime will do [19]:

$$\text{BED} = D \times \left(1 + \frac{d}{\alpha/\beta}\right) = nd \times \left(1 + \frac{d}{\alpha/\beta}\right) \quad (20)$$

Different schemes of fractionation that have the same BED are called iso-effective. Consequently, one fractionation regime may be transformed into another iso-effective regime by using the following equation [33]:

$$n_2 d_2 = n_1 d_1 \times \left(\frac{\alpha/\beta + d_1}{\alpha/\beta + d_2}\right) \quad (21)$$

Typical  $\alpha/\beta$ -values are of the order of 3 Gy for late reactions and 10 Gy for early reactions. Most tumours have a high  $\alpha/\beta$  ratio, with  $\alpha/\beta$ -values of 10 Gy and can be fairly treated with normal fractionated radiotherapy (using single fraction doses of 1.8 – 2 Gy) while sparing late reacting tissues [33]. However, some tumours can have a very low  $\alpha/\beta$  ratio, smaller than for the surrounding normal tissue. In this case, aiming for better tumour control with approximately the same side effects, higher single doses applied in less fractions would be an advantage, leading to less repair in the tumour compared to normal tissue [19, 41]. This is called hypofractionation. Hypofractionated radiotherapy has seen an increasing interest due to the use of modern technologies, such as IMRT/VMAT and IGRT. While inverse planning, present in IMRT techniques, has made a better sparing of OARs and more sophisticated dose distribution possible, with the advances in IGRT the reduction of PTV margins was also achieved. All these reasons explain the further dose escalation and hypofractionated schemes [12, 33, 41, 44].

### 2.1.5 Photon Dose Calculation

#### Planning CT

CT provides 3-dimensional information of the patient with a number of axial images (slices), playing an essential role in radiation oncology. The images are not only used in cancer diagnosis but also for radiotherapy planning. They are created with a computer-based composition of X-ray images gathered from different angles while the patient is translated along the longitudinal axis, until the whole region of interest is covered. The CT scan is the mostly used imaging modality to perform the delineation of the target volumes and the OARs, even though other imaging modalities, like MRI or PET, may be also used in the treatment planning process. For an accurate dose



calculation an optimal image quality is essential as it influences the recognition and delineation of target volumes and OARs, and consequently a lower quality can induce improper delineation of structures. Moreover, its higher importance in radiotherapy is due to the fact that all dose calculations and plans are based on CT information: the accuracy of dose calculation is based on CT data and calibration of CT Hounsfield units (HU) to relative electron density [45].

The grayscale values of the planning CT correspond to the local attenuation of X-ray radiation, depending on the atomic number and electron density and being an indirect representation of the various tissue-electron densities within the images. MV radiation interacts with tissue mainly via Compton scattering (thus according to electron density) and therefore the CT data can be used directly (after conversion to electron density) for radiation-absorbed dose calculations [19].

The planning CT is discretised and composed of a matrix of voxels and the voxel tissue information at location of a CT scan is expressed in Hounsfield Units (HU). The Hounsfield scale, by definition, assigns the value zero for a medium with the same attenuation as water [19]. The HU is defined as:

$$HU(x, y, z) = 1000 \times \frac{\mu(x, y, z) - \mu_w}{\mu_w} \quad (22)$$

where  $\mu(x, y, z)$  is the average linear attenuation coefficient of the tissue for a voxel of tissue in the patient at location  $(x, y, z)$  and  $\mu_w$  is the linear attenuation coefficient in water. The  $HU(x, y, z)$  represents the gray scale CT images in the same  $(x, y, z)$  spatial coordinates. The CT scanner must be calibrated to measure the relationship between tissue density (or electron density) and HU, resulting in a CT-to-density-table, also known as an HU-to-density-table, which is dependent on the individual CT scanner. The CT-to-density-table should represent density behaviour over the full range from air, over lung and soft tissue to low and high density bone and metal inserts. In case the CT images have voxels with higher HU than contained in the table, the density cannot be determined but it is assumed to be identical to the density for the highest density HU in the table. Similar behaviour occurs with voxels with lower HU than the lowest HU entry, i.e. it is assumed they have an identical density as the lowest density in the table [19].

For the calculation of the treatment dose to be identical, or as close as possible, to the dose to be delivered during the treatment sessions, the patient needs to be in the treatment position, with all the immobilisation devices planned to be used during treatment.

### Dose Calculation Algorithms

When using ionising radiation, to calculate the corresponding dose deposited in human tissue, it is necessary to solve a complex equation – the transport equation. This equation has many variables, depending on the patient's anatomy but also on the field size, field shape, energy of the radiation, beam direction, among other [33]. Furthermore, an accurate calculation of a 3D dose distribution within the patient is one of the most important proceedings and a necessity for the evaluation of a treatment plan. It is what connects the elected treatment plan parameters and the observed clinical result in terms of absorbed dose distributions [33].

When the dose algorithms for high-energy photon beams started being developed, they were created for a phantom made of an homogenous material, such as a water phantom [46]. Some measurements such as tissue air ratios, tissue phantom ratios, output factors and off-axis ratios

were performed for some common treatment fields and under reference conditions, using a water phantom [33]. Since not all possible combinations of treatment fields were measured, some measurements were extrapolated to other specific fields. Moreover, as a water phantom is not entirely representing a patient, some correction algorithms were also applied, for example for the approximate consideration of tissue heterogeneities, to enable a more accurate dose calculation within the patient [33]. These methods, so called “correction-based methods”, although very fast, were relying almost entirely on a set of measurements and not taking into consideration the energy transport by electrons and photons inside the patient [33].

The processes regarding energy transport and deposition within the patient could only be taken into consideration once “dose kernels” were introduced. Dose kernels describe the energy transport and deposition in water, caused by primary photon tissue interactions. Tissue inhomogeneities in patient geometries have an impact on the dose calculation and could be accounted for, by using electron densities derived from the planning CT scan. These dose algorithms are based on analytical solutions of the transport equation and known as “model-based algorithms”, which include the Superposition and Convolution methods. The main principle is that the kernels are first pre-calculated with Monte Carlo (MC) simulations in water and then scaled to account for heterogeneities. The accumulation of dose for Superposition and Convolution methods is divided into several steps [47]:

- A model for the radiation field coming out of the radiation source, representing the “primary energy fluence”. This step requires modelling the beam properties and energy spectrum based on machine characteristics;
- The calculation of the energy absorption and transport within the patient, considering the absorption of the primary photons (“total energy release per unit mass” – TERMA) and the transport of the energy by the secondary electrons and photons, by introducing specific “dose kernels”).

However, some approximations must be applied in order for these algorithms to be acceptable when used for clinical purposes [47]:

- Neglect or estimation of kernel tilting;
- Neglect or estimation of density scaling;
- Estimation of depth spectral hardening and off-axis spectral softening;
- Various approximations to take scattered photons into consideration.

Specific dose kernels commonly available in commercial TPSs are:

- Pencil beam (PB);
- Collapsed Cone (CC).

**Pencil Beam:** it is a dose kernel representing the 3D dose distribution of many infinitely narrow pencil shaped beams along the primary beam direction. The dose is calculated as a linear superposition of the corresponding dose deposition kernels and TERMA. The equivalent path length, calculated from the total electron density between the point where the PB enters the phantom/body and the voxel where the dose is deposited, is used as a basis to scale the PB kernel. Tissue inhomogeneities are thus accounted for along the direction of the central beam axis and the PB kernels are shorter for high electron densities, whereas for low electron densities they are

elongated. Electron variations in the perpendicular direction to the PB axis are, however, not considered, i.e. in the lateral direction the medium is presumed to be water, resulting in a lack of accuracy in non-homogeneous tissues [33].

**Collapsed Cone:** a technique that describes a specific internal sampling of the dose kernels, an angular discretisation of the kernel into cones, for which the calculation of energy transport and deposition is more efficient [48]. Similar to the PB method, the CC method uses a convolution between TERMA and the dose deposition kernel, leading to a dose deposition in the voxels along the central axis of the cone. However, by comparison with the PB, CC method models partly lateral scattering and backscattering, yielding more accurate dose calculations, in particular in inhomogeneous tissues [33, 48].

Radiotherapy in body regions, where there are interfaces between very different materials with considerable density differences (e.g. lung/tissue or air-filled cavities within the facial bones), and when small fields in stereotactic techniques are used, can cause problems for analytical photon-beam algorithms. This results from the lack of charged-particle equilibrium on the central axis of these small fields and therefore not reliably accounting for secondary electron transport [19]. The MC technique, a stochastic method that models particle transport, can, however, minimise dose inaccuracies in treatment planning, and has been shown to calculate accurate dose distributions if radiation sources and patients are completely modelled and a sufficiently large number of simulations are performed [19, 47, 49].

For radiation transport problems, this approach simulates the tracks of individual particles [50, 51].

For MC treatment planning applications the linac head can be separated into an “upper” part and a “lower” part. The “upper” part consists of all components that are fixed for all possible beam settings, representing the patient independent part, whereas the “lower” part consists of the patient dependent part, starting from the patient specific collimating devices [52]. The “upper” part is modelled once, an operation named “beam modelling”, whose purpose is to perform an adequate characterisation of the primary beam, before entering the patient dependent part. During beam modelling a file, known as “phase-space”, is created at the entrance of the “lower” part, containing all necessary transport parameters of a large number of particles entering the lower part of the linac, such as particle type, coordinates, energy, particle weight [19, 52].

There are different approaches to perform a detailed beam model:

- Full head simulations, for which the entire path through the treatment head is simulated by a MC algorithm. The phase space files can then be stored and are accessed during a patient dose calculation. However, comprehensive modelling is only possible if full information on the key components in the treatment head (their geometry and composition) is given by the accelerator manufacturers [19];
- Source model approach, which utilises multiple virtual sources (e.g. the target, the primary collimator and the flattening filter) to represent a beam for a certain treatment head design. These virtual sources, that characterise the beam, are then used separately to build the phase-space. Each particle is then introduced individually to the dose calculation code, which avoids the necessity to accumulate a large phase-space file [19].

At the plane of the phase-space file is where the radiation transport in the patient starts, and it goes until the dose is deposited in the patient geometry.

The simulations start at the position where the electron beam leaves the vacuum window of the linear accelerator and entering the linac head, where it collides with an X-ray target placed in the beamline, and gives rise to bremsstrahlung photons. The photons pass through the treatment head (primary collimator, flattening filter, monitor chamber, collimating jaws, multileaf collimators) of modern clinical linacs and photon source parameters, such as energy, position and direction are sampled and the radiation transport in the patient is simulated as well (see Figure 2.1.13) [19]. The patient geometry is described by a 3D cartesian array of voxels, with cubic voxel sizes up to 5 mm for the body and up to 3 mm for the head [19]. Some parameters are required as input for dose calculations with MC, such as density and material type of the different tissues, derived from the CT numbers [53].

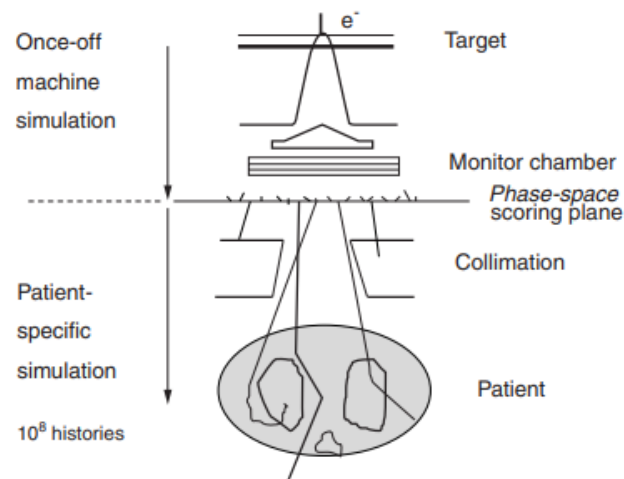


Figure 2.1.13: Schematic drawing illustrating the MC simulation in radiotherapy treatment planning, showing both phases: the machine simulation and the patient-specific simulation [54]. Figure reproduced with permission by Springer Nature.

The photon may experience various interactions (Rayleigh scattering, Compton scattering, photoelectric effect, pair/triplet production), with the probability for interactions directly dependent on the cross-section of the medium: the larger the cross-section at the interaction site, the higher the probability of interaction is going to be. The interaction is then simulated, the energy and direction of the scattered photon are calculated, as well as of the electron participating in the interaction [52]. Here, well-known theories describing the kinematics of the various types of photon interaction are applied [52]. After the first interaction site, the photon is then transported to the next interaction site and is forced to interact with the medium [50, 51].

Regarding electron transport, electrons and photons behave differently, i.e., while photons go through a relatively small number of interactions per particle track, electrons, on the other hand, experience a very large number of Coulomb interactions with the electrons and atomic nuclei while traversing the material [52]. This represents a very intensive operation when simulating each of the individual Coulomb interactions [52]. Due to the computational high costs, this operation is not simulated but another approach is usually applied, a so-called condensed-history model. Here, each electron track is divided into a series of short track segments, also known as

“steps” and the resulting (cumulative) energy loss and angular deflection are calculated, once per step.

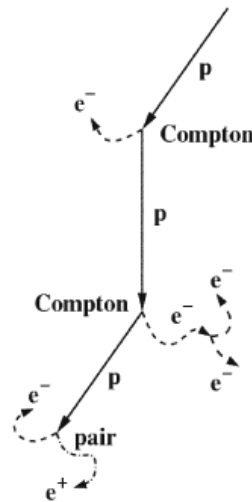


Fig. 2.1.14: Schematic drawing of a photon history in the MC simulation of radiation transport [33]. Figure reproduced with permission by Springer Nature.

The particles (primary and secondary photons, contamination electrons and secondary electrons) in the MC calculations are transported until they reach a defined energy cut-off [51]. The trajectories and interactions of each particle of the irradiation beam are simulated and followed, until they are either absorbed or abandon the area of interest (see Figure 2.1.14) [33].

The transport of a primary particle is called “history”. One single particle does not provide useful information about the dose distribution. However, the larger the number of particle histories is, the higher the accuracy of the calculated dose distribution will be. To achieve statistically representative results and an adequate accuracy of the MC simulation (1 - 2% uncertainty at 1 mm to 2 mm voxel size) these processes are repeated for a considerable large number of particles, and for clinical purposes in medical radiation physics treatment planning requires approximately  $10^8$  to  $10^9$  photon histories [19]. However, a large number of particles (or simulations) makes the MC method a slow technique [19, 51]. In order for MC algorithms to be clinically acceptable in terms of efficiency and calculation time, some measures had to be taken, such as using faster computers, moreover approximations and simplifications were made, and several MC codes have been introduced: Macro Monte Carlo, Superposition Monte Carlo, Voxel-based Monte Carlo (VMC, VMC++), among others [47, 51, 52].

In fast MC simulations, a pre-defined phase space or virtual source models replace the simulation of the primary histories and the particle interactions in the linac head. Examples of these fast MC dose calculation engines, commercially available are Monaco TPS (Elekta AB, Stockholm, Sweden), Eclipse TPS (Varian Medical Systems, Palo Alto, CA) or ViewRay MRIdian TPS (ViewRay Inc., Oakwood Village, OH, USA).

The two TPSs relevant for this research project were Monaco and Viewray MRIdian TPS.

The MC algorithm used in the Monaco TPS is called X-ray Voxel Monte Carlo (XVMC), originated from the VMC code, which was developed by Iwan Kawrakow and Matthias Fippel as a fast calculation engine for electron beams [55]. XVMC is a fast MC code, where both photon and electron transport are modelled, as the dose distribution of therapeutic photon beams is originated mainly from secondary charged particles.

This TPS uses three-beam model components: a virtual source model, transmission probability filters and an X-ray VMC engine [56].

Regarding the first component, the virtual source model, its intention is to model the linac photon beam, consisting of a primary photon source, a scatter photon source, and an electron contamination source. A virtual source model replaces the use of MC algorithms to simulate transport through the components of the linac, to accelerate the calculation [56].

Transmission probability filters are used to model the primary collimator, jaws and the MLC. Similarly to the virtual source model's purpose, the transmission probability filters are used instead of direct MC simulations, to lower calculation times [56].

Finally, the dose in the patient model, defined by the patient CT scan, is modelled by an X-ray VMC engine.

The MC algorithm in the Viewray planning system is the Kawrakow MC (KMC), also based on the X-ray VMC algorithm [30].

This model consists of two components: the source model and the patient model. The source model executes the particle transport from the phase space, in the bremsstrahlung target, until the gradient coils of the MR-linac system. As for the patient model, it performs the particle transport in the patient geometry, defined by the patient CT scan, and dose calculations are performed by the KMC engine. In this TPS all device components in the path of the radiation beam are modelled for their attenuation of the fluence of the treatment beams, including the MRI gradient coils, the MRI RF shield and the patient couch [30].

## 2.2 Workflow in External Beam Radiotherapy

The workflow in radiotherapy is often compared to a chain, consisting of different links (see Figure 2.2.1):

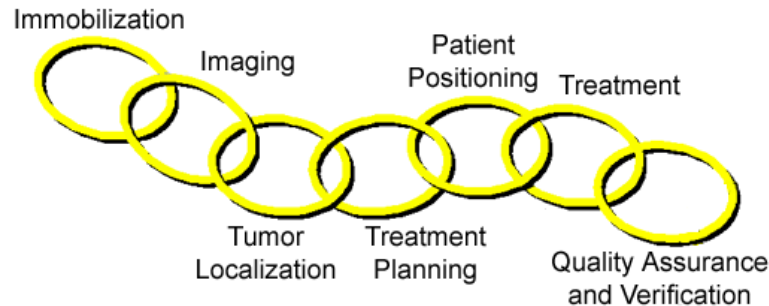


Figure 2.2.1: Workflow in radiotherapy [57]. Figure reproduced with permission by Springer Nature.

The first link refers to “patient immobilisation”, which is a crucial step especially when the delivery techniques are becoming more and more sophisticated. Immobilisation techniques and the consequently reduction of the uncertainties, arising from movements of the patient and motion of the nearby organs, are used not only to ensure that the CTV is located within the PTV during the treatment, but also to enable the diminishment of the CTV to PTV margins [57].

A small setup error or modifications of the position of the patient in relation to the planned position can induce serious underdosage in the target and/or overdosage in the healthy tissue. Therefore, a reliable and accurate fixation of the body area or organ that is going to receive treatment is a very important requirement for radiotherapy [33, 57]. The immobilisation accuracy must be the highest for stereotactic treatments, when the patient is planned to be treated in a single session or in a reduced number of fractions [33].

Once the patient is sufficiently immobilised, images of the patient are acquired, as an accurate model of the anatomy is a crucial prerequisite for treatment planning. This is referred by the second and third links: “Imaging” and “Tumour Localisation”, whose aim is to localise the tumour and the OARs. A higher precision in tumour localisation and volume definition has been seen over time due to advances in the medical imaging field. CT images are the basis for dose calculation, as with this modality it is possible to quantitatively characterise the physical properties of heterogeneous tissues regarding electron densities. However, MRI, which is known by its high soft tissue contrast, is very important for an accurate delineation of the target volume and surrounding organs. In reality, MRI is often considered superior to CT and can help delineate different structures. Furthermore other imaging modalities, such as PET imaging, are capable of detecting complementary metabolic information. When combined, all the different imaging modalities can add extra information and therefore play an important role in imaging for radiotherapy. This complementary information can be offered by the registration of various images. The aim of image registration is to align the input image to a reference image, in order to maximise the similarity between both images [58]. A variety of algorithms can be used, depending on the method and type of transformation the input image will undergo when the registration process occurs [58, 59].

The fourth link in the chain of radiotherapy is “Treatment Planning”, whose purpose is the optimisation and evaluation of alternative irradiation treatment strategies that lead to the best coverage possible of the target volume while sparing enough the surrounding healthy tissue. The planning process is constituted by several parts: segmentation of the target volumes and OARs, determination of the treatment technique, dose calculation and evaluation of the 3D dose distribution [33].

The following link refers to “Patient Positioning” for treatment delivery. The goal is to place the patient on the treatment couch in the exact same position as during patient imaging, by utilising the same immobilisation devices used before. Moreover, several IGRT strategies are currently available at linacs to make sure of the correct position of the PTV, by acquiring data shortly before or even during treatment. The simplest process of patient surveillance can be performed by using an electronic portal imaging device (EPID). The patient position is verified by a linac beam, which after traversing the patient body, is then recorded using digital imaging devices, such as amorphous silicon flat panel detectors. The acquisition of the outgoing beam yields a 2D portal image. The resulting image and a digitally reconstructed radiograph (DRR), which is a simulation of radiographic images produced through a perspective projection of the 3D image (volume) onto a 2D image plane, are registered and compared. Another well-known strategy is the usage of CBCT, with an in-room independent kilovolt (kV) source and a 2D digital detector panel on the opposite side, both mounted to the linac. The patient is imaged from multiple 2D projection angles, through rotation of both source and detector around the patient. The projected images are used to reconstruct a 3D image, with an enhanced visualisation of soft tissue, as opposed to the traditional 2D portal imaging. However, the HU values are less reliable than the planning CT, due to scatter detection and other limitations.

Another IGRT strategy in current use is MR imaging, known as MRgRT. There are currently two MR-linac systems commercially available, which consist of a conventional linac combined with an MR-scanner, as presented earlier, with the potential to perform online adaptive MRgRT. Stereoscopic X-ray imaging as well as optical surface imaging (SGRT) are also strategies that are currently being used, and similarly to MRgRT, are technologies of interest in this work. Therefore, a more detailed description of these strategies will follow in section 2.4.

The next link of the chain represents the most important one in radiotherapy, characterised by the radiation delivery. Most radiotherapy treatments are performed by EBRT with photons. Nevertheless, radiotherapy with internal sources has also been established and proven to be efficient for special indications. Charged particle therapy with proton or carbon beams are gaining more importance worldwide. However, their use is still limited to a rather small number of centres, due to high costs [33].

In radiotherapy, the “Quality Assurance and Verification” is a very important step in preventing errors and inaccuracies that may induce radiation treatment accidents and injury of the patient. Moreover, it helps improving qualitatively the treatment. Therefore, a careful network of quality assurance and verification needs to be adopted, in order to cover all aspects of the chain and all components involved.



## 2.3 Basics in Medical Imaging

In medical imaging, energy penetrates the human body and interacts with the tissues, providing information about the internal anatomy. A good quality of the images is important, which always involves a compromise: X-ray images with higher quality are obtained with higher radiation dose to the patient; the longer the image acquisition time, the higher the MR image quality; and better US images are acquired when the ultrasound power levels are large. Nevertheless, a balance between the pursuit of the perfect image quality and patient safety and comfort is crucial [60].

### 2.3.1 Kilovoltage X-rays

Kilovoltage X-rays for imaging are generated in an X-ray tube, composed by a vacuum tube with a cathode, emitting the electrons, an anode, collecting the accelerated electrons and a high voltage power source to accelerate the electrons. A large electric potential difference is applied between both in order to accelerate the electrons that travel from the cathode towards the anode. The kinetic energy of the accelerated electrons on the impact with the target is then converted to other forms of energy, such as heat release or emission of radiation in the form of X-ray photons with a range of energies (X-ray spectrum). The X-rays can be released in the form of bremsstrahlung (yielding a continuous X-ray spectrum) and characteristic radiation (yielding characteristic peaks, with discrete energies that are characteristic of the particular target atom where the transitions occurred; and these peaks are superimposed onto the continuous spectrum), as the electrons are decelerated and change their direction [60, 61].

The bremsstrahlung spectrum is a continuous spectrum, composed of X-ray photons with energies between zero and a maximal energy, the kinetic energy of the electron that hits the target. The bremsstrahlung spectrum depends on the kinetic energy of the incident electron and also on the thickness and atomic number of the target [18].

Targets are divided into two categories: they can be thin or thick, depending on the range of electrons  $R$  of a given kinetic energy  $E_K$  in the target material. A thin target has a thickness much smaller than  $R$  and for a thin target radiation, the energy irradiated is proportional to the product  $E_K Z$ , where  $Z$  is the atomic number of the target. The intensity of the X-ray photons is constant between zero and the kinetic energy  $E_K$  of the incident electron, and zero for all energies above  $E_K$  (see Figure 2.3.2, curve 1) [18].

A thick target may be considered as consisting of many superimposed thin targets, with total thickness in the order of  $R$  [18]. The intensity of a thick target spectrum can be calculated by the following expression:

$$I(h\nu) = CZ(E_K - h\nu) \quad (23)$$

Where  $C$  is a proportionality constant and  $h\nu$  is the photon energy.

Typical thin and thick target bremsstrahlung spectra for imaging, originating from 100 keV electrons accelerated towards a thin and a thick target are shown in Figure 2.3.2, curves 1 – 4 [18].

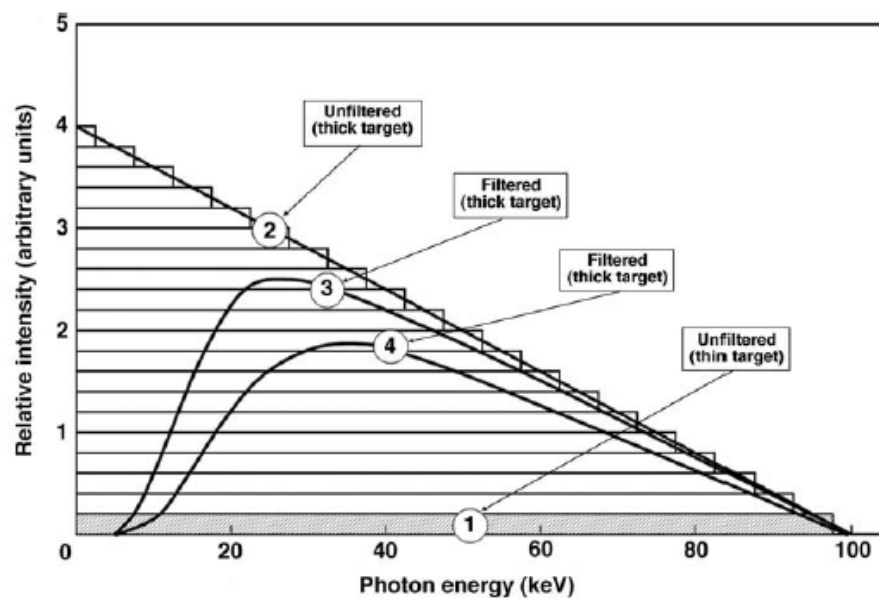


Figure 2.3.1: Diagram illustrating a typical thin target spectrum (curve 1) and thick target spectra (curves 2, 3 and 4) for an X-ray tube, when electrons are striking a target with an energy of 100 keV [18]. Curve 1 represents a thin target spectrum, with electrons striking the target and producing a constant intensity of photons with energies from zero to the kinetic energy  $E_K$ . Curve 2 represents a thick target, producing an unfiltered spectrum (ignoring filtering within the target itself and X-ray tube components). Curve 3 is showing the spectrum also for a thick target, for which the photon beam is filtered by an X-ray tube window (low energies are filtered out). Curve 4 represents the spectrum for a beam filtered, not only by the X-ray tube window but has also an additional filtration. Figure reproduced with permission by I.A.E.A.

A filtered bremsstrahlung spectrum is achieved by the removal of X-rays with lower energy (around 10 keV). The intensity of photons increases to a maximum (between one third and one half of the maximal X-ray photon energy), which then decreases to zero as the X-ray energy increases to its maximum [60]. The spectrum is filtered by attenuation in different materials: not only the materials that are intrinsic to the X-ray tube, such as the glass window of the tube insert; but also materials that are located within the beam path (e.g. thin aluminium and copper sheets), for optimal low-dose imaging purposes [60].

The amount of emitted photons or their energy are dependent on some parameters of the X-ray source, in the following way:

- The amount of electrons, and consequently the intensity of emitted photons is directly related to the cathode current multiplied by the time the current is on (in mAs) [61];
- The energy carried by the electrons hitting the target, and therefore the energy of the emitted photons depend on the voltage between cathode and anode (in kV) [61];
- The total incident energy (in joule) is the product of the voltage, the cathode current and the time the current is on [61].

Ionising photons can interact with matter in different ways, depending on their energy, as explained in Section 2.1.1. An X-ray beam, with an energy that typically vary from 25 to 125 kV, is attenuated by the different types of tissues in the body. The individual interactions are of statistical nature, but the macroscopic intensity of the beam follows a deterministic exponential law, as shown in section 2.1.1:

$$N(x) = N_0 \times e^{-\mu x} \quad (24)$$

and can also be written as follows:

$$I_{\text{out}} = I_{\text{in}} \times e^{-\mu d} \quad (25)$$

where  $I_{\text{out}}$  refers to the intensity of the beam after passing through a certain material and leaving it, which is related to the intensity of the incoming beam  $I_{\text{in}}$ , and  $\mu$  is the linear attenuation coefficient. This can only be true if the material is homogeneous and the beam consists of mono-energetic photons. A real X-ray beam contains a whole spectrum of energies and when traversing the human body, the photons travel through a nonhomogeneous medium. In this case the intensity of the outgoing beam can be expressed by:

$$I_{\text{out}} = \int_0^\infty \sigma(E) e^{-\int_{x_{\text{in}}}^{x_{\text{out}}} \mu(E,x) dx} dE \quad (26)$$

where the intensity distribution of the incoming beam is a function of the energy [61].

Radiography refers to an imaging technique that uses X-rays passing through a three-dimensional object. The result of the attenuation of the X-ray beam passing through the object is a two-dimensional image reflecting the internal shape of the object. Incident X-ray beams are heterogeneously attenuated as they traverse the anatomical structures in the patient and are projected onto a detector. This procedure is known as “projection radiography”.

The X-rays are produced in the focal spot, which is considered small, and diverge as they flee from this spot. Consequently, the beam becomes larger in area and less intense, and the object being radiographed is magnified in the X-ray radiography, according to the following mathematical expression:

$$M = \frac{L_{\text{image}}}{L_{\text{object}}} = \frac{a+b}{a} \quad (27)$$

where  $L_{\text{image}}$  refers to the length of the object as seen on the image,  $L_{\text{object}}$  is the length of the actual object,  $a$  refers to the object distance and  $b$  to the object to detector distance, as shown in Figure 2.3.2 [60].

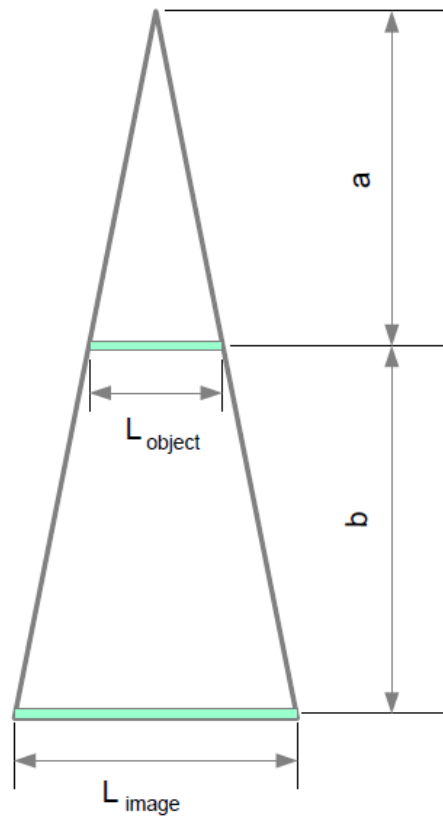


Figure 2.3.2: A schematic drawing representing the geometry of the beam divergence:  $a$  refers to the distance between the X-ray source and the object being radiographed;  $a + b$  represents the distance between the X-ray source and the detector. Figure adapted from [60].

The magnification is always greater than unity. However,  $M$  is closer to 1 when the distance between the object being radiographed and the detector is close to 0,  $b \approx 0$ , which happens when the object is positioned on the detector. Furthermore, for each plane perpendicular to the X-ray beam axis, with a certain distance from the X-ray source and from the detector, the object magnification is slightly different, which explains the different magnification of different anatomical structures [60].

### 2.3.2 Clinical Computed Tomography

CT is an essential part of radiotherapy as the patient model must be accurate and representative of the patient in the course of treatment. Moreover, it also plays an indispensable role in tumour identification, localisation and delineation, as well as in dose calculation.

Clinical CT scanners have an X-ray source, which rotates continually around the patient, as represented in Figure 2.3.3.

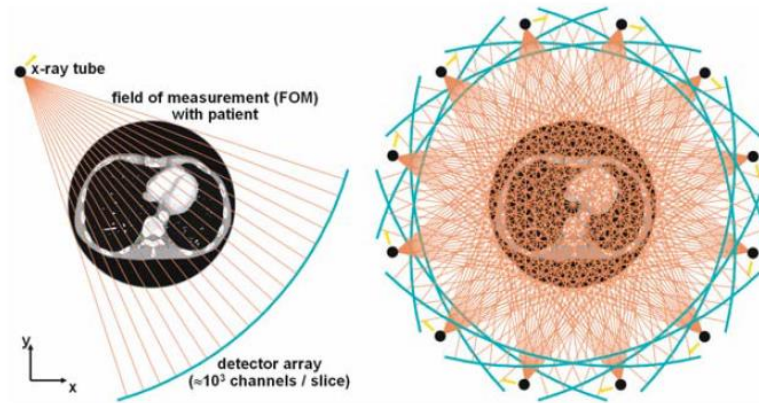


Figure 2.3.3: Clinical CT represents the measurement of an object's X-ray absorption along straight lines, for which the in-plane scan geometry represents a fan beam geometry [33]. Fan beam projection represents a fan of data that converges on a vertex, and each individual ray corresponds to a detector measurement of X-ray photon attenuation. Figure reproduced with permission by Springer Nature.

A cylindrical detector with many elements is mounted opposite to the source to measure the X-ray attenuation characteristics of tissue. The in-plane scan geometry is the fan-beam geometry, where each single ray corresponds to a line integral, extending from the X-ray source traversing the body of the patient and finally hitting the X-ray detector (see Figure 2.3.4). The couch is constantly translated through the CT gantry and the measurement of all straight lines result in the generation of several axial slices, with 3D information of the patient's anatomy [33, 60]. The table movement is characterised by the pitch – the ratio between the axial distance over which the table moves during a complete tube rotation (called table feed) and the slice thickness.

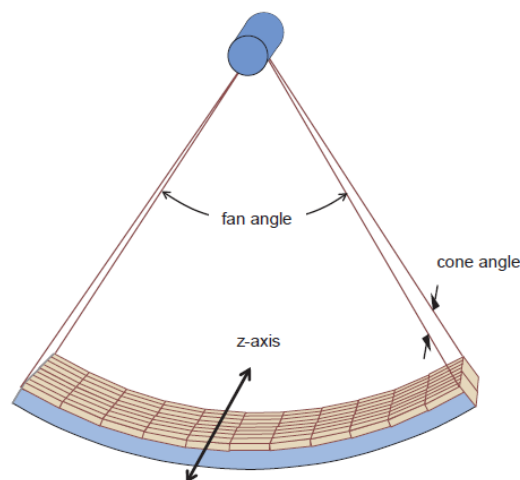


Figure 2.3.4: The illustration of a narrow cone beam geometry and the detector array, composed by several detector modules mounted along the z-axis [60]. Figure reproduced with permission by Wolters Kluwer Health/Lippincott Williams & Wilkins.

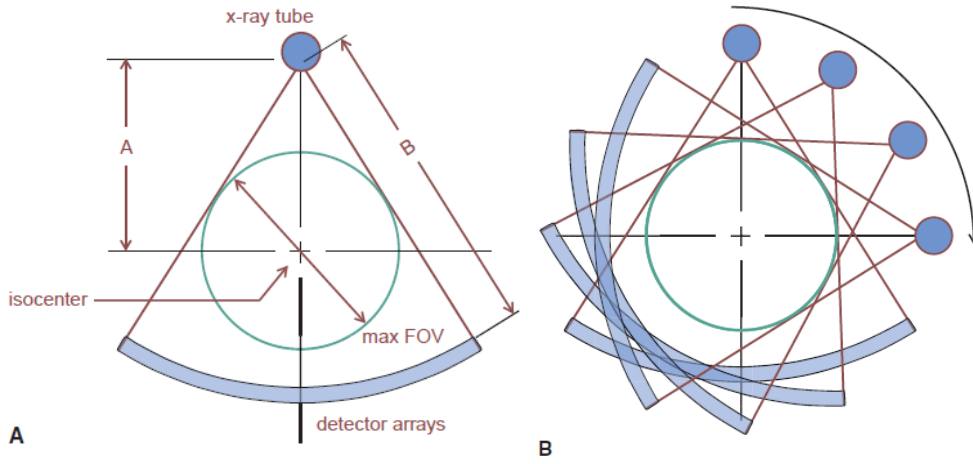


Figure 2.3.5: A) The geometry of a CT scanner, where the X-ray tube, the isocentre, the detector array, as well as the source-to-isocentre distance  $A$  and the source-to-detector distance  $B$  are depicted [60]. B) The X-ray tube and detector arrays are mounted onto the same rotating platform. Multiple line integrals are measured as the CT gantry rotates, to acquire sufficient information for 3D image reconstruction [60]. Figure reproduced with permission by Wolters Kluwer Health/Lippincott Williams & Wilkins.

In Figure 2.3.5, some basic geometry regarding CT scanners is shown. The isocentre represents the point around which the CT gantry rotates and it can also be the centre of the reconstructed CT image. The source-to-isocentre distance as well as the source-to-detector distance are represented by  $A$  and  $B$ , and according to equation  $M = \frac{L_{\text{image}}}{L_{\text{object}}} = \frac{a+b}{a}$ , in section 2.3.1, the magnification factor from the isocentre to the detectors is given here by  $M = \frac{B}{A}$ .

Modern CT scanners use indirect scintillating solid-state detectors. The detector's scintillator elements are used to detect X-ray photons, converting the X-rays into visible light. Light photons are then converted by photodiodes, to an electrical current. The data acquisition system connects to the photodiode, integrating the photocurrent from the diode and converts the electric charge signal to voltage, using a transimpedance amplifier. The analog to digital conversion is then performed, also by the data acquisition system [33, 61].

In clinical CT scanners the absorption of an object's X-ray attenuation is measured along straight lines, through the detection of the intensity of the beam reaching the detector. The following expression referring to the projection of the function  $\mu(x, y, z)$ :

$$p(L) = -\ln \frac{I_{\text{out}}(L)}{I_{\text{in}}} = \int_L \mu(x, y, z) dL \quad (28)$$

It shows that the line integral along the line  $L$  of an object's linear attenuation coefficient distribution  $\mu(x, y, z)$  is expressed by the negative logarithm of the intensity measurement relative to the corresponding X-ray attenuation along a straight line. After performing multiple measurements of the object, covering the entire field-of-view (FOV), enough information is gathered and the projection values  $p(L)$  can be used for image reconstruction, i.e. the attenuation value at each point of the scanned slice can be reconstructed [33, 61]. The CT reconstruction process, called back-projection, converts the raw data that was acquired to a series of CT images, usually reconstructed as a series of adjacent axial images [60].

In order to solve the reconstruction problem several methods were developed: filtered backprojection, iterative reconstruction or algebraic solutions, with backprojection the most established technique [61].

The reconstructed image is expressed in CT values, as already explained in section 2.1.5.

### 2.3.3 Magnetic Resonance Imaging

MRI is a non-invasive imaging technique, which works on the principle of nuclear magnetic resonance (NMR), discovered in the early 1940s. NMR studies the behaviour of atomic nuclei with spin angular momentum and associated magnetic moment, in an external field. Unlike CT, MRI does not hold any information about the electron densities, essential for radiotherapy treatment planning. MRI measures a magnetic property of tissue, describing the behaviour and ability of protons, particles with angular momentum and magnetic moment, to absorb and re-emit electromagnetic radiation at a specific resonance frequency (the Larmor Frequency), in an external magnetic field [61]. In clinical routine, NMR and MRI can be distinguished by the fact that in NMR only the hydrogen nuclei is exploited, whereas in MRI all nuclei with a non-zero spin can be used [62].

MR images are distinguished by their high soft tissue contrast and multiplanar tomographic format. They are therefore considered a good choice for the display of patient's anatomy and pathology in radiotherapy.

Atomic nuclei consist of protons and neutrons, with a net positive charge. Certain atomic nuclei, such as hydrogen nuclei, are characterised by a quantum-mechanical property, so-called "spin angular momentum". Hydrogen, also referred to as protons (nucleus of  $H_1^1$ ), with spin  $1/2$ , is also one of the most abundant elements in the human body, which makes this element suitable as an MRI source. Only nuclei with non-zero spins are able to absorb and emit electromagnetic radiation and undergo "resonance" when placed in a magnetic field [61].

For the nucleus of  $H_1^1$  there are two possible spin states, commonly denoted as  $+1/2$  and  $-1/2$ , referred as "spin-up" or "parallel" and "spin-down" or "anti-parallel", respectively. These two separate states are observable in the presence of an external magnetic field,  $B_0$ , reflecting an energy difference  $\Delta E$  between the two states. This phenomenon of quantised energy states is known as the "Zeeman effect" and the energy gap is given by the Zeeman equation [61]:

$$\Delta E = h\gamma B_0 \quad (29)$$

where  $h$  is Planck's constant and  $\gamma$  refers to the gyromagnetic ratio, a constant specific to a particular nucleus. For the  $H_1^1$  nucleus, the value is 42.58 MHz/Tesla [61].

Not only spin angular momentum but also the transfer of energy may assume only discrete units, and a proton in the lower energy state can change to the higher energy state by absorbing a photon of frequency  $\omega_0$  with energy equal to [61, 63]:

$$\Delta E = h\omega_0 \quad (30)$$

The Zeeman equation and the Planck relation can be combined, resulting in the Larmor equation, showing that NMR resonance frequency  $\omega_0$  equals to the gyromagnetic ratio  $\gamma$  multiplied by the magnetic field strength  $B_0$  and is given by the following expression [61]:

$$\omega_0 = \gamma B_0 \quad (31)$$

In imaging, each voxel contains a considerable quantity of protons, each proton with its own spin and associated magnetic moment. Under a dynamic equilibrium, since more spins occupy the lower energy level, the net magnetization vector,  $\vec{M}_0$ , which represents the sum of all individual magnetic moments, yields a net polarisation in the direction of the external magnetic field  $\vec{B}_0$ . The direction of the  $\vec{B}_0$  field is commonly designated as the z-axis, and using this coordinate system,  $\vec{M}_0$  has only a component in the longitudinal z-axis  $\vec{M}_z$ . The stronger the external magnetic field is, the larger the net magnetization vector will be, and consequently the signal. The amplitude of the magnetization,  $M_0$ , is also proportional to the number of spins inside each voxel [61].

A direct measurement of the net magnetization is not possible. However, this can be quantified by disturbing the equilibrium via the transmission of photons with the appropriate energy and therefore frequency, the Larmor frequency. With the transmission of an electromagnetic wave, also known as a RF wave, with an orientation perpendicular to the  $\vec{B}_0$  field, photons are absorbed by the tissue, i.e. by protons, creating a transverse magnetization  $\vec{M}_{xy}$ . This process is called excitation [61, 63]. The RF pulse disturbs the equilibrium conditions and induces a rotation in phase by the protons while it is being applied [63].

When the RF pulse is turned off, the relaxation process begins by releasing the absorbed energy and the system returns to its dynamic equilibrium: the magnetization transverse component  $\vec{M}_{xy}$  returns to zero, while the longitudinal component  $\vec{M}_z$  reaches its maximum  $\vec{M}_0$ . The relaxation process can be divided into two independent parts, which happen simultaneously:  $T_1$ - and  $T_2$ -relaxation [61, 63].

$T_1$ -relaxation, also known as “spin-lattice” relaxation, characterises the exponential increase until total restoration of the longitudinal component of the net magnetization vector  $\vec{M}_z$  is achieved, after the RF pulse is switched off. The reason for this relaxation is spin-lattice interaction, which refers to the process in which the spins release the energy acquired by the RF pulse, back to the surrounding medium (the “lattice”), restoring their equilibrium state [61, 63].

$T_2$ -relaxation, or “spin-spin” relaxation, describes the event that causes the disappearance of the transverse component of the net magnetization vector  $\vec{M}_{xy}$ , immediately after an RF pulse is switched off, caused by a loss of phase coherence between the different spins. Every spin is exposed to a fluctuating field, influencing the z-component of the magnetic field, and therefore the phase and precession frequency [61, 63].

The rate of dephasing is different for each tissue: in fat tissue the protons dephasing process is faster, while for water the same process takes longer time. Also, different tissues are characterised by different relaxation times, even if they present a similar composition.  $T_1$  is heavily affected by the strength of the external magnetic field  $B_0$  and is longer than  $T_2$  [62].

Figure 2.3.6 shows a simplified scheme of the net magnetization, when a 90° RF pulse is applied, where  $T_1$  and  $T_2$  are exemplified.



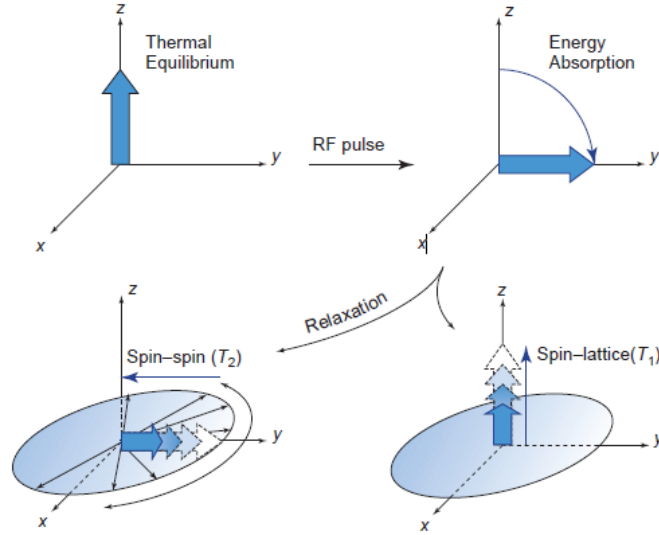


Figure 2.3.6: Schematic overview of both relaxation times,  $T_1$  and  $T_2$ , after the transmission of a  $90^\circ$  RF pulse and the return to the dynamic equilibrium [61]. Figure reproduced with permission by Cambridge University Press.

The transverse component of the net magnetization vector  $\vec{M}_{xy}$  induces an alternating current in the receiver coil, and the magnitude of the detected signals are described by the following sinusoidal functions [61]:

$$s_x(t) = M_0 e^{-t/T_2} \cos(-\omega_0 \times t) \quad (32)$$

$$s_y(t) = M_0 e^{-t/T_2} \sin(-\omega_0 \times t) \quad (33)$$

The signal is acquired during the relaxation processes when the spins release the excess of energy, in the shape of RF waves. The detected signal and its duration are directly related to the amount of spins or protons, the strength of the external magnetic field  $\vec{B}_0$ ,  $T_1$ ,  $T_2$  and the time  $t$  of the measurement [61].

Slightly different precession frequencies of the nuclear spins that occur due to random fluctuations of the local magnetic field, lead to the loss of the original phase coherence. This results in an exponential decay of the signal. The dephasing of the transversal magnetization occurs at a rate  $1/T_2^*$ , which is faster than the  $T_2$ -relaxation alone can explain. It is caused however by both external magnetic field inhomogeneities and changes in susceptibility, characterised by the relaxation time  $T_2'$  [61, 63]. The decay of the transverse magnetization is described by a time constant  $T_2^*$  by the following expression [63]:

$$\frac{1}{T_2^*} = \frac{1}{T_2} + \frac{1}{T_2'} \quad (34)$$

This behaviour is often called “free induction decay” or “FID” [63].

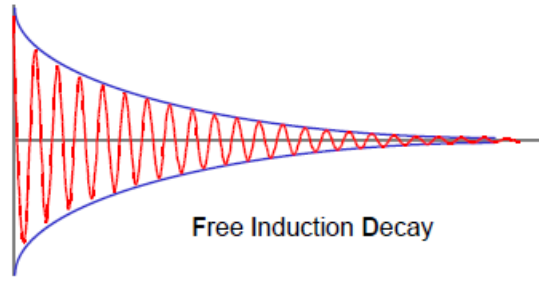


Figure 2.3.7: Representation of the FID signal [63]. Figure reproduced with permission by Evert J. Blink.

When both relaxation processes,  $T_1$  and  $T_2$ , are finished, the net magnetization vector is aligned with the external magnetic field  $\vec{B}_0$ ,  $\vec{M}_z = \vec{M}_0$ ,  $\vec{M}_{xy} = 0$  and the MR-signal is reduced to zero.

The FID is one of four basic types of MR signals, i.e. gradient echo (GRE), spin echo (SE) and stimulated echo. The description of these MR signals is beyond the scope of this work and can be found in the following literature: [61, 62, 64].

Besides the acquisition of the signal, to generate an image, it is crucial to know how the magnetization is distributed in the body and associate a signal with its position of origin – the process of encoding spatial information in the MR signal – performed by applying magnetic field gradients in the x-, y- and z directions onto the static  $\vec{B}_0$ -field. This magnetic field gradient  $G$  can be defined by:

$$G(t) = (G_x(t), G_y(t), G_z(t)) = \left( \frac{\partial B_z(t)}{\partial x}, \frac{\partial B_z(t)}{\partial y}, \frac{\partial B_z(t)}{\partial z} \right) \quad (35)$$

where  $G_x$ ,  $G_y$  and  $G_z$  indicate the slope of the gradient fields [62, 65].

In a homogeneous  $\vec{B}_0$  field, the Larmor frequency is not influenced by the position within the (FOV), as opposed to when magnetic gradient fields are superimposed to the main field, resulting in a position dependency of Larmor frequencies, according to the following expression [61]:

$$\omega_0(r, t) = \omega_0 + \gamma G(t)r \quad (36)$$

with  $r$  representing the x-, y- and z-directions.

A slice with thickness  $\Delta z$  comprises a precise range of precession frequencies around  $\gamma B_0$  [61]:

$$\Delta\omega = \gamma G_z \Delta z \quad (37)$$

Moreover, if an RF pulse is then applied with a certain frequency, the protons that spin at this same frequency are excited and return a signal [63]. In an MRI sequence, the received signal is encoded in x-, y- and z-direction by the use of these gradient fields: slice encoding, phase encoding and frequency encoding, i.e. with one of the gradients and the application of the excitation RF pulse, the protons in one axial slice experience excitation [59, 63]. Within the selected slice, rows and columns with different phases and frequencies are created when the other two gradients are

switched on [59]. The emitted signal contains a complex amount of information, combining different frequencies, phases and amplitudes of RF waves. These data are collected and saved in a matrix, known as k-space, which is the representation of the spatial distribution of transverse magnetization. The process of MRI acquisition consists of filling the k-space line by line and then the image is reconstructed using a Fourier transformation [64, 65].

## 2.4 Image Guided Radiotherapy

### 2.4.1 IGRT techniques and ART

Temporal variations in patient and/or organ position and shape throughout the radiotherapy treatment are a major source of concern as they can compromise the clinical results by poor dose coverage of the target volume and/or overdosage of the surrounding OARs [35]. The anatomical variations can have a systematic or a random nature: the first one represents a consistent divergence between patient's or organs' planned position and/or shape and that when the treatment delivery takes place, also known as treatment preparation error [33]. The random component represents patient/organ position and/or shape random variations during the radiotherapy course, which are also known as treatment execution errors [33]. All variations need to be monitored over time and can potentially be accounted for, being their effect in the treatment eliminated or minimised, via tumour tracking or gating techniques and plan adaptations strategies [33, 35].

IGRT is an imaging technique used for patient surveillance whose purpose is the detection and correction for patient set-up errors, patient movement errors, organ movement and organ changes, allowing patient positioning and monitoring to be target volume oriented [35]. It represents an important step towards a more precise and accurate dose placement within the body, since it guides the treatment on a daily basis, aiming simultaneously at reducing the treatment margins (GTV; CTV; PTV), without compromising the clinical outcome [35, 66, 67]. Using smaller treatment margins enables not only the delivery of less dose to the surrounding healthy tissues, but also a dose escalation to the tumour. With a higher total dose being delivered to the tumour, the therapeutic effect is reached with less fractions, under a hypofractionated scheme [67]. Moreover, IGRT enables a non-uniform dose pattern according to intra-tumoural heterogeneity. Finally, the image-based detection and quantification of anatomical changes during treatment enables the integration of adaptive radiotherapy (ART), which means the modification of the treatment plan during the treatment course [67, 68]. ART comprises IGRT techniques, which use additional information about patient specific anatomical variations, and this knowledge is then introduced into the plan and dose-delivery optimisation during the treatment course [11].

There are several IGRT techniques commercially available, which can be categorised into non-ionising- and ionising radiation-based systems [69].

The non-ionising based systems may employ US, optical surface systems, electromagnetic tracking systems or in-room MRI systems [69, 70]:

- In-room US-based system has been used since the late 1990s and it acquires 3D images, which help align the target and monitor its position, applying in-treatment motion correction;
- Surface guided radiotherapy (SGRT) allows for patient positioning and permanent monitoring of the patient surface throughout the treatment session, being used for intra- and inter-fractional motion. A 3D model of the patient's surface is generated, including the information about the geometric relationship to the isocentre. For each treatment fraction the patient's surface is scanned and compared to the planned 3D model and using a rigid

body transformation, the systems perform a least-square fit to minimise the difference between both models and the patient can be positioned as planned. Intra-fractional position monitoring can also be performed, for either gating, when the beam is delivered only at a defined position of the target, or repositioning of the target for correction. One of the systems of interest for the present study is the ExacTrac Dynamic, an automated SGRT and IGRT system, and a detailed description of its positioning and monitoring strategy will follow in section 2.4.4;

- Electromagnetic tracking systems (Calipso System, Varian Medical System) use electromagnetic transponders, which are implanted within the tumour. A detector array system is used throughout the treatment to track in real time the transponders;
- In-room MRI systems: a low-field MR-linac (MRIdian, ViewRay Inc., Oakwood Village, OH, USA) and a high-field MR-linac (Elekta Unity, Elekta AB, Stockholm, Sweden) were already clinically available. Another system of interest for the present study is the low-field MR-linac and a detailed description of its positioning and monitoring strategy will follow in section 2.4.3.

The ionising radiation based systems include static and real time tracking, and use either kV, MV or hybrid methods [69, 70]. Below some of the systems are briefly explained:

- the EPID, which records the MV linac beam as a 2D projection, can be used for pre-treatment patient set-up, and the 2D image is compared to a DRR. The EPID was developed in the 1980s as a replacement for film and is rather simple to use as the image and the therapeutic MV beam have the same isocentre. Nevertheless, due to the dominant Compton Effect, the image has low soft tissue contrast, and the bony structures are preferably used for patient set-up. Additionally, EPID systems are unable to detect and quantify certain rotations;
- CBCT scanners consist of an independent retractable X-ray source and a 2D detector panel mounted onto the linac. Prior to treatment delivery, several 2D projections are acquired while the kV source and the detector rotate around the patient and a 3D reconstruction of the patient's anatomy is acquired. This volumetric image can be registered to the patient's planning CT aiming at precisely position the patient according to the daily anatomy. This technique has allowed smaller margins and a reduction in integral dose to surrounding OARs when compared to surrogates for target position, like skin tattoos or bony anatomy [71, 72];
- 2D kV stereoscopic imaging (CyberKnife, Accuray Inc., Madison, Wisconsin): the CyberKnife robotic radiosurgery system consists of a linac mounted on an industrial robotic manipulator arm. Image-guidance during the treatment session is provided by the acquisition of X-ray images: two orthogonal X-ray imaging systems are mounted on the ceiling and are used to generate stereoscopic images, at periodic intervals, and two flat panel floor detectors. This information is then used as input to determine the position of the robotic manipulator arm;
- Optical/thermal image and 2D kV stereoscopic imaging (EXTD system): a detailed description of this positioning and monitoring strategy will follow in section 2.4.4.

The integration of ART is becoming more broadly available in clinical practice [11]. The various steps of an adaptive patient treatment workflow are shown below in Figure 2.4.1, where two feedback loops are represented. Every patient treatment starts with a pre-treatment plan and the adaptive workflow can be either performed online (inner loop) or offline (outer loop) [33]. Online and offline ART strategies concern to whether the patient is positioned on the treatment couch while the verification is being performed and the corresponding corrections would be applied during that same fraction or only after completing the treatment fraction [70].

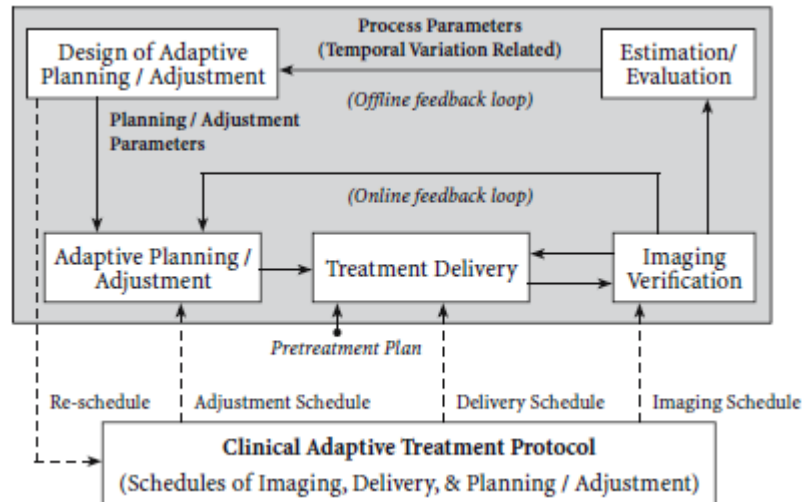


Figure 2.4.1: Schematic representation of an adaptive radiotherapy system [33]. Figure reproduced with permission by Springer Nature.

Offline ART is mostly referring to systematic and progressive alterations, which happen during the cycle of treatment, like patient weight loss and tumour morphological changes [68].

However, many treatment variations, such as inter-fractional target or adjacent organ displacement, and OARs deformation will take place in shorter time intervals, for instance, over one treatment fraction. In these situations offline ART is insufficient to account for these changes. Online ART is the most suitable process to take into consideration temporal and stochastic changes detected in each treatment fraction, while the patient remains in the treatment position [68]. To perform online ART, imaging, fast re-planning, plan review and an acceptable procedure for patient-specific QA is necessary. The benefit from online plan adaptation has already been reported for a wide range of indications [73-75]. Online ART can be implemented in two different situations: online right before a treatment fraction is delivered, or the plan is being automatically adapted simultaneously while the treatment is being delivered [68]. CyberKnife or Vero systems have been implementing real-time ART [68]. The clinical introduction of the MR-linac, for instance, brought the possibility of applying and performing online adaptation workflows, before the treatment delivery begins, in a daily basis. This technique is, however, described more thoroughly in section 2.4.3.

### 2.4.2 SRT, SRS and SBRT

Stereotactic radiosurgery (SRS), stereotactic radiotherapy (SRT) and stereotactic body radiotherapy (SBRT) are defined as treatment methods of radiotherapy that accurately deliver a high radiation dose, of 8 to 50 Gy, in one up to 5 treatment sessions (hypofractionated radiotherapy) [76, 77]. SRS (single-fraction treatment) and SRT are limited to intracranial lesions, while SBRT is defined as treatment to tumours outside of the brain.

The larger the target volumes are, the larger the volume of normal tissue receiving ionising radiation is going to be, and this consequently increases the toxicity to normal tissues. Moreover, the higher the applied single daily dose, the more dose is going to be received by the surrounding normal tissues and critical organs. So that the toxicity of the adjacent critical organs and normal tissues are kept low, stereotactic treatments are commonly delivered to smaller target volumes [77]. The development of these treatment methods could move forward due to technological advances in image guidance and treatment delivery techniques, allowing for the delivery of high doses to target volumes with smaller margins and high gradients outside of the target [76].

To perform stereotactic treatments, conventional medical linacs were adapted and different technologies and hardware and software tools have been incorporated into their designs: the beam produced and its modelling, treatment delivery, MLCs, dose rate, specialised treatment planning and IGRT techniques used, gantry mounted systems but also room-mounted system [17]. Similarly to all new technologies, these dedicated machines and techniques require specialised QA methods for an adequate irradiation delivery [78-80].

The choice of IGRT modality for stereotactic treatments depends on several factors: the necessity to avoid nearby OARs, the need to image with respect to time, the movement of internal organs or even the position of the patient surface. Whether the lesion or a set-up surrogate are composed of soft tissue or bony tissue, how well can they be visualised when X-ray or MR images are acquired, is also a crucial aspect when deciding on which IGRT technique to use, and, perhaps, most importantly, the availability of equipment in the department [17].

### 2.4.3 MRIdian linac

The MRIdian linac is a hybrid system, integrating a conventional linac and an MR scanner for MR-guided radiotherapy (MRgRT), with the possibility of online ART and automated beam gating (see Figures 2.1.8 and 2.1.9) [12]. The possibility of having simultaneous target imaging and radiotherapy delivery was the inspiration for the development of a hybrid MRI/radiotherapy machine. Additionally, it was motivated by the possibility of an improved treatment position verification as well as a reduction of the target margins, enabled by the improved soft tissue contrast of MRI, as well as target monitoring during treatment, with no extra dose delivered to the patient [59, 69].

The MRIdian linac system integrates an MR scanner, which enables pre- and post-treatment MR imaging. For intra-fraction image guidance, continuous monitoring of the position of the target is

enabled by the acquisition of 2D cine sagittal MR images, allowing not only to monitor the target's movement but also the delivery of an automated gated beam [16]. The radiation isocentre coincides with the imaging isocentre, enabling patient imaging before and during therapy delivery.

The MR imaging unit of the system provides a 50 cm diameter spherical field of view (DSV), where a geometric accuracy of the MR images better than 1 mm and 2 mm, on average, within a 20 cm and 35 cm DSV, respectively, is assured by the vendor [31, 59]. A whole-body RF transmit coil and two surface receive coils, anterior and posterior of the patient, are available: a coil pair for the treatment of tumours located in the thoracic, abdominal or pelvic area, and a coil pair for the treatment of head and neck tumours [81].

For both volumetric imaging and cine sagittal MRI, the true fast imaging with steady state precession (TRUFI) pulse sequence is used in the clinical mode. This is a type of balanced steady-state free precession (bSSFP) sequence, offering a very high signal-to-noise ratio and a  $T_2/T_1$ -weighted image contrast [82, 83]. Generally, this sequence is not suited for diagnostic purposes, but has however the advantageous characteristic of being robust against motion and flow, being also suitable for the continuous imaging with the quality needed for real-time tracking of tissues during treatment delivery [82, 84].

### **Online MRgRT workflow at the MRIdian**

For initial treatment planning an MR simulation scan of the patient is acquired, known as planning MR scan. Additionally, since MR images do not capture information about electron density information, essential for treatment planning, i.e. for dose calculation, a CT scan is also acquired using the same patient setup. The MR image is used as primary image and, via DIR, the CT dataset is registered to the MR image, to obtain the electron density values. These values are then propagated to create a planning synthetic CT. The target volumes (GTV, CTV, PTV) and OARs are delineated on the MR scan and after contour delineation and dose prescription is defined, a baseline treatment plan is generated.

This system allows daily treatment plan adaptation while the patient remains in the treatment position, well known as on-table adaptation. This new treatment plan is based on a daily 3D setup MR scan, which is acquired in the beginning of each treatment fraction. The initial planning MRI, as well as the CT scan, are registered to the daily 3D setup MR image, using DIR, and all delineated structures (target volumes, OARs and help structures), as well as the electron density, are propagated onto the daily 3D setup MR image. The deformed structures are inspected and, if necessary, they can be re-contoured. The baseline treatment plan is then calculated on the 3D setup MR image of the day (in truth, on the daily segmented synthetic CT), based on the patient's latest anatomy, resulting in the so-called predicted dose. In case the plan's constraints are not fulfilled, or a better dose distribution with a better sparing of the OARs and/or an improved dose coverage of the target volume are desirable, a plan adaptation can be performed. Before the delivery of the treatment, the adapted plan is then verified with a secondary MC dose calculation code.

The adaptive treatment planning process is concluded by the delivery of the dose to the target, with a gated treatment beam.



Motion management techniques, such as gating, are implemented to concentrate the dose to the target and avoid dose smearing. They are important when treating tumours in thorax or abdominal region, that may be affected by respiratory motion, cardiac motion, gastrointestinal motility and swallowing [85]. Gating is an active motion management technique, which receives information from a surrogate signal or from a real-time image of the region where the tumour is located, to determine whether the beam delivery is interrupted or not [59]. With this intent, with the 0.35 T MR-linac it is possible to acquire continuous 2D cine sagittal MR images during RT delivery, and the beam is automatically gated through online structure tracking, for which a tracking structure (that resembles the tumour motion) and a boundary have to be defined. During treatment, the tracking structure is deformed automatically from the original image to each of the acquired real-time cine MRI frames. Furthermore, the overlap between both the deformed tracking structure and the boundary structure is constantly calculated and compared to a pre-defined threshold value, called “target out percentage” and usually set to approximately 5% to 10%. If the “target out percentage” is below the pre-defined threshold, the beam delivery is switched on, otherwise the beam is paused until the tracking structure is again positioned within tolerance boundaries [82].

Tumours treated in the MR-linac are mainly located in the abdominal and thoracic regions, where organ motion is more pronounced. These lesions are mostly treated in a SBRT regime, for which smaller margins are necessary, and the ability to dynamically adjust to the daily patient's anatomy is provided by gating management technique as well as online ART [16].

#### 2.4.4 ExacTrac Dynamic

EXTD is a system, which uses both SGRT and IGRT positioning tools. It is used in the radiotherapy environment, not only to accurately place the patient in the treatment position but also to monitor its position throughout the whole fraction. EXTD works as an additional system to standard linacs [86].

Intra-fractional positioning information of the bony anatomy is provided by acquiring stereoscopic X-ray images of the patient, as well as real-time 3D surface imaging for continuous motion detection during treatment delivery [87]. Different in-room SGRT and IGRT strategies are combined:

- Optical structured blue light scanning;
- Thermal imaging;
- Oblique stereoscopic kV X-ray imaging.

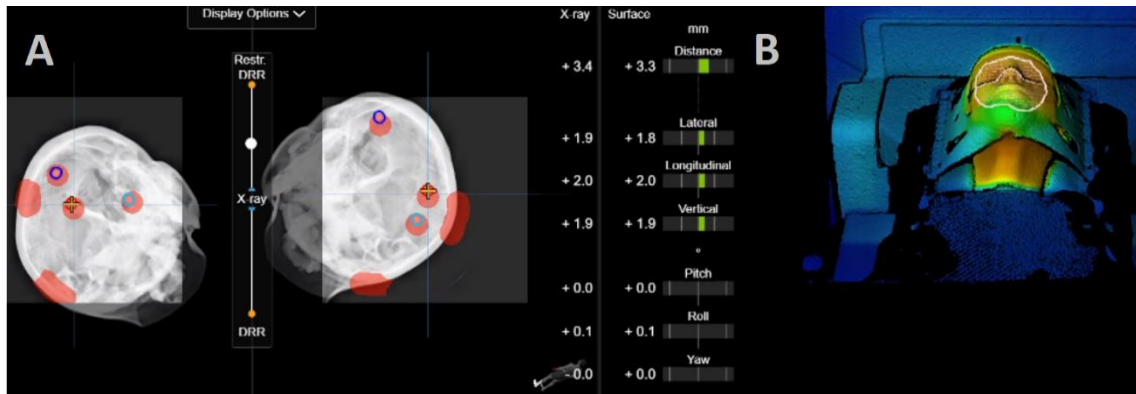


Figure 2.4.2: (A) Combined imaging modalities in the EXT-D system: (A) stereoscopic X-ray imaging, (B) surface optical/thermal imaging [88]. Figure reproduced with permission by John Wiley and Sons.

EXT-D relies on bony anatomy by acquiring stereoscopic X-rays. The X-ray images are registered to DRRs, calculated from the planning CT scan, yielding a rigid body transformation. The comparison of both images result in a deviation of the isocentre position between planned and actual position. The calculated correction shift, in all 6 degrees of freedom (DoF), is transferred to the treatment machine, in order to correctly align the patient's position (see Figure 2.4.2 A) [87].

The system also contains an optical/thermal imaging device, containing a structured light projector, an integrated thermal camera and two stereoscopic high-resolution cameras [86, 87]. The optical/thermal imaging device projects a structured blue light onto the patient surface with a certain pattern. This pattern is recognised by the two optical cameras and with this information a matrix of the patient surface is generated in 3 dimensions. Additionally, the patient is emitting a heat signal, which is acquired by the thermal camera, creating a 2D thermal matrix. These two matrices (3D and 2D) are matched producing a hybrid matrix with spatial and thermal information of each point of the patient surface [87]. The calculated correction shift, in all 6DoF, is also transferred to the treatment machine (see Figure 2.4.2 B).

Figure 2.4.3 shows a schematic illustration of one the linacs important in this work, where the EXT-D system is installed.

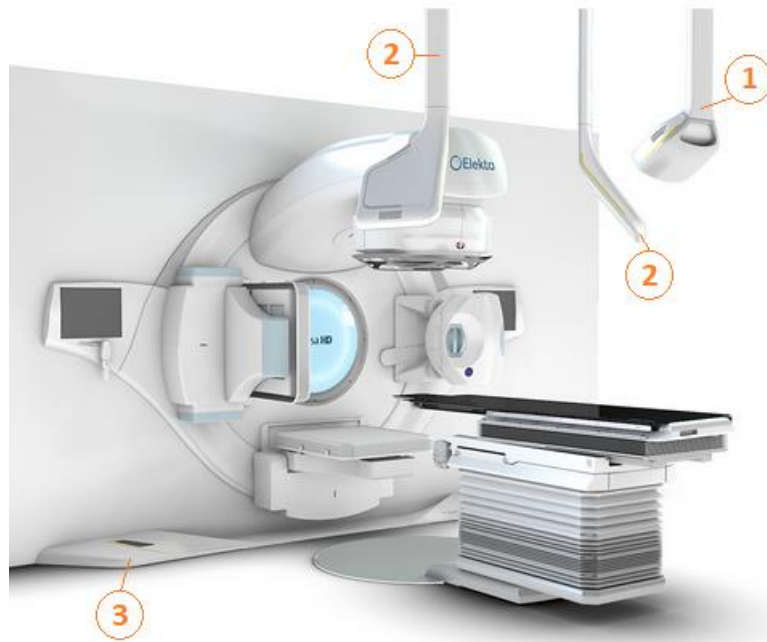


Figure 2.4.3: Design of the EXT-D system, integrated with an Elekta Versa HD linac: 1) thermal camera, 2) flat panel detectors, 3) in-floor cover containing the X-ray tubes, one on either side of the linac [89]. Figure reproduced with permission by Brainlab AG.

Monitoring is performed with surface tracking and the X-ray monitoring system. While the optical/thermal imaging device is constantly acquiring information and providing feedback regarding patient's surface position, the stereoscopic X-ray images can be periodically acquired to verify the position of the internal anatomy [86]. If patient movement is detected and is out of tolerance, the treatment beam is automatically deactivated and the patient needs to be correctly positioned, according to the information acquired by the stereoscopic X-ray imaging, in order to continue the treatment [86, 88].

As opposed to gantry mounted systems, like CBCT, the EXT-D system cannot provide volumetric data, neither soft tissue information [17]. This system is mostly suitable when treating intracranial tumours or tumours in bony structures [88]. However, the monitoring of the patient in real-time, the detection and compensation for intra-fraction tumour motion, also in extracranial regions, whether induced by patient movement or breathing, is also possible when EXT-D system is used [17, 88].

### 3. Summary

Treatment of cancer using photon radiation has rapidly developed over the past years, trying to increase the dose of radiation to the tumour, while sparing organs at risk (OAR) and decreasing healthy tissue toxicity. Not only technological improvements in treatment planning and delivery have their contribution, but also imaging had and still has a very important role.

Nowadays, the importance of imaging techniques goes beyond diagnostic evaluation, accurate tumour localisation and treatment planning. Patient setup and continuous patient monitoring in the course of every treatment fraction are also crucial for precise external beam radiotherapy (EBRT). For instance, patient monitoring during treatment facilitates not only the detection of inter- and intra-fractional anatomical changes but also immediate adjustment of the target position or even the possibility of re-planning. This can be achieved by the daily use of image-guidance, which is possible since different imaging modalities were integrated directly at the linear accelerator (linac). Image-guided radiotherapy (IGRT) has thus expanded the option for radiation oncology by reducing the inherent uncertainties in treatment planning and its delivery.

Current IGRT strategies make use of ultrasound (US), X-ray imaging, magnetic resonance (MR) imaging, computed tomography (CT) or structured light projection (surface imaging). The main imaging modalities important for this thesis were MR imaging and combined surface- and X-ray imaging, for each a different study was designed and performed.

The first study aimed to compare quality of treatment plans for a MR-linac to those for a conventional linac. For this study, 20 anonymised data sets of patients with localised prostate cancer (PCa), who were subjected to definitive radiotherapy and were treated at the LMU University Hospital, were retrospectively selected [12]. This study was divided into two parts: the first part aimed at creating intensity modulated radiotherapy (IMRT) plans for delivery at a low-field strength MR-guided linac (the MRIdian system), which were then evaluated and compared to clinical conventional volumetric modulated arc therapy (VMAT) plans [12]. At first, the original planning target volume (PTV) margins were used in order to compare the performance of both machines, an MR-linac and a standard linac, as well as the treatment planning systems (TPSs). Similar plan quality was achieved, demonstrating that the low-field MR-linac system was able to create IMRT treatment plans that were clinically equivalent as conventional linac-based VMAT, with a comparable quality [12].

Regarding the second part of the plan comparison, its purpose was to investigate the potential of the dosimetric benefits of MR-guided radiotherapy [12]. When treating a patient at the MRIdian linac, online MR-guided adaptive radiotherapy is available and therefore a reduction of the PTV margins is possible without compromising the clinical outcome [12, 57]. For this project, reduced PTV margins were used to create new plans and compare them to the original ones, with original PTV margins [12]. Suitable and comparable target coverages were reached as a better sparing of the surrounding tissues could be achieved [12].

The second study aimed at characterising the patient positioning system, ExacTrac Dynamic (EXTD), installed at the LMU University Hospital [88]. This system consists of a combined surface guided radiotherapy (via optical and thermal imaging) and X-ray imaging system, used for patient

positioning, monitoring and tumour targeting [86]. The examination of the performance of the EXT-D system and its IGRT components was performed: the optical/thermal- and the stereoscopic X-ray imaging systems were exposed to several tests [88]. The positioning consistency between EXT-D and cone-beam computed tomography (CBCT), considered the benchmark for patient setup, was also tested [88]. Furthermore, as the EXT-D system is mostly used in stereotactic radiotherapy (SRT) and stereotactic radiosurgery (SRS), other measurements, such as a hidden target Winston-Lutz test and an end-to-end IGRT test, were performed [88]. Finally, the data relative to the treatment of 14 patients were analysed in order to evaluate and estimate intra-fractional motion. For this investigation, both intra-fractional X-ray data and combined optical/thermal motion data of 142 treatment fractions were used [88]. A cranial open-face mask was utilised to immobilise the patients to the couch during the treatment. The final positioning was performed by EXT-D, which also monitored the patients throughout all fractions. This study demonstrated that this combined system was able to provide an accurate and efficient final positioning of the patients and was also able to detect any movement during the treatment, for both coplanar and non-coplanar couch angles [88].

Modern EBRT techniques are developing towards a more and more accurate and precise treatment, by using the information of more sophisticated in-room imaging modalities. The performed studies are necessary steps in the evaluation and implementation of recently introduced innovative clinical IGRT techniques, being able to prove their accuracy and precision.

## 4. Zusammenfassung

Die Behandlung von Krebs mit Photonenstrahlung hat sich in den letzten Jahrzehnten rasant entwickelt, wobei die Strahlendosis im Tumor maximiert, gleichzeitig aber die Risikoorgane besser geschont und die Toxizität für das normale Gewebe verringert wurden. Dazu haben nicht nur technologische Verbesserungen bei der Behandlungsplanung und -durchführung beigetragen, sondern auch die Bildgebung spielte und spielt dabei eine sehr wichtige Rolle.

Heutzutage geht die Bedeutung der bildgebenden Verfahren über die diagnostische Bewertung, die genaue Tumorlokalisierung und die Behandlungsplanung hinaus. Für eine präzise externe Strahlentherapie (EBRT) sind auch die Patienteneinstellung und die Echtzeitüberwachung des Patienten während aller Behandlungsfractionen von entscheidender Bedeutung. So ermöglicht die Patientenüberwachung während der Behandlung nicht nur die Erkennung inter- und intrafractioneller anatomischer Abweichungen, sondern auch die sofortige Korrektur der Zielposition oder sogar die Möglichkeit einer Neuplanung. Dies wird durch den täglichen Einsatz der Bildführung erreicht, die durch die Integration verschiedener Bildgebungsmodalitäten direkt am Linearbeschleuniger (Linac) ermöglicht wird. Die bildgesteuerte Strahlentherapie (IGRT) hat somit die Möglichkeiten der Radioonkologie erweitert, indem sie die inhärenten Unsicherheiten bei der Behandlungsplanung und -durchführung verringert.

Bei den derzeitigen IGRT-Strategien werden Ultraschall (US), Röntgenbilder, Magnetresonanztomographie (MR), Computertomographie (CT) oder die Projektion von Lichtmustern (Oberflächenbildgebung) verwendet. Die wichtigsten Bildgebungsmodalitäten für diese Arbeit waren die MR-Bildgebung und die kombinierte Oberflächen- und Röntgenbildgebung, für die jeweils eine eigene Studie konzipiert und durchgeführt wurde.

Ziel der ersten Studie war es, die Qualität der Behandlungspläne für einen MR-Linac mit denen für einen konventionellen Linac zu vergleichen. Dafür wurden 20 anonymisierte Datensätze von Patienten mit lokalisiertem Prostatakrebs, die sich am Universitätsklinikum der LMU einer definitiven Strahlentherapie unterzogen, retrospektiv ausgewählt. Die Studie war in zwei Teile gegliedert: Der erste Teil zielte auf die Erstellung von Plänen für die intensitätsmodulierte Strahlentherapie (IMRT) an einem MR-gesteuerten Linac mit niedriger Feldstärke (dem MRIdian-System) ab, die dann ausgewertet und mit klinischen Plänen für die volumetrisch modulierte arc therapie (VMAT) am konventionellen Linac verglichen wurden. Um die Qualität der beiden Geräte, MR-Linac und Standard-Linac, und der zugehörigen Behandlungsplanungssysteme (TPS) vergleichen zu können, wurden die Planungszielvolumen (PTV) mit ursprünglichen Sicherheitssäumen verwendet. Beide Systeme zeigen eine vergleichbare Planqualität, was zeigt, dass am MRIdian Linac IMRT-Pläne erstellt und abgestrahlt werden können, die dosimetrisch vergleichbar zu VMAT-Plänen an konventionellen Linacs sind.

Der zweite Teil dieser Planvergleichsstudie hatte zum Ziel, das Potenzial der MR-geführten Strahlentherapie hinsichtlich dosimetrischer Vorteile zu untersuchen. Bei der Behandlung eines Patienten am MRIdian-Linac steht die MR-geführte online-adaptive Strahlentherapie zur Verfügung, so dass eine Reduzierung der Sicherheitssäume möglich ist, ohne das klinische Ergebnis zu beeinträchtigen. In diesem Projekt wurden kleinere PTVs mit reduzierten Sicherheitssäumen verwendet, um neue Pläne zu erstellen und sie mit den ursprünglichen Plänen zu vergleichen.

So konnte eine bessere Schonung des umliegenden Gewebes bei gleichzeitiger Beibehaltung einer angemessenen Zielvolumenabdeckung erreicht werden.

Die zweite Studie zielte auf die Charakterisierung des Patientenpositionierungssystems ExacTrac Dynamic (EXTD) ab, das in Verbindung mit Linacs der Firma Elekta erstmals am Universitätsklinikum der LMU installiert wurde. EXTD besteht aus einem System für die oberflächengeführte Strahlentherapie mittels optischer und thermischer Bildgebung kombiniert mit einem Röntgenbildgebungssystem, und wird für die Patientenpositionierung sowie die Überwachung von Patienten- bzw. Tumorage eingesetzt. Die Leistung des EXTD-Systems und seiner IGRT-Komponenten wurde untersucht: das optische/thermische und das stereoskopische Röntgenbildgebungssystem wurden mehreren Tests unterzogen. Auch die Übereinstimmung der Positionierung zwischen EXTD und der Kegelstrahl-Computertomographie (CBCT), die als Maßstab für die Patientenpositionierung gilt, wurde getestet. Da das EXTD-System hauptsächlich in der stereotaktischen Strahlentherapie (SRT) und der stereotaktischen Radiochirurgie (SRS) eingesetzt wird, wurden weitere Messungen durchgeführt, wie z. B. ein „versteckter“ Winston-Lutz-Test und ein End-to-End-IGRT-Test. Schließlich wurden die intrafraktionellen Bewegungen und die Abweichungen zwischen geplanter und aktueller Position während der Behandlung von 14 Patienten untersucht. Dazu wurden die intrafraktionellen Röntgen- und kombinierten optischen/thermischen Bewegungsdaten von insgesamt 142 Bestrahlungsfractionen erfasst und analysiert. Die ausgewählten Patienten wurden mit einer gesichtsffenen Kopfmaske auf der Behandlungsliege fixiert und mit EXTD positioniert und überwacht. Diese Studie hat gezeigt, dass das EXTD mit seinem neuen optischen/thermischen Bildgebungssystem ein effizientes und genaues Instrument zur Patientenpositionierung und Lageüberwachung während der Strahlentherapie ist, insbesondere bei Behandlungen mit nicht-koplanaren Tischwinkeln.

Moderne EBRT-Techniken entwickeln sich in Richtung einer immer genaueren und präziseren Behandlung, indem sie die Informationen von immer ausgefeilteren Bildgebungssystem im Behandlungsraum nutzen. Die beiden durchgeführten Untersuchungen beweisen die Qualität und Präzision zweier kürzlich eingeführter innovativer klinischer IGRT-Techniken.

## **5. Paper I: Dosimetric comparison of MR-linac-based IMRT and conventional VMAT treatment plans for prostate cancer**




RESEARCH

Open Access



# Dosimetric comparison of MR-linac-based IMRT and conventional VMAT treatment plans for prostate cancer

Vanessa Da Silva Mendes<sup>1\*</sup> , Lukas Nierer<sup>1</sup>, Minglun Li<sup>1</sup>, Stefanie Corradini<sup>1</sup>, Michael Reiner<sup>1</sup>, Florian Kamp<sup>1,3</sup>, Maximilian Niyazi<sup>1</sup>, Christopher Kurz<sup>1</sup>, Guillaume Landry<sup>1</sup> and Claus Belka<sup>1,2</sup>

## Abstract

**Background:** The aim of this study was to evaluate and compare the performance of intensity modulated radiation therapy (IMRT) plans, planned for low-field strength magnetic resonance (MR) guided linear accelerator (linac) delivery (labelled IMRT MRL plans), and clinical conventional volumetric modulated arc therapy (VMAT) plans, for the treatment of prostate cancer (PCa). Both plans used the original planning target volume (PTV) margins. Additionally, the potential dosimetric benefits of MR-guidance were estimated, by creating IMRT MRL plans using smaller PTV margins.

**Materials and methods:** 20 PCa patients previously treated with conventional VMAT were considered. For each patient, two different IMRT MRL plans using the low-field MR-linac treatment planning system were created: one with original (orig.) PTV margins and the other with reduced (red.) PTV margins. Dose indices related to target coverage, as well as dose-volume histogram (DVH) parameters for the target and organs at risk (OAR) were compared. Additionally, the estimated treatment delivery times and the number of monitor units (MU) of each plan were evaluated.

**Results:** The dose distribution in the high dose region and the target volume DVH parameters ( $D_{98\%}$ ,  $D_{50\%}$ ,  $D_{2\%}$  and  $V_{95\%}$ ) were similar for all three types of treatment plans, with deviations below 1% in most cases. Both IMRT MRL plans (orig. and red. PTV margins) showed similar homogeneity indices (HI), however worse values for the conformity index (CI) were also found when compared to VMAT. The IMRT MRL plans showed similar OAR sparing when the orig. PTV margins were used but a significantly better sparing was feasible when red. PTV margins were applied. Higher number of MU and longer predicted treatment delivery times were seen for both IMRT MRL plans.

**Conclusions:** A comparable plan quality between VMAT and IMRT MRL plans was achieved, when applying the same PTV margin. However, online MR-guided adaptive radiotherapy allows for a reduction of PTV margins. With a red. PTV margin, better sparing of the surrounding tissues can be achieved, while maintaining adequate target coverage. Nonetheless, longer treatment delivery times, characteristic for the IMRT technique, have to be expected.

**Keywords:** IMRT, VMAT, IGRT, MR-guidance, MRIdian linac, Low-field MR-linac, Prostate

## Background

Prostate cancer (PCa) is the second most common solid tumour diagnosed in men of Western Europe and the United States [1]. External beam radiation therapy (EBRT) is one of the treatment options chosen for localised PCa. This technique has evolved substantially over the last decades, maximizing the dose of radiation

\*Correspondence: Vanessa.Mendes@med.uni-muenchen.de  
<sup>1</sup> Department of Radiation Oncology, University Hospital, LMU Munich, Marchioninistraße 15, 81377 Munich, Germany  
Full list of author information is available at the end of the article  
This article belongs to the Topical Collection: Radiation Physics.



© The Author(s) 2021. **Open Access** This article is licensed under a Creative Commons Attribution 4.0 International License, which permits use, sharing, adaptation, distribution and reproduction in any medium or format, as long as you give appropriate credit to the original author(s) and the source, provide a link to the Creative Commons licence, and indicate if changes were made. The images or other third party material in this article are included in the article's Creative Commons licence, unless indicated otherwise in a credit line to the material. If material is not included in the article's Creative Commons licence and your intended use is not permitted by statutory regulation or exceeds the permitted use, you will need to obtain permission directly from the copyright holder. To view a copy of this licence, visit <http://creativecommons.org/licenses/by/4.0/>. The Creative Commons Public Domain Dedication waiver (<http://creativecommons.org/publicdomain/zero/1.0/>) applies to the data made available in this article, unless otherwise stated in a credit line to the data.

delivered to the tumour, while decreasing normal tissue toxicity and sparing organs at risk (OAR). Technological improvements in planning, imaging and delivery of the treatment have led to the development of highly conformal techniques, such as intensity modulated radiation therapy (IMRT) and volumetric modulated arc therapy (VMAT) [2, 3].

Among the advantages reported for VMAT, in comparison to step-and-shoot IMRT, are shorter treatment delivery times, decreasing the influence of intra-fraction motion, the need of less monitor units (MU) and a potential better target coverage and dose conformity [4–6]. It is the technique of choice for the treatment of PCa in our clinic.

Inter- and intra-fractional anatomical variations must be considered when performing EBRT treatments [7, 8]. This explains the importance of image guided radiation therapy (IGRT): it allows for the adjustment of the patients' daily setup and correction of target positioning during treatment delivery, helping enhancing the precision and accuracy of dose delivery [9–12]. Additionally, margins applied to the clinical target volume (CTV), accounting for internal organ motion, variability of the target position and organ deformation, can be reduced, and consequently, the surrounding healthy tissue can be better spared [11, 13]. For PCa, Deutschmann et al. stated that if inter- and intra-fractional variations during RT delivery are properly managed, treatment margin reduction to 3 mm might be reasonable [14].

IGRT strategies in current use are ultrasound (US), 2D X-ray imaging, magnetic resonance (MR) imaging or computed tomography (CT) [11, 15]. In our institution, PCa patients have been treated with VMAT since 2015 under cone beam computed tomography (CBCT)- and US-based IGRT. CBCT is one of the most common IGRT techniques for PCa RT treatments with conventional linear accelerators (linacs) [16]. This technique has, however, some limitations, such as its image quality (image blurring, artefacts and its poor soft tissue contrast) and the dose exposure to the patient [16, 17]. Advantages of US imaging are its real time imaging capability and a good soft tissue contrast, without delivering any further dose to the patient. As limitations, there is the inaccessibility of tissue shielded by bone or air, the susceptibility for imaging artefacts and the user dependency [18].

In recent years, both a low-field (0.35 T) MR-linac (ViewRay MRIdian, ViewRay Inc., Oakwood Village, OH, USA) and a high-field (1.5 T) MR-linac (Elekta Unity, Elekta AB, Stockholm, Sweden) were clinically introduced [19]. The low-field MR-linac, which is the system of interest for the current study, is a hybrid system, combining a conventional linac and an MR scanner for MR-guided radiotherapy (MRgRT), with the

possibility of automated beam gating. A VMAT dose delivery technique is currently not available. Instead, a step-and-shoot IMRT (ssIMRT) dose delivery technique is used. This hybrid machine is able to acquire daily 3D volumetric MR images, to which a CT image is registered for enabling dose calculation of the anatomy of the day, as well as plan re-optimisation for online plan adaptation. MR images are characterised by an improved soft tissue contrast, which is very important for an accurate delineation of the target volume and surrounding organs. Moreover, with the low-field system 2D cine sagittal MR images can also be acquired during treatment for intra-fraction image guidance, allowing not only to monitor the target's movement but also to deliver a gated treatment beam [20]. The information provided by MR-guidance is well suited for PCa, leading to better visualisation of the prostate and surrounding tissue than CT, thus giving an improved certainty of the position of the tumour [8, 21].

Several studies comparing the plan quality provided by IMRT and VMAT have been conducted through the years [4, 6, 22–34]. Studies comparing the treatment plan quality provided by VMAT and IMRT techniques for conventional linacs found VMAT to have better treatment efficiency and shorter treatment delivery times, as well as better dosimetric outcomes for the target and OARs [4–6, 24–26, 33]. More recently, studies describing MRgRT for lung, spine, prostate, rectum, pancreas, liver and kidney were performed, where the impact of reduced margins and plan adaptation showed that at comparable dose to the target a dose reduction to OARs was possible [8, 27–30, 32, 35–41]. Park et al. performed a treatment plan comparison for PCa between conventional linac-based VMAT plans and the MRIdian's  $^{60}\text{Co}$  predecessor system (MR- $^{60}\text{Co}$ ), where smaller planning target volume (PTV) margins for the MR- $^{60}\text{Co}$ -based IMRT technique were used [29]. The quality of MR- $^{60}\text{Co}$ -based IMRT plans was comparable to the quality presented by VMAT plans. Furthermore, lower doses to the rectum and the bladder were seen for MR- $^{60}\text{Co}$  IMRT plans. Other plan quality comparisons for low-field MR-linac-based IMRT systems were also performed for spine and lung [27–32]. Two other studies investigating and comparing the plan quality of high-field MR-linac-based IMRT plans and conventional linac-based VMAT plans for PCa were found [36, 39]. In both studies, identical PTV margins were used for both techniques, and a comparable plan quality was found between both techniques. At the time of writing, there was no study comparing treatment plan quality between low-field MR-linac IMRT (labelled IMRT MRL in this study) and conventional VMAT plans with identical margins, as well as with the reduced margin clinically used with MRgRT.

The aim of this study was to evaluate and compare the performance of IMRT MRL plans, planned for low-field MR-linac delivery, and clinical conventional linac-based VMAT plans, for the treatment of PCa. We evaluated the plan quality in terms of dose-volume histogram (DVH) parameters, as well as the conformity and homogeneity of the dose distribution. Furthermore, estimated treatment delivery times and number of MU were compared. Additionally, the potential benefit of MR-guidance was estimated, by using PTV margins adjusted for online adaptive MRgRT, as currently clinically adopted in our institution.

## Materials and methods

### Patient data and PTV margin concept

20 anonymized data sets of patients with localised PCa undergoing definitive radiotherapy (low and intermediate risk) [42] and treated at our institution from June 2017 to September 2019, were retrospectively selected for this planning study. Depending on the risk stratification, the prescribed dose was 74 Gy to the PTV in 37 fractions (2 Gy per fraction, daily) for 7 patients affected by low risk PCa, and 76 Gy to the PTV in 38 fractions (2 Gy per fraction, daily) for 13 patients affected by intermediate risk PCa.

Patients were scanned in the supine position using a CT scanner (Toshiba Aquilion LB, Canon Medical Systems, Japan). To provide geometric reproducibility, patients were instructed to have a comfortably filled bladder and an empty rectum. The selected patients were treated using a conventional Elekta Versa HD linear accelerator with an Agility multileaf collimator (MLC) consisting of 160 leaves, with a leaf-width of 5 mm. For image-guidance, two modalities were used: a daily CBCT and an US image. The CBCT was acquired in the beginning of each fraction to align the patient; the US images were captured in real-time during treatment in order to monitor the intra-fraction prostate motion, with the Elekta Clarity Autoscan system (Elekta AB, Stockholm, Sweden).

The CTV and the OARs were contoured on the planning CT data set ( $1 \times 1 \times 3 \text{ mm}^3$ ) by an experienced radiation oncologist and according to the institutional protocol. The CTV delineation depended on the PCa risk presented by the patient: for the low risk group the CTV was only covering the prostate; for the intermediate risk group the proximal seminal vesicles were also included. The orig. PTV margins were defined as an isotropic expansion of 6 mm of the CTV in all directions, except posteriorly, where an expansion of 5 mm towards the rectum was used, following the institutional protocol for CBCT guided treatments. The delineation of the clinical PTV expansion as well as the OARs was done with a

clinical treatment planning system (TPS) Oncentra MasterPlan Version 4.5 (Nucletron B.V., Veenendaal, Netherlands), which is used for delineation in our clinic.

For treatment plans currently delivered at the low-field MR-linac at our clinic, reduced margins adjusted for MRgRT are used [8, 28, 40, 43]. This reduction is supported by the additional information given by MR imaging with its better soft tissue contrast [39], the possibility to perform online adaptation (in case this is deemed necessary by the physician in charge) [40] as well as the delivery of a gated beam based on the 2D cine sagittal MR images acquired during irradiation [43]. This margin, designated in this study as red. PTV margin, was defined as an isotropic expansion of 4 mm of the CTV in all directions, except posteriorly, where an expansion of 3 mm towards the rectum was applied, similarly to what has been suggested and applied for prostate tumours at other institutions [8, 10, 40, 44]. In clinical practice for the MR-linac, delineation is done on an ( $1.5 \times 1.5 \times 1.5 \text{ mm}^3$ ) MRI. In Viewray MRIdian TPS Version 5 (ViewRay Inc., Oakwood Village, OH, USA), contours are always defined as multiples of the resolution of the planning image, leading to an expansion of 4.5 mm of the CTV in all directions, instead of 4 mm, except posteriorly towards the rectum, where an expansion of 3 mm is obtained, as intended.

In this study we used ( $1 \times 1 \times 3 \text{ mm}^3$ ) CT images in the low-field MR-linac TPS for planning. Thus the red. margin was, effectively, an expansion of 4 mm of the CTV in the left-right and anterior direction, while in the superior-inferior direction, as well as posteriorly towards the rectum, an expansion of 3 mm was obtained. For the orig. margin, with an expansion of 6 mm of the CTV in the superior-inferior direction, this feature of the TPS does not cause any changes on the effective margin.

### Planning technique

In this planning study, two sets of IMRT MRL plans were developed and compared to the already existing clinical VMAT plans. Table 1 shows the different specifications for both machines and TPSs investigated in this study. The IMRT MRL plans were generated using the same CT and delineations, except from also applying a reduced PTV margin, as used for the VMAT plans.

### VMAT

VMAT plans were generated using a 6 MV photon beam, with the clinical Monaco Version 5.11.01 TPS (Elekta AB, Stockholm, Sweden) and the Agility MLC. For all patients included in this study a VMAT plan using two coplanar arcs was calculated using a Monte Carlo algorithm, with a calculation grid size of

**Table 1** Machine specific parameters for both linacs and the TPSs parameters used for this study

Device specific parameters	Standard linac	Low-field MR-linac
SAD (cm)	100	90
Linac calibration	At the maximum dose point: 100 MU correspond to 1 Gy	
Effective leaf width (mm)	0.5	0.415
Field size at isocentre (cm <sup>2</sup> )	40 × 40	27.4 × 24.1
Multileaf collimator	Rounded leaf edges	double-stacked, double-focused leaves
IMRT technique	VMAT	sslIMRT
Photon energy (MV)	6	6
Flattening filter	FF	FFF
Static magnetic field (T)	–	0.35
TPS parameters:		
Calculation grid size (cm <sup>3</sup> )	0.3 × 0.3 × 0.3	0.3 × 0.3 × 0.3
Statistical uncertainty (%)	1	1
Dose calculation algorithm	XVMC	KMC

(0.3 cm)<sup>3</sup> and a statistical uncertainty during dose prediction of 1%. These plans were delivered clinically.

#### IMRT MRL

IMRT MRL plans were created using Viewray MRIdian TPS Version 5 (ViewRay Inc., Oakwood Village, OH, USA). The low-field MR-linac system generates a 6 MV flattening-filter-free (FFF) photon beam in the presence of a 0.35 T magnetic field, using the RayZR MLC, a double-stacked and double-focused 138-leaf MLC with 4.15 mm effective leaf-width at isocentre. The dose calculation algorithm is also based on Monte Carlo simulation, with a calculation grid size of (0.3 cm)<sup>3</sup> and a statistical uncertainty during dose prediction of 1%.

In order to mimic a VMAT dose distribution, while using the same isocentre as for the VMAT plans, 17 equally spaced beams, avoiding the couch's top edges in order to avoid dosimetric uncertainty, were chosen to create the IMRT MRL plans.

Treatment plans using two different PTV margins were generated. In scenario 1, orig. PTV margins (used also in the clinical VMAT plans) were used for treatment planning, in order to allow the comparison of the performance of the two machines and TPSs, under similar conditions. In scenario 2, red. PTV margins were used, to estimate the potential DVH-based dosimetric benefits of MRgRT.

All IMRT MRL plans were generated by a single medical physicist. This was not the case for the VMAT plans due to their clinical nature. IMRT MRL plans were also evaluated by an experienced radiation oncologist.

#### Treatment planning objectives

The VMAT plans were not normalised as the final plans are a result of a constrained optimisation, for which at first the constraints for OARs are applied and after that step the algorithm tries to fulfil the target's dose objective. For each patient, both IMRT MRL plans were normalised to the PTV D<sub>95%</sub> achieved by the corresponding VMAT plan. In addition, the plans were generated such that the maximum dose would not exceed 107% of the prescribed dose. The following OARs were included in the analysis: rectum, bladder and femoral heads. Internal clinical guidelines, based on tolerance doses and volumes of the OARs suggested by QUANTEC [45], were followed and are presented in Table 2.

#### Plan evaluation and comparison

VMAT dose cubes were imported into the low-field MR-linac TPS in order to analyse and compare all the plans using a single system. The PTV dose and coverage were assessed by the near maximum (D<sub>2%</sub>), the near minimum

**Table 2** Dose-volume constraints used for OARs

OAR	Dose-volume constraint (% of total volume)
Rectum	V <sub>70Gy</sub> < 15% V <sub>60Gy</sub> < 25% V <sub>50Gy</sub> < 50%
Bladder	V <sub>70Gy</sub> < 20% V <sub>60Gy</sub> < 30% V <sub>50Gy</sub> < 50%
Femoral heads	V <sub>50Gy</sub> < 10%



( $D_{98\%}$ ), the median ( $D_{50\%}$ ), as well as the  $V_{95\%}$  of the prescribed dose. The degree of homogeneity of the plans was measured by the homogeneity index (HI), which evaluates the homogeneity of the dose distribution within the PTV [46, 47]. The closer the HI is to zero the higher the homogeneity of the dose distribution will be [48]:

$$HI = \frac{D_{2\%} - D_{98\%}}{D_{50\%}}. \quad (1)$$

The conformity index (CI) considers the shape of the target and reference isodose, as well as the degree of spatial intersection of the two volumes [49, 50]. When a reference isodose is surrounding the PTV completely, not extending to the surrounding tissue, CI equals 1, meaning a perfect hypothetical conformal treatment is achieved. A deviation from perfect conformity gives a lower score. The CI is calculated, according to Paddick for the 95%-isodose, which takes into account the target volume covered by 95% of the prescribed dose ( $V_{95\%PTV}$ ), the target volume ( $V_{PTV}$ ) and the total volume covered by 95% of the prescribed dose ( $V_{95\%isodose}$ ) [51]:

$$CI = \frac{(V_{95\%PTV})^2}{V_{PTV} \times V_{95\%isodose}}. \quad (2)$$

According to our internal clinical guidelines, relevant dose-volume parameters for the OARs, such as  $V_{70Gy}$ ,  $V_{60Gy}$ ,  $V_{50Gy}$  for the rectum and bladder were reported and compared. For the femoral heads, since a dose of 50 Gy was never achieved, it was decided instead to analyse the near maximum,  $D_{2\%}$ . To evaluate the low dose exposure, total volumes  $V_{40Gy}$  and  $V_{25Gy}$  were chosen, as in a study by Hoffmann et al. [3]. We used the patients' outer contour defined for the superior-inferior extent of the planning CT scans. The average treatment delivery time (from first beam-on to final beam-off, estimated by both TPS) for all three plan scenarios, as well as the number of MU required for each plan, were compared.

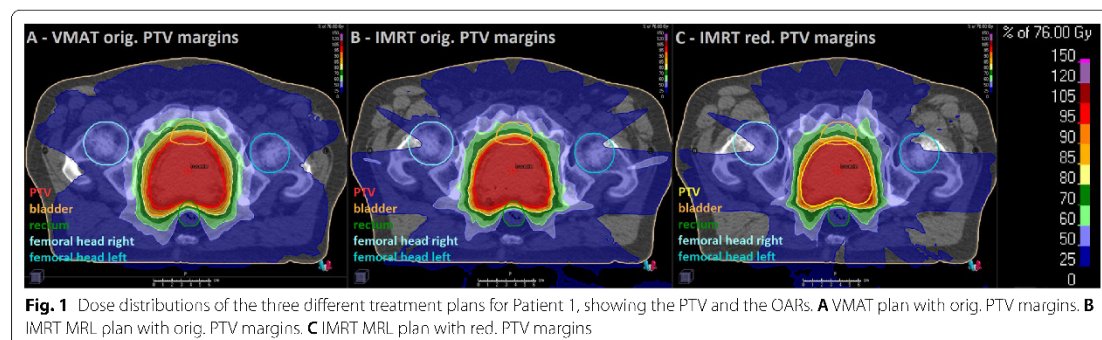
### Statistical analysis

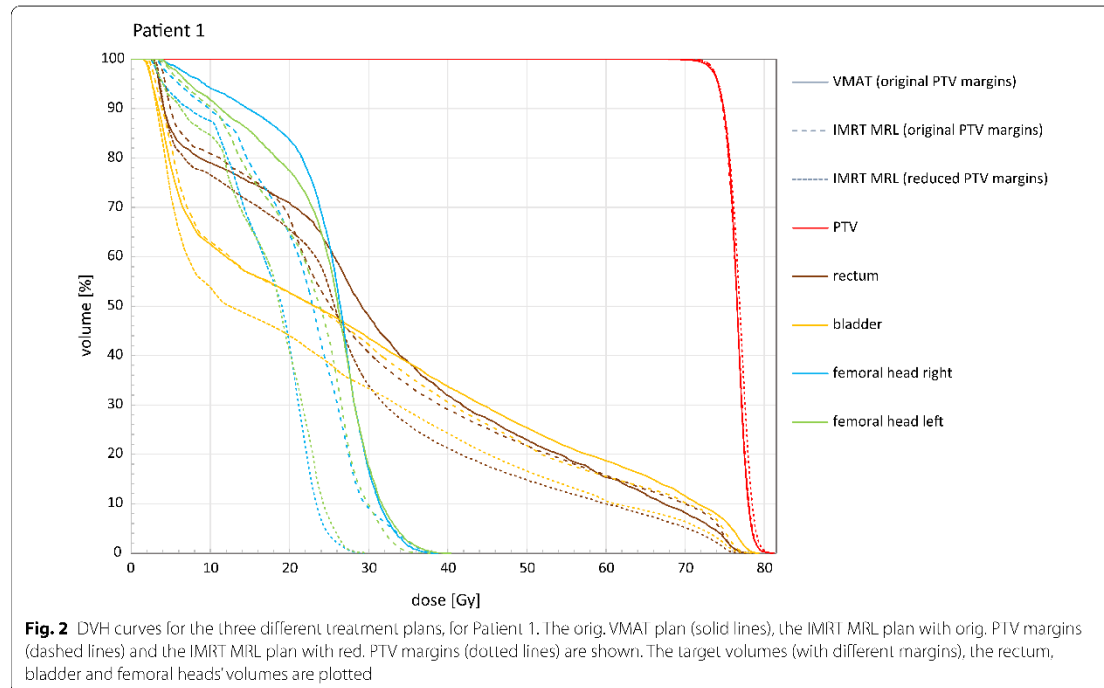
The IBM SPSS Statistics Version 26.0 software (IBM Corporation, Armonk, New York) was used to perform Wilcoxon signed-rank sum tests to investigate differences for each single DVH parameter independently between VMAT and IMRT MRL plans. Differences were considered statistically significant for  $p$  value  $\leq 0.05$ . No correction for multiple testing was done since the analysis was performed for each parameter individually, and comparisons between IMRT MRL plans with orig. and red. margins were not performed.

### Results

Clinically acceptable IMRT MRL plans, with orig. and red. PTV margins, were achieved for all patients. The mean original PTV volume was  $184.6 \pm 49.3$  cc (range 97.4–319.1 cc), whilst the mean PTV volume with red. margins was  $138.1 \pm 40.4$  cc (range 53.6–242.2 cc), resulting in a reduction on average of 25% of the original volume. Exemplary dose distributions of the three different treatment plans, for a prescription dose of 76 Gy, for Patient 1 are shown in Fig. 1. The VMAT and both IMRT MRL dose distributions are visually similar in the high dose region. The VMAT plan PTV dose-volume parameters  $D_{98\%}$  and  $D_{2\%}$  were 73.3 and 78.6 Gy, respectively. For the IMRT MRL plans, the respective values were 73.4 and 78.9 Gy for orig. PTV margins, and 73.2 and 79.3 Gy, for red. PTV margins. The largest differences were seen in the low dose bath. For VMAT/IMRT MRL with orig. PTV margins  $V_{40Gy}$  and  $V_{25Gy}$  were 695 cc and 1848 cc versus 634 cc and 1916 cc, respectively. As expected, the IMRT MRL with red. PTV margins plan allowed better OARs sparing and a further reduction of the low dose bath, with  $V_{40Gy}$  and  $V_{25Gy}$  of 528 cc and 1558 cc, respectively.

The corresponding DVHs of the VMAT plan as well as both IMRT MRL plans are shown in Fig. 2. Both IMRT MRL plans were normalised to the PTV  $D_{95\%}$ , as in the





VMAT plans. The treatment planning constraints for target and OARs were achieved in all plans: DVH curves for target volumes are almost overlapping, while OARs present similar DVH curves for both VMAT and IMRT MRL plans, when orig. PTV margins are applied. However, a reduction of the dose in all OARs for the IMRT MRL red. PTV margins plans was observed, as expected.

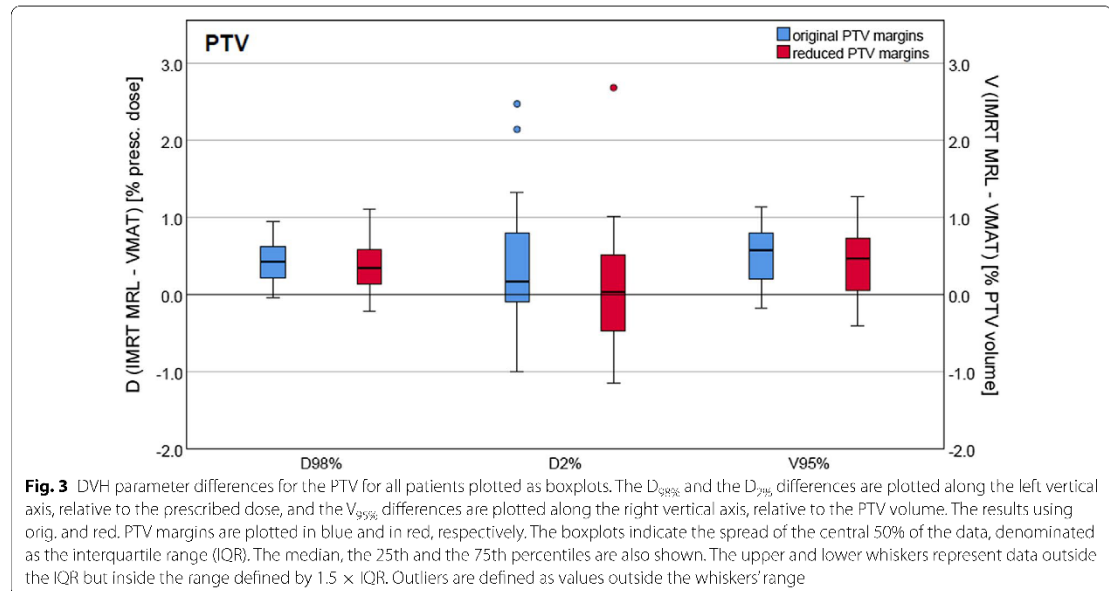
Boxplots of the distribution of the differences of DVH parameters for the target volumes of all patients, between the IMRT MRL and the VMAT plans, for both orig. and red. PTV margins are presented in Fig. 3. The  $D_{98\%}$ ,  $D_{2\%}$  and  $V_{95\%}$  achieved for the IMRT MRL plans for both PTV margins were on average slightly higher than the ones reported for the VMAT plans, with median differences below 0.6%. For a few cases the  $D_{2\%}$  difference exceeded 2% for the IMRT MRL plans. However, the  $D_{2\%}$  was still within the tolerance limits. The Wilcoxon matched-pair signed rank test showed there was no significant difference in  $D_{2\%}$  between VMAT and IMRT MRL ( $p > 0.05$ ), as opposed to  $D_{98\%}$  and  $V_{95\%}$ , where differences were statistically significant ( $p \leq 1 \times 10^{-5}$ ). Deviations between IMRT MRL and VMAT were, however, below 1% in most cases.

The distribution of the differences between dose-volume parameters of the OARs for all patients, between IMRT MRL and VMAT plans, orig. and red. PTV

margins, is presented by the boxplots shown in Fig. 4. When using the orig. PTV margins, the  $V_{70Gy}$  of the rectum was on average 1.7% higher for the IMRT MRL plans than for the VMAT plans ( $p \leq 1 \times 10^{-5}$ ). However, for IMRT MRL plans, the  $V_{60Gy}$  was roughly the same ( $16 \pm 5\%$ ) as for VMAT plans ( $16 \pm 4\%$ ), with no significant difference. The  $V_{50Gy}$  was slightly lower for IMRT MRL ( $22 \pm 6\%$ ) than for VMAT plans ( $24 \pm 6\%$ ), but statistically significant ( $p \leq 1 \times 10^{-5}$ ). For red. PTV margins the  $V_{70Gy}$ ,  $V_{60Gy}$  and  $V_{50Gy}$  were always smaller for IMRT MRL plans, which was statistically significant ( $p \leq 1 \times 10^{-5}$ ), with reductions of 3%, 6% and 9%, respectively.

For the bladder, when planning with the orig. PTV margins, the results indicated that the  $V_{70Gy}$  was approximately the same for both planning techniques, not showing any significant difference ( $p > 0.05$ ). However, both the  $V_{60Gy}$  and  $V_{50Gy}$  were always smaller for the IMRT MRL plans (the reductions were, respectively, on average 0.7%,  $p = 0.019$  and 1.1%,  $p = 0.002$ ). For red. PTV margins, reductions ranging from 4% for  $V_{70Gy}$  to 6% for  $V_{50Gy}$  were observed with  $p \leq 1 \times 10^{-5}$ .

In terms of  $D_{2\%}$  of the femoral heads, when planning with the orig. PTV margins, the IMRT MRL plans indicated on average a lower  $D_{2\%}$  for the left femoral head, with a reduction of nearly 2%,  $p = 0.001$ . Approximately the same  $D_{2\%}$



values were found, for both techniques, for the right femoral head, with  $p > 0.05$ . When using the red. PTV margins, the  $D_{2\%}$  was significantly lower in comparison to the VMAT plans (a reduction of nearly 6% for both left and right femoral heads), with  $p \leq 1 \times 10^{-5}$ .

The HI and CI are reported in Table 3, as well as the significance of the differences between the various modalities. The three modalities achieved a similar HI, with no statistically significant differences ( $p > 0.05$ ). The CI were all  $< 1$  and marginally higher for the VMAT plans than for both IMRT MRL plans, meaning the conformity achieved by VMAT's dose distributions was slightly better, with  $p \leq 0.049$ .

In Table 3 the distribution of the low dose is also summarised, where  $V_{40\text{Gy}}$  and  $V_{25\text{Gy}}$  are reported. Both parameters were larger for the IMRT MRL plans with orig. PTV margins, with a statistically significant difference for the  $V_{25\text{Gy}}$ . As for the IMRT MRL plans with red. PTV margins, the  $V_{40\text{Gy}}$  and  $V_{25\text{Gy}}$  were both smaller compared to the VMAT plans, and the differences were both statistically significant.

Additionally, in Table 3 the plan parameters for treatment efficiency for the three types of plan presented in this study are shown. The number of MU for both IMRT MRL plans were significantly higher than for VMAT: an increase of 17% of the number of MU was reported for the IMRT MRL plans with orig. PTV margins, while for plans with red. PTV margins 25% more MU were needed. Treatment delivery times for IMRT MRL plans were calculated to be approximately 4.5 times longer than treatments delivered

using VMAT plans on a conventional linac, which took on average  $2.1 \pm 0.0 \text{ min}$  ( $p \leq 1 \times 10^{-5}$ ).

## Discussion

In the present planning study, VMAT and IMRT MRL plans with orig. PTV margins showed comparable dosimetric quality, with no clinically relevant differences regarding target coverage and dose to OARs. This is in agreement with the PCa results of Christiansen et al. and van de Schoot et al. for the high-field MR-linac [36, 39], where the same margins were used for both techniques and no clinically relevant differences regarding target coverage or doses to OARs were shown. Yadav et al. and Choi et al. compared low-field MR-linac-based IMRT plans to standard linac-based VMAT plans, for spine stereotactic body radiation therapy (SBRT), and both achieved comparable plan quality in terms of PTV DVH parameters [27, 30]. In our study, equivalent HI for both techniques were found, indicating a similar uniformity of the dose distribution in the target volume. However, better CI were observed for VMAT compared to IMRT MRL plans, corresponding to an increase of the irradiated volume for IMRT MRL orig. PTV margins. This is in contradiction to what Choi et al. observed for spine SBRT, where better CI were found for low-field MR-linac-based IMRT compared to VMAT plans. This disagreement is likely attributable to the different treatment sites, since our results are in agreement with Otto et al., who studied a novel-aperture based algorithm for VMAT treatment

plan optimisation, and compared the resulting plan quality to a standard linac IMRT plan for nasopharyngeal carcinoma. In that study it was suggested that the limited number of angles in an IMRT technique may lead to poorer conformity [52]. Another study, from Palma et al., which investigated and compared 3D conformal radiotherapy with conventional linac IMRT and VMAT techniques for the treatment of PCa also proposed that the additional flexibility in dose delivery afforded by VMAT's variable dose rate might contribute to a better dose conformity [25].

For the OARs, a similar sparing between IMRT MRL and VMAT plans was achieved. For the femoral heads, the IMRT MRL plans indicated a slightly lower, but significant,  $D_{2\%}$  for the left femoral head in comparison to the VMAT plans (a reduction of about 2%), while the  $D_{2\%}$  for the right femoral head was nearly the same for both techniques. Given that the patient structures are relatively symmetric, the difference between left and right femoral heads for orig. PTV margins was not expected. This difference was not seen when analysing the  $D_{2\%}$  values for both femoral heads when red. PTV margins were used. This suggests that a larger sample size might be needed to determine whether this was a systematic effect.

Both  $V_{40Gy}$  and  $V_{25Gy}$  showed significant increases for the IMRT MRL plans. However, while the  $V_{40Gy}$  was only slightly higher in comparison to VMAT, the  $V_{25Gy}$  showed an increase of 14%. This follows the trend seen in Hoffmann et al., who evaluated VMAT and IMRT plans for PCa treatment delivery using a conventional linac. In this study the low dose bath of 40 Gy and 25 Gy isodose volumes, among other parameters, were analysed. Nearly the same  $V_{40Gy}$  values for IMRT and VMAT plans were reported, but a 62% increase for  $V_{25Gy}$  was observed [3].

With red. PTV margins, where the target volume was on average 1.3 times smaller than the orig. PTV, we observed similar DVH parameters for the target volume, while a reduction in the doses to the OARs was noticeable. Park et al. compared the plan quality of low-field MR-linac-based IMRT plans where the PTV volumes were approximately 4 times smaller, to conventional linac-based VMAT plans, for lung SBRT [28]. A better plan quality was attributed to the MR-linac-based IMRT technique, showing, in general, less dose to the

surrounding normal tissue and a better target coverage [28]. Similarly to Park et al., the better outcomes for the OARs were attributed to the margin reduction capability, enabling the irradiation of smaller volumes [28]. This is also the explanation for the lower  $V_{40Gy}$  and  $V_{25Gy}$ , determined for IMRT MRL plans with red. margins.

Several investigations have been made to find the most adequate margins to apply to the CTV for low and intermediate risk prostate cancer patients, considering the use of different types of IGRT and its frequency [53–55]. The choice for our orig. VMAT margins is based on the fact that our CT images have a slice thickness of 3 mm, on previous studies [56], and on our institutional practice and experience, with good tumour control and low toxicity observed among our patients. Naturally, the benefits of using the red. PTV margins for IMRT MRL plans would be less if we had used smaller orig. margins for the VMAT plans, or vice-versa.

For the IMRT MRL plans (with red. PTV margins), as mentioned before, the margin applied was slightly smaller in the superior-inferior direction than 4 mm due to the TPS' features and the resolution of the CT used for treatment planning. Consequently, the dose to the OARs may have been slightly more reduced than with a 4 mm superior-inferior expansion, although it is not clear to what extent.

In terms of treatment delivery efficiency, the results suggested that the VMAT technique presents a higher efficiency in both scenarios, which concurs with other studies [27, 28, 30]. According to Choi et al., the average number of MU required for the low-field MR-linac-based IMRT plans was approximately 3 times larger than that for VMAT [27], whilst for Park et al. this number was 2 times larger [28]. In our study, this impact was less dramatic since this value was below 1.3 times for both plans, with orig. and with red. PTV margins.

However, it is also true that even when using the same delivery technique, the performance of different TPSs using different approaches can vary, leading to different outcomes. The performance of two commercial TPSs, Monaco (Elekta AB, Stockholm, Sweden) and Pinnacle (Philips Medical Systems, Madison, WI) for VMAT treatment plans regarding PCa was studied by Lafond et al. [57]. Both techniques offered clinically acceptable dose distributions with similar delivery times (on average 169 s

(See figure on next page.)

**Fig. 4** DVH parameter differences for the OARs, for all patients, as boxplots are shown.  $V_{70Gy}$ ,  $V_{60Gy}$ ,  $V_{50Gy}$  for **a** rectum and **b** bladder, relative to the rectum and bladder volume, respectively, and  $D_{2\%}$  for **c** femoral heads, relative to the prescribed dose. The results using orig. and red. PTV margins are plotted in blue and in red, respectively. The boxplots indicate the spread of the central 50% of the data, denominated as the IQR (interquartile range). The median, the 25th and the 75th percentiles are also shown. The upper and lower whiskers represent data outside the IQR but inside the range defined by  $1.5 \times$  IQR. Outliers are defined as values outside the whiskers' range



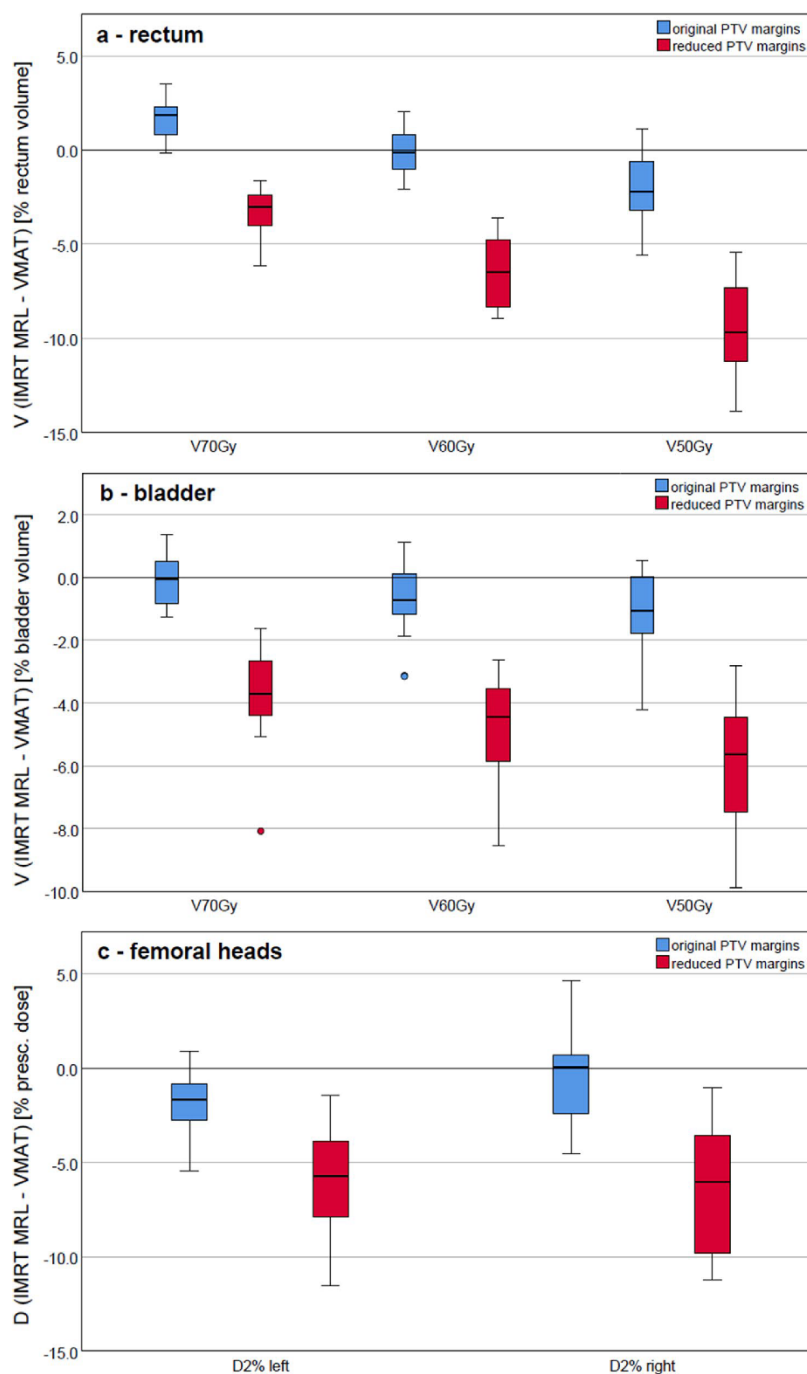


**Fig. 4** (See legend on previous page.)

**Table 3** Homogeneity and conformity indices for orig. VMAT and IMRT MRL plans with orig. PTV margins and red. PTV margins. Additionally,  $V_{40Gy}$  and  $V_{25Gy}$  and the average number of MU per fraction and the estimated treatment delivery time for the VMAT and IMRT MRL plans with orig. and red. PTV margins are shown. The results presented are mean values  $\pm$  standard deviation. The  $p$ -values for the VMAT and IMRT MRL comparisons for both orig. and red. PTV margins are also indicated

	VMAT (orig. PTV margins)	IMRT MRL (orig. PTV margins)	IMRT MRL (red. PTV margins)
Homogeneity (HI)	0.08 $\pm$ 0.01	0.08 $\pm$ 0.01	0.08 $\pm$ 0.01
$p$ value		0.7	0.4
Conformity (CI)	0.89 $\pm$ 0.05	0.87 $\pm$ 0.06	0.85 $\pm$ 0.05
$p$ value		0.049	0.016
$V_{40Gy}$ (% relative to VMAT)	100 $\pm$ 0.0	103 $\pm$ 8	81 $\pm$ 9
$p$ value		0.1	$\leq 1 \times 10^{-5}$
$V_{25Gy}$ (% relative to VMAT)	100 $\pm$ 0.0	114 $\pm$ 9	89 $\pm$ 11
$p$ value		$\leq 1 \times 10^{-5}$	0.001
MU	639 $\pm$ 69	748 $\pm$ 61	796 $\pm$ 75
$p$ value		$\leq 1 \times 10^{-5}$	$\leq 1 \times 10^{-5}$
Predicted treatment delivery time (min)	2.1 $\pm$ 0.0	9.4 $\pm$ 0.8	9.1 $\pm$ 0.6
$p$ value		$\leq 1 \times 10^{-5}$	$1 \times 10^{-5}$

for Monaco and 165 s for Pinnacle), despite the higher number of MU provided by Monaco, which needed 688 MU on average, as opposed to 452 MU for Pinnacle [57]. Moreover, Wiezorek et al. compared different rotational and static IMRT techniques for head-and-neck tumour treatment plans, where a comparable target coverage was achieved by all treatment plans [58]. However, discrepancies were found when analysing the treatment delivery times and the required number of MU. While the number of MU was, on average, slightly higher for the VMAT plans planned with Monaco (501 MU) in comparison to the VMAT plans planned with Eclipse (Varian, Palo Alto, USA) (437 MU), the shortest mean treatment times were associated with the latter, delivered in 2.5 min on average, in contrast to 9 min [58].

All three studies already mentioned, which compared low-field MR-linac-based IMRT to conventional linac-based VMAT plans, [27, 28, 30], reported beam-on times and not the estimated treatment delivery times. While Yadav et al. reported a beam-on time of approximately 2 times longer for MR-linac-based IMRT compared to VMAT, for Park et al. and for Choi et al. these values were, respectively, 4 times and 7 times larger. In our study, we decided to report the estimated treatment delivery time, since this represents the actual time needed for the treatment to be delivered, for which not

only the beam-on time counts, but also the overhead to reposition the gantry and the time the MLC needs to form each segment are taken into consideration [26]. Treatment delivery times for both IMRT MRL plans were calculated to be below 4.5 times longer than treatments delivered using VMAT. The longer calculated treatment delivery times can be explained by various factors, such as the larger number of MU and the multiple field arrangement. This could raise concerns about a possible inaccurate delivery of the treatments due to patient and/or organ motion, with the consequence of dose delivery differences from that planned. However, the low-field MR-linac system has the ability to monitor the internal anatomy motion continuously and to deliver a gated beam, by the use of online cine MR images while the IMRT MRL plans are being delivered. This contributes for improved certainty of the position of the tumour and improved patient safety.

The reported differences between clinical VMAT and IMRT MRL plans (orig. PTV margins) were mainly due to differences in machine characteristics. Even though the exact contribution of each factor could not be identified in this study, discrepancies were mostly induced by treatment machine geometries (MLC leaf width, collimator positioning, and dose rate), differing TPSs, treatment techniques and the presence of the magnetic field.

It is important to mention that such studies carry the risk of bias, especially when clinical plans, with a well-established technique, are compared to plans created using a novel technique. Another limiting factor could be the fact that VMAT and IMRT MRL plans were produced by different planners. Nevertheless, the results were consistent and all the IMRT MRL plans were considered clinically acceptable and equivalent to the clinical ones. To evaluate whether performing the DVH analysis of all plans on the same TPS used to generate the IMRT MRL plans introduced a bias in our study, an independent system, Oncentra MasterPlan (Nucletron B.V., Veenendaal, Netherlands), was used for repeated DVH analysis for 5 out of the 20 patients. The DVH parameters for the target volume and the OARs were compared to the ones reported by the MRIdian system and the resulting deviations between both TPSs were always below 0.5%, demonstrating a good agreement.

## Conclusions

This study demonstrated that, under similar conditions, the MRIdian system is capable of delivering PCa treatment plans of similar dosimetric quality as conventional linac-based VMAT plans. Furthermore, a better sparing of the surrounding OARs and healthy tissue is possible due to the margin reduction enabled by online MR image guidance.

# Abbreviations

CBCT: cone beam computed tomography; CI: conformity index; CT: computed tomography; CTV: clinical target volume; DVH: dose-volume histogram; EBRT: external beam radiation therapy; FFF: flattening-filter-free; HI: homogeneity index; IGRT: image guided radiation therapy; IMRT: intensity modulated radiation therapy; linac: linear accelerator; MLC: multileaf collimator; MR: magnetic resonance; MRgRT: MR-guided RT; MU: monitor units; OAR: organ at risk; PCa: prostate cancer; SBRT: stereotactic body radiation therapy; sIMRT: step-and-shoot IMRT; TPS: treatment planning system; US: ultrasound; VMAT: volumetric modulated arc therapy.

# Acknowledgements

The authors thank Matthias Söhn, Sylvia Garny, Roel Shpani and Helmut Weingandt for assistance with treatment planning and discussion of the study. Angela Irask is thanked for support with the MRIdian TPS.

# Authors' contribution

VDSM performed the IMRT/ML treatment planning, performed the statistical analysis and drafted the manuscript. LN assisted in MRL treatment planning, reviewed the manuscript and helped to finalize it. MI, SC assisted in clinical data collection and plan evaluation, reviewed the manuscript and helped to finalize it. MR, FK, MS, CK and GL helped design the study, supervised the analysis, reviewed the manuscript and helped to finalize it. CB and MN conceived the study, supervised the analysis, reviewed the manuscript and helped finalize it. All authors read and approved the final manuscript.

# Funding

Open Access funding enabled and organized by Projekt DEAL. This research project has received funding from ViewRay, Inc.

# Availability of data and materials

The datasets generated and/or analysed during the current study are not publicly available due to patient privacy concerns.

# Declarations

# Ethics approval and consent to participate

This retrospective study was exempt from requiring ethics approval. Bavarian state law (Bayrisches Krankenhausgesetz/Bavarian Hospital Law § 27 Absatz 4 Datenschutz (Data protection)) allows the use of patient data for research, provided that any person's related data are kept anonymous. German radiation protection laws request a regular analysis of outcomes in the sense of quality control and assurance, thus in the case of purely retrospective studies no additional ethical approval is needed under German law.

# Consent for publication

Not applicable.

# Competing interests

The Department of Radiation Oncology of the University Hospital, LMU Munich has research agreements with Elekta, Inc. and ViewRay, Inc.

# Author details

<sup>1</sup>Department of Radiation Oncology, University Hospital, LMU Munich, Marchioninistraße 15, 81377 Munich, Germany. <sup>2</sup>German Cancer Consortium (DKTK), Partner Site Munich, Munich, Germany. <sup>3</sup>Department of Radiation Oncology, Cologne University Hospital, Cologne, Germany.

Received: 11 February 2021 Accepted: 12 July 2021

Published online: 21 July 2021

# References

1. Zaorsky NG, et al. What is the ideal radiotherapy dose to treat prostate cancer? A meta-analysis of biologically equivalent dose escalation. *Radiation Oncol*. 2015;11(5):295–300.
2. Fischer Valuck BW, Rao YJ, Michalski JM. Intensity modulated radiotherapy for prostate cancer. *Transl Androl Urol*. 2018;7(3):297–307.
3. Ioffmann M, et al. Analysis of a volumetric-modulated arc therapy (VMAT) single phase prostate template as a class solution. *Rep Pract Oncol Radiother*. 2019;24(1):92–6.
4. Khan M, et al. Dosimetric and radiobiological characterizations of prostate intensity-modulated radiotherapy and volumetric-modulated arc therapy: a single-institution review of ninety cases. *J Med Phys*. 2016;41(3):162–8.
5. White P, et al. Volumetric intensity-modulated arc therapy vs conventional intensity modulated radiation therapy in nasopharyngeal carcinoma: a dosimetric study. *J Radiat Res*. 2013;54(3):532–45.
6. Kawashima M, et al. Comparison of total MU and segment areas in VMAT and step-and-shoot IMRT plans. *Radiol Phys Technol*. 2013;6(1):14–20.
7. Dang A, et al. Image-guided radiotherapy for prostate cancer. *Transl Androl Urol*. 2018;7(3):308–20.
8. Ietar SU, et al. Clinical implementation of magnetic resonance imaging guided adaptive radiotherapy for localized prostate cancer. *Phys Imaging Radiat Oncol*. 2019;9:69–76.
9. Yan D, et al. Adaptive radiation therapy. *Phys Med Biol*. 1997;42(1):173–32.
10. Kim J-i, et al. Retrospective study comparing MR-guided radiation therapy (MRgRT) setup strategies for prostate treatment: repositioning vs. replanning. *Radiat Oncol*. 2019;14(1):139.
11. Sterzing F, et al. Image-guided radiotherapy: a new dimension in radiation oncology. *Dtsch Arzteblatt Int*. 2011;108(16):274–80.
12. Li M, et al. A dosimetric comparison between conventional fractionated and hypofractionated image-guided radiation therapies for localized prostate cancer. *Chin Med J (Engl)*. 2016;129(12):1447–54.
13. Zelefsky MJ, et al. Improved clinical outcomes with high-dose image-guided radiotherapy compared with non-IGRT for the treatment of clinically localized prostate cancer. *Int J Radiat Oncol Biol Phys*. 2012;84(1):125–9.
14. Deutschmann H, et al. First clinical release of an online, adaptive, aperture-based image-guided radiotherapy strategy in intensity-modulated radiotherapy to correct for inter- and intrafractional rotations of the prostate. *Int J Radiat Oncol Biol Phys*. 2012;83(5):1624–32.
15. Langen KM, et al. Observations on real-time prostate g and motion using electromagnetic tracking. *Int J Radiat Oncol Biol Phys*. 2008;71(4):1084–90.
16. Nicosia J, et al. Daily dosimetric variation between image-guided volumetric modulated arc radiotherapy and MR-guided daily adaptive radiotherapy for prostate cancer stereotactic body radiotherapy. *Acta Oncol*. 2020;60(2):1–7.
17. McParland NA. kV-cone beam CT as an IGR tool in the treatment of early stage prostate cancer: a literature review. *J Med Imaging Radiat Sci*. 2009;40(1):9–14.
18. Camps SM, et al. The use of ultrasound imaging in the external beam radiotherapy workflow of prostate cancer patients. *BioMed Res Int*. 2018;2018:7569590.
19. Corradini S, et al. MR-guidance in clinical reality: current treatment challenges and future perspectives. *Radiat Oncol (Lond Engl)*. 2019;14(1):92–2.
20. Mittauer K, et al. A new era of image guidance with magnetic resonance-guided radiation therapy for abdominal and thoracic malignancies. *Cureus*. 2018;10(4):e2422.
21. Khoo VS, Ioon DI. New developments in MRI for target volume delineation in radiotherapy. *Br J Radiol*. 2006;79(Spec No 1):S2–5.
22. Herman IT, et al. Dosimetric comparison between IMRT delivery modes: Step-and-shoot, sliding window, and volumetric modulated arc therapy—for whole pelvis radiation therapy of intermediate to high risk prostate adenocarcinoma. *J Med Phys*. 2013;38(4):165–72.
23. Slosarek K, et al. Integral dose: comparison between four techniques for prostate radiotherapy. *Rep Pract Oncol Radiother J Great Poland Cancer Center Poznan Pol Soc Radiat Oncol*. 2014;20(2):99–103.
24. Verbakel WF, et al. Volumetric intensity modulated arc therapy vs. conventional IMRT in head-and-neck cancer: a comparative planning and dosimetric study. *Int J Radiat Oncol Biol Phys*. 2009;74(1):252–9.
25. Palma D, et al. Volumetric modulated arc therapy for delivery of prostate radiotherapy: comparison with intensity modulated radiotherapy and three-dimensional conformal radiotherapy. *Int J Radiat Oncol Biol Phys*. 2008;72(4):996–1001.
26. Scorselli M, et al. Volumetric modulation arc radiotherapy compared with static gantry intensity-modulated radiotherapy for malignant pleural

- mesothelioma tumor: a feasibility study. *Int J Radiat Oncol Biol Phys.* 2010;77(3):942–9.
27. Choi CH, et al. Comparison of treatment plan quality among MRI based IMRT with a linac, MRI-based IMRT with tri-Co-60 sources, and VMAT for spine SABR. *PLoS ONE.* 2019;14(7):e0220039.
  28. Park JM, et al. Comparison of treatment plans between IMRT with MR-linac and VMAT for lung SABR. *Radiat Oncol.* 2019;14(1):105.
  29. Park JM, et al. Treatment plan comparison between Tri-Co-60 magnetic-resonance image-guided radiation therapy and volumetric modulated arc therapy for prostate cancer. *Oncotarget.* 2017;8(53):91174–84.
  30. Yadav P, et al. Dosimetric study for spine stereotactic body radiation therapy: magnetic resonance guided linear accelerator versus volumetric modulated arc therapy. *Radiol Oncol.* 2019;53(3):362–8.
  31. Merna C, et al. A treatment planning comparison between modulated tri-cobalt-60 teletherapy and linear accelerator-based stereotactic body radiotherapy for central early-stage non-small cell lung cancer. *Med Dosim.* 2016;41(1):87–91.
  32. Park JM, et al. A comparative planning study for lung SABR between tri-Co-60 magnetic resonance image guided radiation therapy system and volumetric modulated arc therapy. *Radiother Oncol.* 2016;120(2):279–85.
  33. Sale C, Moloney P. Dose comparisons for conformal, IMRT and VMAT prostate plans. *J Med Imaging Radiat Oncol.* 2011;55(6):611–21.
  34. Nguyen BI, et al. Optimising the dosimetric quality and efficiency of post-prostatectomy radiotherapy: a planning study comparing the performance of volumetric-modulated arc therapy (VMAT) with an optimised seven-field intensity-modulated radiotherapy (IMRT) technique. *J Med Imaging Radiat Oncol.* 2012;56(2):211–9.
  35. Bohoudi O, et al. Fast and robust online adaptive planning in stereotactic MR-guided adaptive radiation therapy (SMART) for pancreatic cancer. *Radiother Oncol.* 2017;125(3):439–44.
  36. Christiansen RL, et al. Plan quality for high risk prostate cancer treated with high field magnetic resonance imaging guided radiotherapy. *Phys Imaging Radiat Oncol.* 2018;7:1–8.
  37. Henke LE, et al. Stereotactic MR-guided online adaptive radiation therapy (SMART) for ultracentral thorax malignancies: results of a phase 1 trial. *Adv Radiat Oncol.* 2019;4(1):201–9.
  38. Rosenberg SA, et al. A multi-institutional experience of MR-guided liver stereotactic body radiation therapy. *Adv Radiat Oncol.* 2019;4(1):142–9.
  39. van de Schoot AJAJ, et al. Evaluation of plan quality in radiotherapy planning with an MR linac. *Phys Imaging Radiat Oncol.* 2019;10:19–24.
  40. van Timmeren JC, et al. Treatment plan quality during online adaptive re-planning. *Radiat Oncol.* 2020;15(1):203.
  41. Mannerberg A, et al. Dosimetric effects of adaptive prostate cancer radiotherapy in an MR-linac workflow. *Radiat Oncol.* 2020;15(1):168.
  42. D'Amico AV, et al. Biochemical outcome after radical prostatectomy, external beam radiation therapy, or interstitial radiation therapy for clinically localized prostate cancer. *JAMA.* 1998;280(11):969–74.
  43. Park JM, et al. A comparative planning study for lung SABR between tri-Co-60 magnetic resonance image guided radiation therapy system and volumetric modulated arc therapy. *Radiother Oncol.* 2016;120(2):279–85.
  44. McPartlin AJ, et al. MRI-guided prostate adaptive radiotherapy: a systematic review. *Radiother Oncol.* 2016;119(3):371–80.
  45. Michalski JM, et al. Radiation dose volume effects in radiation induced rectal injury. *Int J Radiat Oncol Biol Phys.* 2010;76(3 Suppl):S123–9.
  46. Shaw E, et al. Radiation Therapy Oncology Group: radiosurgery quality assurance guidelines. *Int J Radiat Oncol Biol Phys.* 1993;27(5):1231–9.
  47. Salimi M, et al. Assessment and comparison of homogeneity and conformity indexes in step-and-shoot and compensator-based intensity modulated radiation therapy (IMRT) and three-dimensional conformal radiation therapy (3D CRT) in prostate cancer. *J Med Signals Sens.* 2017;7(2):102–7.
  48. Hodapp N. Der ICRU Report 83: Verordnung, Dokumentation und Kommunikation der fluenzmodulierten Photonenstrahlentherapie (IMRT) [The ICRU Report 83: prescribing, recording and reporting photon-beam intensity-modulated radiation therapy (IMRT)]. *Strahlenther Onkol.* 2012;188(1):97–9. <https://doi.org/10.1007/s00066-011-0015-x>.
  49. Cao T, et al. Analysis of different evaluation indexes for prostate stereotactic body radiation therapy plans: conformity index, homogeneity index and gradient index. *Precis Radiat Oncol.* 2019;3(3):72–9.
  50. Stanley J, et al. Evaluation of stereotactic radiosurgery conformity indices for 170 target volumes in patients with brain metastases. *Journal of applied clinical medical physics.* 2011;12(2):3449–9.
  51. Paddick I. A simple scoring ratio to index the conformity of radiosurgical treatment plans. Technical note. *J Neurosurg.* 2000;93(Suppl 3):219–22.
  52. Otto K. Volumetric modulated arc therapy: IMRT in a single gantry arc. *Med Phys.* 2008;35(1):310–7.
  53. Maund IF, et al. Image-guided radiotherapy of the prostate using daily CBCT: the feasibility and likely benefit of implementing a margin reduction. *Br J Radiol.* 2014;87(1044):20140459.
  54. Enmark M, Korreman S, Nyström H. IGRT of prostate cancer; is the margin reduction gained from daily IG time dependent? *Acta Oncol.* 2006;45(7):907–14.
  55. Li M, et al. A comparative assessment of prostate positioning guided by three-dimensional ultrasound and cone beam CT. *Radiat Oncol.* 2015;10:82.
  56. Oates R, et al. What benefit could be derived from on-line adaptive prostate radiotherapy using rectal diameter as a predictor of motion? *J Med Phys.* 2015;40(1):18–23.
  57. Lafond C, et al. Comparison between two treatment planning systems for volumetric modulated arc therapy optimization for prostate cancer. *Phys Med.* 2014;30(1):2–9.
  58. Wiezorek T, et al. Rotational IMRT techniques compared to fixed gantry IMRT and tomotherapy: multi-institutional planning study for head-and-neck cases. *Radiat Oncol.* 2011;6(1):20.

## Publisher's Note

Springer Nature remains neutral with regard to jurisdictional claims in published maps and institutional affiliations.

Ready to submit your research? Choose BMC and benefit from:

- fast, convenient online submission
- thorough peer review by experienced researchers in your field
- rapid publication on acceptance
- support for research data, including large and complex data types
- gold Open Access which fosters wider collaboration and increased citations
- maximum visibility for your research: over 100M website views per year

At BMC, research is always in progress.

Learn more [biomedcentral.com/submissions](https://biomedcentral.com/submissions)





**6. Paper II: ExacTrac Dynamic workflow evaluation:  
Combined surface optical/thermal imaging and  
X-ray positioning**



Received: 18 November 2021 | Revised: 7 July 2022 | Accepted: 19 July 2022

DOI: 10.1002/acm2.13754

## MEDICAL IMAGING

JOURNAL OF APPLIED CLINICAL  
MEDICAL PHYSICS

# ExacTrac Dynamic workflow evaluation: Combined surface optical/thermal imaging and X-ray positioning

Vanessa Da Silva Mendes<sup>1</sup> | Michael Reiner<sup>1</sup> | Lili Huang<sup>1</sup> | Daniel Reitz<sup>1</sup> |  
Katrin Straub<sup>1</sup> | Stefanie Corradini<sup>1</sup> | Maximilian Niyazi<sup>1</sup> | Claus Belka<sup>1,2</sup> |  
Christopher Kurz<sup>1</sup> | Guillaume Landry<sup>1</sup> | Philipp Freislederer<sup>1</sup>

<sup>1</sup>Department of Radiation Oncology,  
University Hospital, LMU Munich, Munich,  
Germany

<sup>2</sup>German Cancer Consortium (DKTK),  
Partner Site Munich, Munich, Germany

### Correspondence

Vanessa Da Silva Mendes, Department of  
Radiation Oncology, University Hospital, LMU  
Munich, Marchioninistraße 15, 81377 Munich,  
Germany.

Email:

[Vanessa.Mendes@med.uni-muenchen.de](mailto:Vanessa.Mendes@med.uni-muenchen.de)

### Abstract

In modern radiotherapy (RT), especially for stereotactic radiotherapy or stereotactic radiosurgery treatments, image guidance is essential. Recently, the ExacTrac Dynamic (EXTD) system, a new combined surface-guided RT and image-guided RT (IGRT) system for patient positioning, monitoring, and tumor targeting, was introduced in clinical practice. The purpose of this study was to provide more information about the geometric accuracy of EXTD and its workflow in a clinical environment. The surface optical/thermal- and the stereoscopic X-ray imaging positioning systems of EXTD was evaluated and compared to cone-beam computed tomography (CBCT). Additionally, the congruence with the radiation isocenter was tested. A Winston Lutz test was executed several times over 1 year, and repeated end-to-end positioning tests were performed. The magnitude of the displacements between all systems, CBCT, stereoscopic X-ray, optical-surface imaging, and MV portal imaging was within the submillimeter range, suggesting that the image guidance provided by EXTD is accurate at any couch angle. Additionally, results from the evaluation of 14 patients with intracranial tumors treated with open-face masks are reported, and limited differences with a maximum of 0.02 mm between optical/thermal- and stereoscopic X-ray imaging were found. As the optical/thermal positioning system showed a comparable accuracy to other IGRT systems, and due to its constant monitoring capability, it can be an efficient tool for detecting intra-fractional motion and for real-time tracking of the surface position during RT.

### KEYWORDS

IGRT, optical surface imaging, SGRT, stereoscopic X-ray imaging, X-ray intra-fractional monitoring

## 1 | INTRODUCTION

Accurate tumor localization and patient setup are essential for precise external beam radiotherapy.<sup>1</sup> Moreover, real-time patient monitoring throughout all treatment fractions enables not only the detection of inter- and intra-fractional anatomical variations, but also immediate correction of the target position or the possibility

of replanning.<sup>2,3</sup> These aspects are critical for hypofractionated treatments.<sup>4</sup> Image-guided radiotherapy (IGRT) can make conventional radiotherapy (RT) safer by virtue of increased precision of delivery. In addition, it facilitates the application of specialized irradiation techniques with narrow safety margins, reducing the probability of adverse effects, and is therefore an essential component in modern RT.<sup>3</sup>

This is an open access article under the terms of the [Creative Commons Attribution](https://creativecommons.org/licenses/by/4.0/) License, which permits use, distribution and reproduction in any medium, provided the original work is properly cited.

© 2022 The Authors. *Journal of Applied Clinical Medical Physics* published by Wiley Periodicals, LLC on behalf of The American Association of Physicists in Medicine.

Linear accelerator (linac)-based stereotactic radiotherapy (SRT) and stereotactic radiosurgery (SRS) cone-beam computed tomography (CBCT) or stereoscopic X-ray imaging, such as with the ExacTrac system (Brainlab AG, Munich, Germany), are both commonly used for IGRT.<sup>5</sup> CBCT enables three-dimensional (3D) volumetric imaging, which provides better visualization of the internal anatomy and more information for image registration in comparison to stereoscopic X-ray imaging.<sup>5</sup> Compared to CBCT, the ExacTrac stereoscopic X-ray system provides faster imaging,<sup>5</sup> lower dose exposure,<sup>6,7</sup> and image guidance for non-coplanar treatments.<sup>5</sup> The use of surface guidance in RT has also been widely implemented for patient positioning, increasing patient setup information compared to laser-based setup.<sup>8</sup> Surface-guided RT (SGRT) may improve not only patient safety and comfort, via open-face masks,<sup>1,9–11</sup> but also the reproducibility of inter-fractional patient positioning and treatment interruption if the patient moves.<sup>12</sup> SGRT is also used for intra-fraction motion monitoring and respiratory gating techniques.<sup>11,13</sup> In addition, Manger et al. stated that SGRT for linac-based radiosurgery could be a surrogate for the position of intracranial lesions.<sup>1</sup> SGRT and IGRT can provide complementary imaging information during patient positioning and throughout treatment, which may improve target localization.<sup>4,13</sup>

The ExacTrac Dynamic (EXTD) system, version 1.0 (Brainlab AG, Munich, Germany), installed in our institution in June 2020, is a combined SGRT and IGRT system used for patient positioning, monitoring and tumor targeting. The system is able to provide intra-fractional positioning information of the bony anatomy via oblique stereoscopic X-ray imaging of the patient in parallel to real-time 3D surface imaging, including thermal information, for continuous motion detection during treatment delivery.<sup>13</sup> In contrast to other systems, only one optical camera is used but thermal information creates an additional dimension, which is assumed to improve tracking accuracy.<sup>14</sup>

In RT, especially for SRT or SRS treatments, the congruence between the radiation isocenter and imaging isocenters needs to be verified, for coplanar and noncoplanar treatments.<sup>15–17</sup>

Several studies investigating the accuracy of positional correction systems have been conducted over the past years.<sup>4,11,12,15,16,18–22</sup> Koubuchi et al. performed a study where the accuracy of the positional correction after treatment couch rotation was investigated and an accuracy of 0.5 mm was found for the ExacTrac X-ray system, version 5.5.2.<sup>22</sup> Another study comparing the isocenter localization accuracy of the ExacTrac X-ray and the on-board CBCT (Varian Medical Systems, Palo Alto, CA) systems was performed, demonstrating that the isocenter agreement was in the range of 1 mm.<sup>4</sup> Ma et al. analyzed and compared the accuracy achieved by SGRT and CBCT in breast cancer RT for inter-fractional

patient positioning measurements and concluded that the two systems showed good agreement, suggesting that SGRT could be used as an effective measure to increase patient positioning precision during breast cancer RT treatment, complementary to CBCT.<sup>12,23–25</sup> Moreover, Swinnen et al. demonstrated that submillimeter accuracy might be achieved by a linac equipped with an optical surface tracking system for a noncoplanar single isocenter SRS treatment for multiple brain metastases.<sup>15</sup> Chow et al. investigated the performance of the EXTD system compared to CBCT with a phantom study.<sup>26</sup>

Our study aimed to provide additional information about the geometric accuracy of EXTD and its workflow in a clinical environment. The investigation of the performance of the EXTD system and its IGRT components, such as the spatial drift of the optical/thermal system was investigated. Both optical/thermal- and the stereoscopic X-ray imaging systems were subjected to several tests and the comparison to CBCT was also performed. Moreover, as the system is mainly used in SRT and SRS treatments, further measurements recommended in the literature, like a hidden target Winston–Lutz (WL) and an end-to-end IGRT test, were included.<sup>27,28</sup> Additionally, intra-fractional X-ray and combined optical/thermal motion data from a study with 14 patients with intracranial tumors, treated at our institution with open-face masks, was evaluated.

## 2 | METHODS

### 2.1 | EXTD system

The EXTD was used in all experiments. It combines the following in-room SGRT and IGRT strategies:

- Optical structured light scanning (SLS)
- Thermal imaging
- Oblique stereoscopic kilovoltage (kV) X-ray imaging

The system consists of an optical/thermal imaging device, which contains a blue light projector, two stereoscopic high-resolution cameras, and an integrated thermal camera.<sup>14</sup> The optical/thermal imaging device is positioned centrally above the treatment couch. Moreover, two kV X-ray tubes are mounted in the bunker floor, projecting obliquely onto two ceiling mounted flat panel detectors, with a 300 × 300-mm<sup>2</sup> radiation sensitive area.<sup>29,30</sup> The geometrical radiation field size at the isocenter is 180 × 180 mm<sup>2</sup>.<sup>30</sup>

The structured light projector emits a pattern onto the patient surface detected by the two optical cameras. The camera images of this pattern are used to calculate a 3D map of the patient surface. Moreover, a 2D thermal matrix is created from the patient's heat signal taken by the integrated thermal camera. These two matrices



are matched in order to calculate a hybrid 3D+thermal matrix containing spatial and thermal information of each point of the patient surface.<sup>14</sup>

The internal anatomy can be verified through paired stereoscopic kV X-rays. These images are then compared to the digitally reconstructed radiographs (DRRs), which are calculated from the planning computed tomography (CT) scan and the isocenter position, yielding a rigid body transformation.<sup>31</sup>

All measurements were performed in a clinical environment. The EXTD system was installed at an Elekta Versa HD linac equipped with the HexaPOD evo RT System (Elekta AB, Stockholm, Sweden) controlling the treatment couch movement within 6 degrees of freedom (DoF) with an accuracy of  $\pm 0.2$  mm.<sup>32</sup> The linac was equipped with an Agility multileaf collimator consisting of 160 leaves with a leaf width of 5 mm at the isocenter.

## 2.2 | EXTD clinical workflow

### 2.2.1 | EXTD monitoring preparation

Once the planning CT and the treatment plan are imported into EXTD, the monitoring strategy needs to be prepared before treatment. This implies the selection of the treatment indication template, the review of some ExacTrac settings, like the surface tracking and X-ray displacement tolerances, auto X-ray triggers, the restriction of the CT volume to improve X-ray to DRR fusion, the adjustment of the patient skin tone setting (light, fair, medium or dark), among others.<sup>30</sup>

### 2.2.2 | Patient positioning

Pre-positioning is first used to approximately position the patient before the treatment, by matching the live 3D optical surface, without thermal information, to the reference contour extracted from the treatment planning CT. A 3-DoF translation shift is sent to the treatment table, and the patient is moved.

After the patient is roughly positioned, an area of interest (AOI), as a surrogate of the movement of the planning target volume, needs to be selected. The AOI's purpose is to track the patient's movement using surface tracking, while providing thermal information. Optical and thermal surface information are used during the monitoring mode, where the AOI is treated as a single rigid area.<sup>30</sup> The quality of the monitoring depends not only on the size of the AOI but also on the topology of the surface.<sup>30</sup> Moreover, for a reliable tracking of the patient movement, the AOI should not include parts of the linac or any external systems.<sup>30</sup>

For final positioning, a pair of X-ray images is acquired and registered to the DRRs. A 6-DoF X-ray-based correction shift of the patient is sent to the robotic couch

Elekta HexaPOD evo RT System. Another pair of X-ray images is taken to confirm the patient's position, and the process is iterated until the remaining deviation from the actual position, and the reference position is within the specified tolerances, at which point the patient is considered to be positioned with sufficient accuracy.<sup>31</sup> After the last pair of X-ray images is acquired and the patient is correctly positioned, the optical surface reference information is updated.<sup>14</sup>

### 2.2.3 | Patient monitoring

The patient monitoring mode is used to track intra-fractional patient motion. The 3D live optical surface information is projected over the thermal image plane and 3D surface points and 2D thermal data are correlated, using the Perspective-n-Point algorithm.<sup>14</sup> The 3D optical/thermal information is constantly compared to the reference image, X-ray images are triggered according to predefined settings and if the surface tracking exceeds the predefined tolerances. Every time stereoscopic X-ray images are acquired, and if patient positioning is within the tolerance, a new optical/thermal imaging reference is established.<sup>30</sup>

## 2.3 | Description of the experiments

For the EXTD system, when preparing the monitoring strategy, the skin tone was adjusted for every phantom individually. For both cranial and pelvic verification phantoms, Figure 1a,c, respectively, the chosen skin tone was "dark," whereas for the 3D-printed head phantom and the abdominothoracic phantom, Figure 1d,f, respectively, the skin tone was adjusted to "light." All experiments were performed in a treatment room, with air temperature at  $\sim 21^\circ\text{C}$ .

### 2.3.1 | EXTD and CBCT: positioning consistency

The differences between EXTD and CBCT image registrations, and therefore the corresponding positioning consistency of both systems, were measured using two anthropomorphic phantoms of two different anatomical regions: a cranial verification phantom (Brainlab AG, Munich, Germany) and a pelvic verification phantom (Brainlab AG, Munich, Germany) (Figure 1a–c). The phantoms were scanned with a CT scanner (Toshiba Aquilion LB, Canon Medical Systems, Japan), with a slice thickness of 3 mm for the pelvic phantom ( $0.7 \times 0.7 \times 3$  mm<sup>3</sup>), and 1 mm for the head phantom ( $0.9 \times 0.9 \times 1$  mm<sup>3</sup>) according to the recommendations for linac SRS/SBRT quality assurance programs.<sup>33–36</sup> For each phantom, six arbitrary isocenters were defined

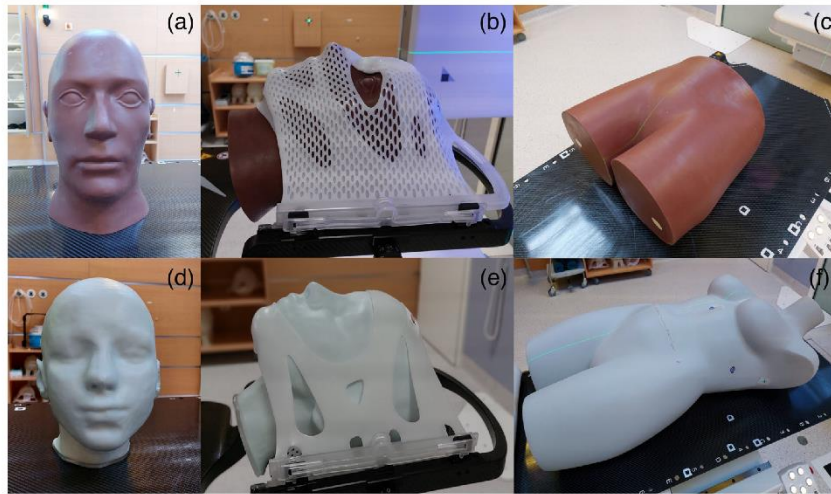


**FIGURE 1** Anthropomorphic phantoms: (a) cranial verification phantom, (b) cranial phantom immobilized on the treatment couch with a cranial 4Pi stereotactic mask, (c) pelvic verification phantom, (d) 3D-printed head phantom with bone equivalent material, (e) head phantom immobilized on the treatment couch with a cranial 4Pi open face mask, and (f) abdominothoracic phantom with bone-equivalent material and a distinct heat signature

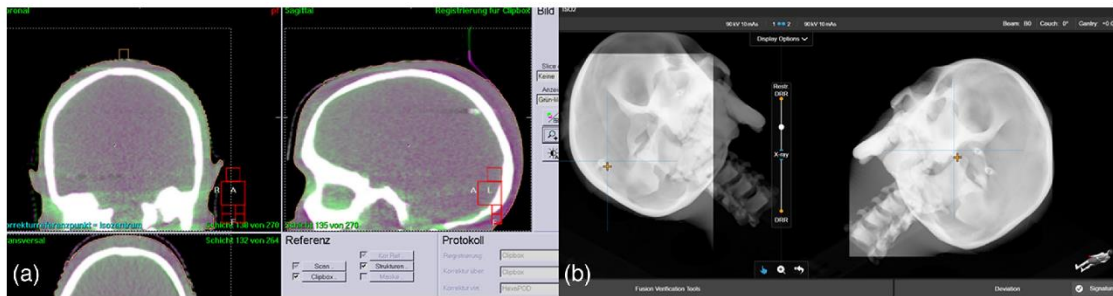


**FIGURE 2** Registration of actual positioning image with planned positioning image, of the cranial verification phantom, by both systems: (a) cone-beam computed tomography (CBCT) and (b) stereoscopic X-ray imaging

manually and the CT datasets were transferred to both EXT D and the CBCT system XVI version 5.0.4 (Elekta AB, Stockholm, Sweden).

#### Setup procedure and positioning consistency

Before starting the measurements, the radiation isocenter and the imaging isocenters of the EXT D and CBCT systems were aligned to the same reference point, using the cranial phantom with an inserted ball bearing (BB), which was fixed to the treatment couch with a cranial 4Pi stereotactic immobilization system (Brainlab AG, Munich, Germany) (Figure 1b).

To compare the positioning accuracy of EXT D and CBCT imaging, both the cranial phantom along with the cranial stereotactic mask and the pelvic phantom were used. The phantoms were pre-positioned using EXT D surface data. Afterward, EXT D stereoscopic X-ray images and a CBCT scan were acquired and the

calculated correction shifts in 6 DoF of both systems were compared. Finally, the shifts calculated by the EXT D system were applied by moving the treatment couch with the HexaPOD evo RT system. Another pair of stereoscopic X-ray images and a second CBCT scan were acquired to determine the residual shift after positioning correction. In Figure 2a,b, the fusion of current and planned positioning images by both systems, CBCT and EXT D X-ray imaging, is shown.

These two positioning methods resulted in correction shifts which were compared according to the following equation:

$$\Delta d_{\text{CBCT-Xray}} = d_{\text{CBCT}} - d_{\text{Xray}} \quad (1)$$

for the lateral ( $\Delta d_{\text{CBCT-Xray},X}$ ), longitudinal ( $\Delta d_{\text{CBCT-Xray},Y}$ ), and vertical ( $\Delta d_{\text{CBCT-Xray},Z}$ ) translational directions and pitch ( $\Delta d_{\text{CBCT-Xray,PITCH}}$ ), roll ( $\Delta d_{\text{CBCT-Xray,ROLL}}$ ), and yaw

**TABLE 1** Cone-beam computed tomography (CBCT) and ExacTrac Dynamic (EXTD) X-ray exposure parameters

		Head phantom	Pelvic phantom
<b>CBCT</b>	Tube voltage (kV)	100	120
	Total mAs	18.3	264
	Gantry angle rotation span	200°	360°
	kV Collimator/kV filter axial FOV	S20/F0 27 cm (small)	M20/F1 41 cm (medium)
<b>ExacTrac Dynamic</b>	Tube voltage (kV)	90	120
	mAs	10	20

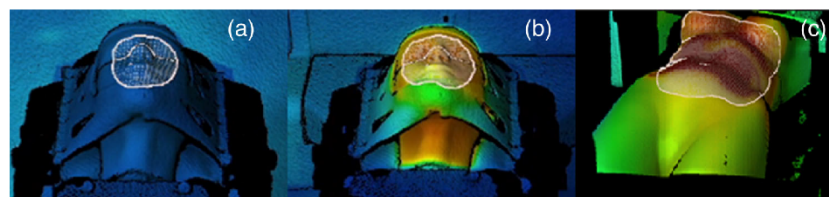


**FIGURE 3** 3D surface image of phantoms at different temperatures, projected over a thermal image plane: (a) head phantom with a cold surface, (b) head phantom with a warm surface, and (c) abdominothoracic phantom with a warm surface

( $\Delta d_{\text{CBCT-Xray,YAW}}$ ) rotational DoF, according to the patient coordinate system.

To investigate the stability and reproducibility of the measurements, this experiment was conducted for each of the six isocenters in two separate time points within ~10 months difference. The second measurement consisted in repeating the procedure five times.

Imaging settings for CBCT and EXT D used for the measurements are indicated in Table 1. Rigid registration and automatic fusion, based on bony features, were performed by the proprietary matching algorithms of both software systems.

### 2.3.2 | EXT D: optical/thermal-, stereoscopic X-ray imaging, and radiation isocenter

Two dedicated anthropomorphic phantoms with a distinct thermal signature were used for this part of the study (Figure 1d–f):

- A head phantom, 3D-printed from bone-equivalent materials with three spherical 5-mm-diameter-embedded BBs (RTsafe, Greece; Figure 3a,b, respectively), was filled with water. The phantom was immobilized to the couch using a cranial 4Pi open-face mask (Brainlab AG, Germany) and scanned with a CT scanner with a slice thickness of 0.5 mm.<sup>33–36</sup> The central BB was chosen as the isocenter (BB0) and delineated on the planning CT dataset ( $0.6 \times 0.6 \times 0.5 \text{ mm}^3$ ) using the clinical

treatment planning system Oncentra MasterPlan Version 4.5 (Elekta AB, Stockholm, Sweden).

- An abdominothoracic phantom with bone-equivalent materials and a distinct and constant heat signature (Brainlab AG, Germany) was scanned with a CT scanner, with a slice thickness of 3 mm ( $1 \times 1 \times 3 \text{ mm}^3$ ). It was positioned on the treatment couch and no immobilization device was used. One isocenter was chosen, located in the spinal column in the thoracic region.

The CT images of the phantoms and corresponding treatment plans were transferred to EXT D and were used as reference images for the image registration.

#### Spatial drift

Following the recommendations of TG-147 as well as the TG-302 reports,<sup>27,37</sup> measurements to assess the spatial drift of the optical/thermal system were conducted. They were performed with the abdominothoracic phantom (Figure 1f) with cold and warm surfaces (Figure 3c) in the abdominal region. The 3D camera has two systems subject to a warm-up phase: the system power and the blue light projector. The system power was on for an extended time (>1 h). However, in order to simulate a clinical situation, that is, when this system is not necessarily used every consecutive patient, the blue light projector was switched off for 30 min. The phantom was placed on the treatment couch at 0° and positioned using the EXT D system. The stability of the system was then evaluated by continuing to sample manually



the phantom's position in the lateral, longitudinal, and vertical directions, every 0.5 min for 70 min.

#### Influence of the surface temperature

**Cold and warm surface: stability of the optical/thermal imaging positioning values during the delivery of a volumetric modulated arc therapy (VMAT) plan.** The head phantom was filled with water at room temperature (labeled "cold surface") or with warm water ( $\approx 41^\circ\text{C}$ ) (labeled "warm surface," surface temperature within  $36\text{--}32^\circ\text{C}$  over the course of the measurements) (Figure 3a,b) and was immobilized on the treatment couch at  $0^\circ$  and positioned using the EXTEND system. In the monitoring mode, the optical/thermal imaging positioning values were monitored in all translational and rotational dimensions and recorded in a log file during the delivery of a VMAT plan, taking  $\sim 12$  min. For the cold and the warm surface, the resulting positioning values,  $d_{\text{ST},X}$ ,  $d_{\text{ST},Y}$ ,  $d_{\text{ST},Z}$ ,  $d_{\text{ST},\text{PITCH}}$ ,  $d_{\text{ST},\text{ROLL}}$ , and  $d_{\text{ST},\text{YAW}}$ , in the lateral, longitudinal, vertical directions, as well as for pitch, roll and yaw, respectively, were compared and reported. The Mann–Whitney  $U$  test was used to investigate differences between a cold and a warm surface.

**Cold and warm surface: couch/phantom displacements, optical/thermal- and stereoscopic X-ray imaging.** Further measurements with the head phantom (cold and warm surface) (Figure 3a,b), positioned on the treatment couch at  $0^\circ$ , were conducted. Twenty five couch displacements were performed in two distinct time points 9 months apart and repeated four times in order to investigate the stability and reproducibility of the measurements. The couch displacements were performed in all three directions, lateral, longitudinal, and vertical in the range of 0–3 mm, and the optical/thermal- and the stereoscopic X-ray imaging positioning values were compared.

A similar procedure with the head phantom and non-coplanar couch angles ( $90^\circ$ ,  $45^\circ$ ,  $315^\circ$ , and  $270^\circ$ ) was carried out. The phantom's surface was warm to simulate the body temperature. Twenty couch displacements were performed in all three translational directions, in the range of 0–3 mm.

The comparison between the optical/thermal and X-ray imaging positioning systems was performed for the lateral, longitudinal, and vertical directions, relative to the patient coordinate system, according to the following equation:

$$\Delta d_{\text{HEAD}} = d_{\text{Xray}} - d_{\text{ST}} \quad (2)$$

The Mann–Whitney  $U$  test was used to investigate differences between a cold and a warm surface, at couch  $0^\circ$ . Additionally, for a warm surface, the deviation of the positioning values for both imaging methods was also analyzed for a treatment couch at  $0^\circ$  when compared to other couch angles.

For the abdomin thoracic phantom, similar measurements were executed. The following seven couch angles were chosen:  $90^\circ$ ,  $60^\circ$ ,  $30^\circ$ ,  $0^\circ$ ,  $330^\circ$ ,  $300^\circ$ , and  $270^\circ$  and to simulate an RT treatment in the torso region, where no immobilization system is usually used, 45 random phantom displacements were performed. The optical/thermal- and the stereoscopic X-ray imaging positioning values were compared for both a cold and a warm surface, according to the following equation:

$$\Delta d_{\text{ABDOMINOTHOR}} = d_{\text{Xray}} - d_{\text{ST}} \quad (3)$$

where  $\Delta d_{\text{ABDOMINOTHOR},X}$ ,  $\Delta d_{\text{ABDOMINOTHOR},Y}$ , and  $\Delta d_{\text{ABDOMINOTHOR},Z}$  represent the lateral, longitudinal, and vertical directions, respectively.

#### Warm surface: optical/thermal-, stereoscopic X-ray imaging positioning and radiation isocenter

To investigate and compare the accuracy of the optical/thermal- and stereoscopic X-ray imaging positioning (IGRT-derived isocenter) and their correlation with the radiation isocenter position, the setup errors using MV portal images, optical/thermal- and X-ray imaging positioning were investigated. The head phantom was filled with warm water ( $\approx 41^\circ\text{C}$ ) and positioned using the EXTEND system. The isocenter of the plan was located at the center of BB0, and reference setup square fields  $2 \times 2 \text{ cm}^2$  (25 MU) centered in the BB0 were created.

With the treatment couch at  $0^\circ$ , five couch displacements with a maximal amplitude of 2 mm in all three translational directions were applied. After each couch displacement, a WL test was performed, with the gantry at cardinal angles ( $0^\circ$ ,  $90^\circ$ ,  $180^\circ$ , and  $270^\circ$ ), used as an indicator of the positional correction accuracy. To provide a more representative sample of all possible couch angles for our SRT or SRS treatments, this test was also performed at noncoplanar couch angles ( $90^\circ$ ,  $45^\circ$ ,  $315^\circ$ , and  $270^\circ$ ) and gantry at  $0^\circ$ . For each couch angle, four couch displacements with a maximal amplitude of 2 mm in the lateral and longitudinal directions,  $s_X$  and  $s_Y$ , respectively, were performed. Both reference position and the couch displacements were analyzed using the Winston–Lutz module of Pylinac, version 2.5<sup>38,39</sup> for processing the WL-type EPID images. The optical/thermal- and the stereoscopic X-ray imaging positioning values were both compared to the MV portal image setup errors, according to the following equations:

$$\Delta d_{\text{MV-IGRT,ST}} = d_{\text{MV}} - d_{\text{ST}} \quad (4)$$

$$\Delta d_{\text{MV-IGRT,Xray}} = d_{\text{MV}} - d_{\text{Xray}} \quad (5)$$

where  $\Delta d_{\text{MV-IGRT,ST},X}$ ,  $\Delta d_{\text{MV-IGRT,ST},Y}$ , and  $\Delta d_{\text{MV-IGRT,ST},Z}$  represent the discrepancies between MV portal imaging and optical/thermal positioning values in the lateral, longitudinal, and vertical directions, respectively.

$\Delta d_{MV-IGRT,Xray,X}$ ,  $\Delta d_{MV-IGRT,Xray,Y}$ , and  $\Delta d_{MV-IGRT,Xray,Z}$  represent the discrepancies between MV portal imaging and X-ray imaging positioning values in the lateral, longitudinal, and vertical directions, respectively.

#### Hidden target test

The hidden target test resembles the traditional workflow of IGRT-based treatments and is performed to assess the coincidence of both imaging and radiation isocenters. This procedure is executed regularly at our institution, using the anthropomorphic cranial verification phantom, immobilized on the treatment couch with a cranial stereotactic mask (Figure 1a,b), and positioned with EXT-D. This phantom has a radiopaque spherical 5-mm-diameter-embedded BB, which was chosen as the isocenter, and it was scanned with a slice thickness of 1 mm ( $0.6 \times 0.6 \times 1 \text{ mm}^3$ ) according to the recommendations for linac SRS/SBRT quality assurance programs. A treatment plan with square fields of  $2 \times 2 \text{ cm}^2$  centered in the isocenter with gantry at  $0^\circ$ ,  $90^\circ$ ,  $180^\circ$ , and  $270^\circ$  was used. The results of 40 WL tests (performed between March 2021 and March 2022), for which the recommended accuracy is 1 mm for SRS treatments<sup>27,28,37</sup> were included in this study.  $\Delta d_{WL,X}$ ,  $\Delta d_{WL,Y}$ , and  $\Delta d_{WL,Z}$  represent the residual differences between IGRT-aligned isocenter and the radiation field isocenter, in the lateral, longitudinal, and vertical directions, respectively.

#### End-to-end IGRT test

Following the recommendations of the TG-147 and TG-302 reports,<sup>27,37</sup> an end-to-end IGRT test, which aims to assess the entire clinical IGRT process, was also performed. After making a new stereotactic mask, the acquisition of a new CT scan, and the creation of a new treatment plan, the same procedure as the hidden target test was followed. The WL test was executed 12 times (repeated exposures while moving the phantom between exposures).

#### 2.3.3 | Patient data

A total of 14 patients with intracranial tumors treated at our institution during the first 3 months of 2021 underwent normofractionated cranial RT treatments. Patients were immobilized to the couch using a cranial open-face mask (Brainlab AG, Germany and IT-V, Innsbruck, Austria), positioned and monitored with EXT-D, and 142 fractions were analyzed. To detect intra-fractional motion and quantify the deviation between planned and current position during the treatment, optical/thermal surface information from the area within the face opening was collected and recorded in a log file. Simultaneously, patients were monitored by stereoscopic X-ray imaging,

acquired at gantry positions  $0^\circ$ ,  $90^\circ$ ,  $180^\circ$ , and  $270^\circ$ , providing anatomical information about the position of bony structures.

In Figure S1, an exemplary patient monitoring with EXT-D is shown, with stereoscopic X-ray and optical/thermal imaging information, as well as a graphical representation of the intra-fractional motion during the treatment.

The 806 optical/thermal- and stereoscopic X-ray imaging positioning values were recorded. The differences between positioning values provided by both systems were evaluated and compared, according to the following equation:

$$\Delta d_{PAT} = d_{Xray} - d_{ST} \quad (6)$$

where  $\Delta d_{PAT,X}$ ,  $\Delta d_{PAT,Y}$ ,  $\Delta d_{PAT,Z}$ ,  $\Delta d_{PAT,PITCH}$ ,  $\Delta d_{PAT,ROLL}$ , and  $\Delta d_{PAT,YAW}$  represent the differences in the positioning values in the lateral, longitudinal, and vertical directions, as well as for pitch, roll and yaw, respectively.

## 2.4 | Statistical analysis

The IBM SPSS Statistics Version 26.0 software (IBM Corporation, Armonk, New York) was used to perform Mann–Whitney  $U$  tests to investigate differences of the positioning values for optical/thermal imaging between a cold and a warm surface, as well as to analyze the difference between both imaging methods, optical/thermal- and stereoscopic X-ray imaging. Differences were considered statistically significant for  $p$  value  $\leq 0.05$ .

## 3 | RESULTS

### 3.1 | EXT-D and CBCT: positioning consistency

The positional differences between EXT-D stereoscopic X-ray imaging and CBCT for the cranial and the pelvic phantoms, as calculated with Equation (1), are shown in Table 2. For the cranial phantom, the largest translational deviation observed was in the lateral direction, showing a median difference of 0.4 mm. For the pelvic phantom, the largest translational deviation was also observed in the lateral direction, with a median of 0.3 mm. Nevertheless, all differences were within the submillimeter range. Regarding the rotational DoF, deviations were also similar and the largest median difference was  $0.4^\circ$ .

Repetition of the measurements (five times) after 10 months yielded similar results (Table S1).

**TABLE 2** The difference between the stereoscopic X-ray and cone-beam computed tomography (CBCT) positional shifts measured using two anthropomorphic phantoms, each phantom with six different isocenter locations (median and IQR)

Stereoscopic X-ray imaging vs. CBCT		$\Delta d_{\text{CBCT-Xray},X}$ (mm)	$\Delta d_{\text{CBCT-Xray},Y}$ (mm)	$\Delta d_{\text{CBCT-Xray},Z}$ (mm)	$\Delta d_{\text{CBCT-Xray},\text{PITCH}}$ (°)	$\Delta d_{\text{CBCT-Xray},\text{ROLL}}$ (°)	$\Delta d_{\text{CBCT-Xray},\text{YAW}}$ (°)
Cranial verification phantom	Initial correction	0.4 [0.1; 0.9]	−0.1 [−0.2; 0.1]	0 [−0.3; 0.4]	0.4 [0; 1.1]	−0.1 [−0.6; −0.1]	−0.3 [−0.4; −0.2]
	After correction	0.4 [0.3; 0.4]	0 [−0.1; 0.1]	−0.2 [−0.4; 0.1]	0 [−0.1; 0.1]	0 [−0.1; 0.1]	0 [0; 0.1]
Pelvic verification phantom	Initial correction	0.3 [0.2; 0.4]	−0.1 [−0.6; 0.1]	0.1 [−0.3; 0.6]	0.1 [0.1; 0.3]	0.2 [0.1; 0.5]	−0.2 [−0.2; −0.1]
	After correction	0.2 [0.1; 0.3]	0.1 [−0.2; 0.5]	0.1 [−0.2; 0.3]	0.1 [0; 0.1]	−0.1 [−0.3; 0.2]	0 [−0.1; 0]

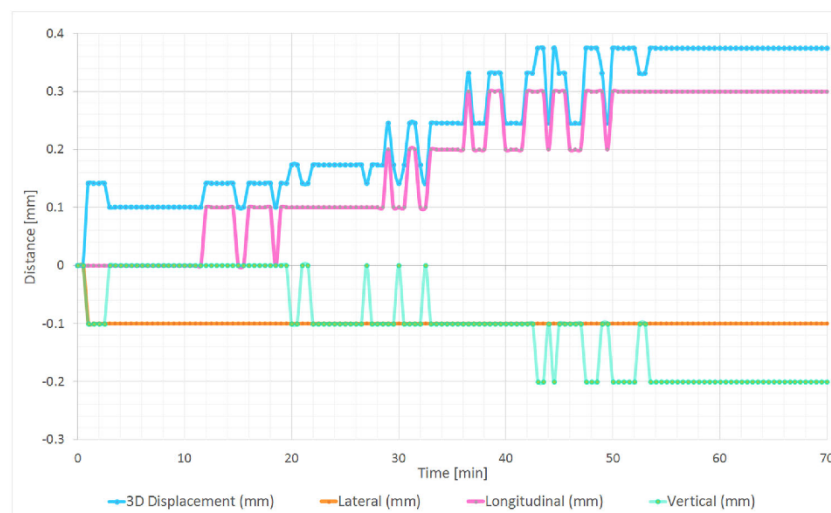


**FIGURE 4** Surface-derived position deviations recorded from the initial position in the lateral, longitudinal, and vertical directions, as well as the 3D displacement vector of the total deviation, for the abdominal phantom with a warm surface

### 3.2 | EXT-D: optical/thermal- and stereoscopic X-ray imaging and MV beam

#### 3.2.1 | Spatial drift

Measurements using the abdominothoracic phantom with a warm surface showed drifts up to 0.4 mm. In Figure 4, the deviations in all three translational directions are plotted, as well as the vector length of the deviation, where the maximal deviation is observed in the longitudinal direction, 0.3 mm. The rotational drifts did not exceed 0.1° in all three directions.

For a cold surface, the drifts reached 0.8 mm. The largest deviations were also seen in the longitudinal direction, 0.7 mm, and the rotational drifts were below

0.3° in all three directions. The deviations in all three translational directions are plotted in Figure S2.

#### 3.2.2 | Influence of the surface temperature

*Cold and warm surface: stability of the optical/thermal imaging positioning values during the delivery of a VMAT plan*

The variance of the optical/thermal imaging positioning values ( $d_{\text{ST}}$ ) for a cold and a warm surface, during the delivery of a VMAT plan (~12 min), was analyzed (Table S2). The recorded values for both temperatures were very similar, and the difference was always <0.07 mm

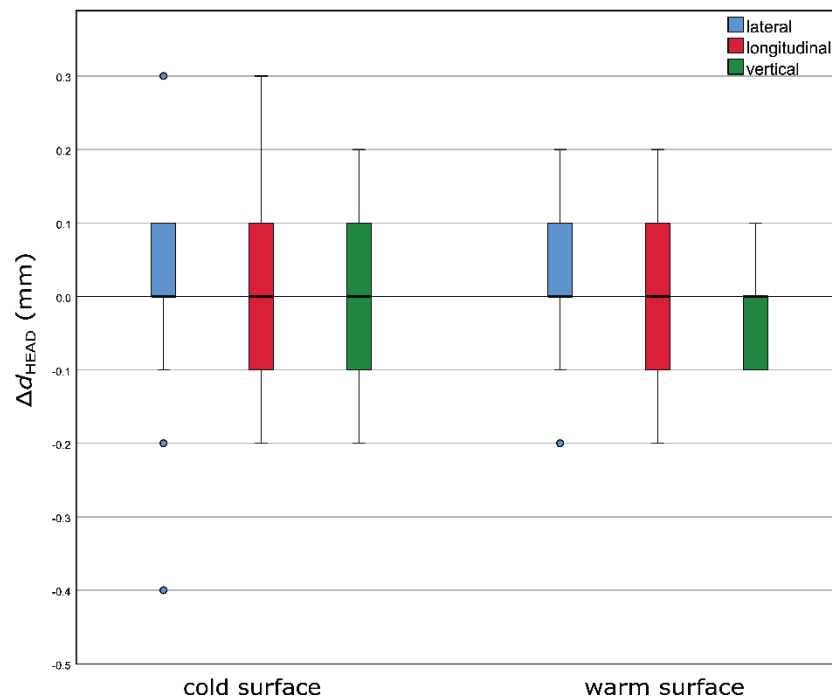


**FIGURE 5** Boxplots of the distribution of the differences between optical/thermal- and X-ray imaging positioning values (25 displacements at couch 0°) for a cold and a warm surface of the head phantom. The results for the different directions, lateral, longitudinal, and vertical, are plotted in blue, red, and green, respectively. The boxplots indicate the spread of the central 50% of the data, denominated as IQR. The median, the 25th ( $Q_1$ ) and the 75th ( $Q_3$ ) percentiles are also shown. The upper and the lower whiskers represent data outside the IQR but inside the range defined by  $1.5 \times \text{IQR}$ . Outliers are defined as values outside the whiskers' range.

and  $<0.05^\circ$ . A Mann–Whitney  $U$  test was performed to investigate whether the differences reported by the surface optical/thermal imaging positioning system for a cold and a warm surface were statistically significant. The test showed that there was no significant difference in  $d_{\text{STY}}$  and  $d_{\text{STROLL}}$  when comparing a cold and a warm surface ( $p > 0.05$ ), as opposed to the other DoF, which presented  $p \leq 1 \times 10^{-5}$ . However, the median of the deviations observed was always below 0.08 mm and  $0.05^\circ$ . The optical/thermal imaging positioning values recorded in the log file present 0.01-mm precision.

#### Cold and warm surface: couch/phantom displacements, optical/thermal- and stereoscopic X-ray imaging

For the head phantom with a cold and a warm surface, treatment couch at  $0^\circ$ , boxplots of the distribution of the differences between optical/thermal- and X-ray imaging positioning values for 25 couch displacements are presented in Figure 5. For a warm surface, the differences between both imaging positioning modalities were slightly less scattered than the ones for a cold surface. However, no median differences in any direction were observed. The maximum deviation observed for a cold

surface was 0.4 mm in the lateral direction, whereas for a warm surface the maximal deviation was 0.2 mm, in both lateral and longitudinal directions. In addition, the Mann–Whitney  $U$  test showed no significant difference between a cold and a warm surface regarding the distribution of the differences between optical/thermal- and X-ray imaging positioning values ( $p > 0.05$ ).

The same 25 couch displacements were performed 9 months later (four repetitions) and similar results were found (Figure S3).

Moreover, similar measurements (20 couch displacements) were performed with the head phantom for the noncoplanar couch angles  $90^\circ$ ,  $45^\circ$ ,  $315^\circ$ , and  $270^\circ$ , in the lateral, longitudinal, and vertical directions. Boxplots of the distribution of the differences between optical/thermal- and X-ray imaging positioning values for the head phantom (Equation 2) are presented in Figure S4. The largest deviations were observed for couch angles  $45^\circ$  and  $315^\circ$ , and the maximal deviation recorded was 0.4 mm in the lateral direction. The median differences were 0 mm for all couch angles, except for couch  $90^\circ$ , in the lateral direction, where this value reached 0.1 mm. The smallest deviations were observed for couch angles  $0^\circ$  and  $270^\circ$ , in all three directions,

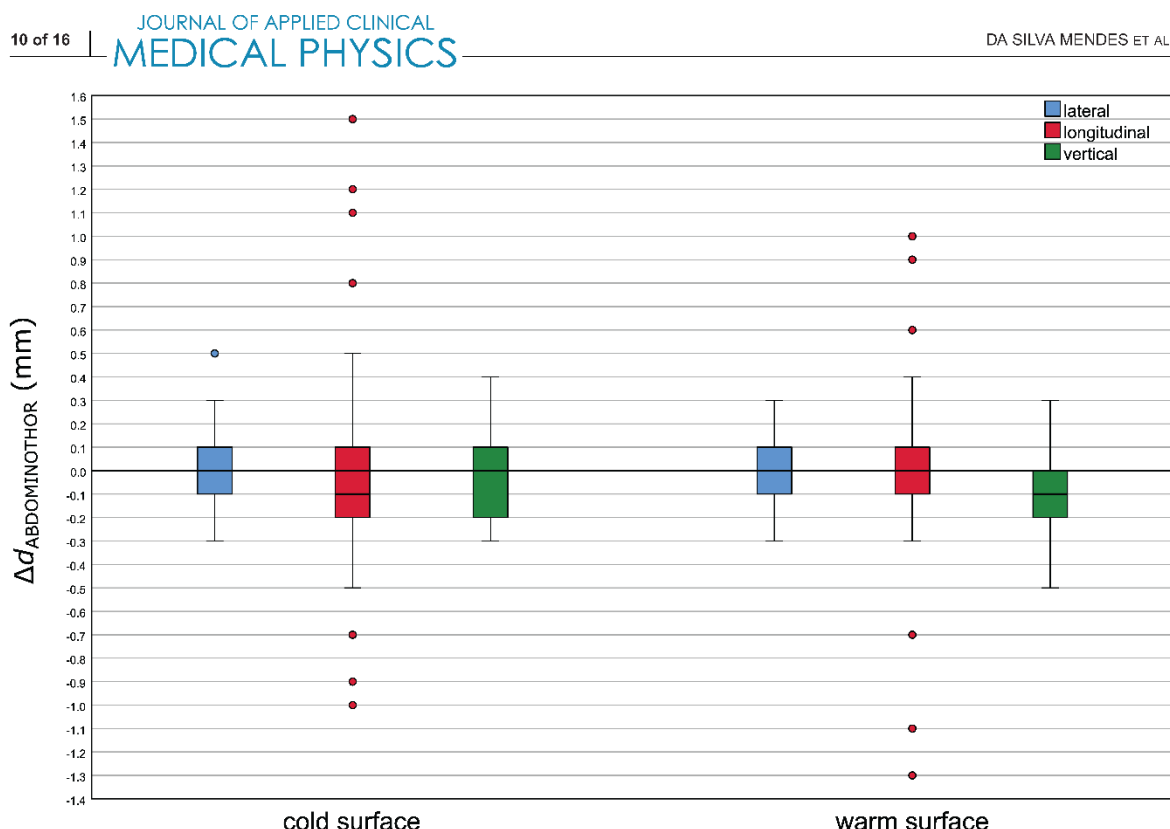


**FIGURE 6** Boxplots of the distribution of the differences between optical/thermal- and X-ray imaging positioning values (45 measurements at 7 couch angles) for a cold and a warm surface of the abdominothoracic phantom. The results for the different directions, lateral, longitudinal, and vertical are plotted in blue, red, and green, respectively. The boxplots indicate the spread of the central 50% of the data, denominated as IQR. The median, the 25th, and the 75th percentiles are also shown. The upper and the lower whiskers represent data outside the IQR but inside the range defined by  $1.5 \times \text{IQR}$ . Outliers are defined as values outside the whiskers' range.

with a maximal deviation of 0.2 mm. The result of the Mann–Whitney  $U$  test between the couch at  $0^\circ$  and the other four noncoplanar couch angles were statistically nonsignificant,  $p > 0.05$ .

For the abdominothoracic phantom, to simulate an RT treatment in the torso region, where no immobilization system is usually used, 45 random phantom displacements, with displacements between 4.6 and 65.6 mm, were performed for seven different couch angles. The deviations observed between the optical/thermal- and the stereoscopic X-ray imaging positioning values, with a cold and a warm surface, are shown in Figure 6. The median differences, for both cold and warm surface, were very similar and below 0.2 mm. The largest deviations were observed in the longitudinal direction, with a maximal deviation of 1.5 mm for a cold surface and 1.3 mm for a warm surface. The Mann–Whitney  $U$  test showed no significant difference between both temperature surfaces regarding the distribution of the differences between optical/thermal- and X-ray imaging positioning values ( $p > 0.05$ ).

### 3.2.3 | Warm surface: optical/thermal-, stereoscopic X-ray imaging positioning and radiation isocenter

#### Couch $0^\circ$

The deviations between the positioning values, reported by optical/thermal- and stereoscopic X-ray imaging, respectively, and the displacement of the BB0 center from the MV beam center (Equations 4 and 5), after five couch displacements in all three directions of a maximal amplitude of 2 mm, are shown in Table 3. The median differences for both imaging positioning modalities in comparison to MV portal imaging positioning were not larger than 0.3 mm. The deviations between optical/thermal- and MV portal imaging differ by at maximum 0.1 mm from the corresponding deviation between stereoscopic X-ray- and MV portal imaging. Figure 7 shows the different methods of monitoring the head phantom's position, with stereoscopic X-ray imaging and optical/thermal imaging.



**TABLE 3** The difference (median and IQR) between the positioning values, reported by optical/thermal- and stereoscopic X-ray imaging, respectively, and the distance between the MV radiation center and the BB's center, in a  $2 \times 2\text{-cm}^2$  field (25 MU, 6-MV photons), for five couch translations in all three directions

Gantry angle	Surface/Thermal imaging vs. MV portal image (mm)				Stereoscopic X-ray imaging vs. MV portal image (mm)			
	$\Delta d_{MV-IGRT,ST,X}$	$\Delta d_{MV-IGRT,ST,Y}$	$\Delta d_{MV-IGRT,ST,Z}$	3D displacement	$\Delta d_{MV-IGRT,Xray,X}$	$\Delta d_{MV-IGRT,Xray,Y}$	$\Delta d_{MV-IGRT,Xray,Z}$	3D displacement
0°	0.2 [0.1; 0.2]	-0.1 [-0.2; -0.1]	—	0.1 [0; 0.1]	0.1 [0; 0.3]	-0.1 [-0.1; 0]	—	0.2 [0.1; 0.2]
90°	—	0 [-0.1; 0]	0.2 [0.2; 0.2]	0.2 [0.2; 0.4]	—	0 [0; 0]	0.2 [0.2; 0.3]	0.3 [0.2; 0.4]
180°	0 [-0.1; 0.1]	-0.1 [-0.1; -0.1]	—	0 [-0.1; 0.1]	-0.1 [-0.1; 0]	0 [-0.1; 0]	—	0.1 [0; 0.1]
270°	—	-0.1 [-0.3; -0.1]	0.3 [0.2; 0.3]	0.1 [0; 0.2]	—	-0.1 [-0.2; 0.1]	0.2 [0.2; 0.3]	0.1 [0.1; 0.2]

Note: For each gantry angle, only two of three directions are shown as the information reported by MV portal image positioning is in 2D.

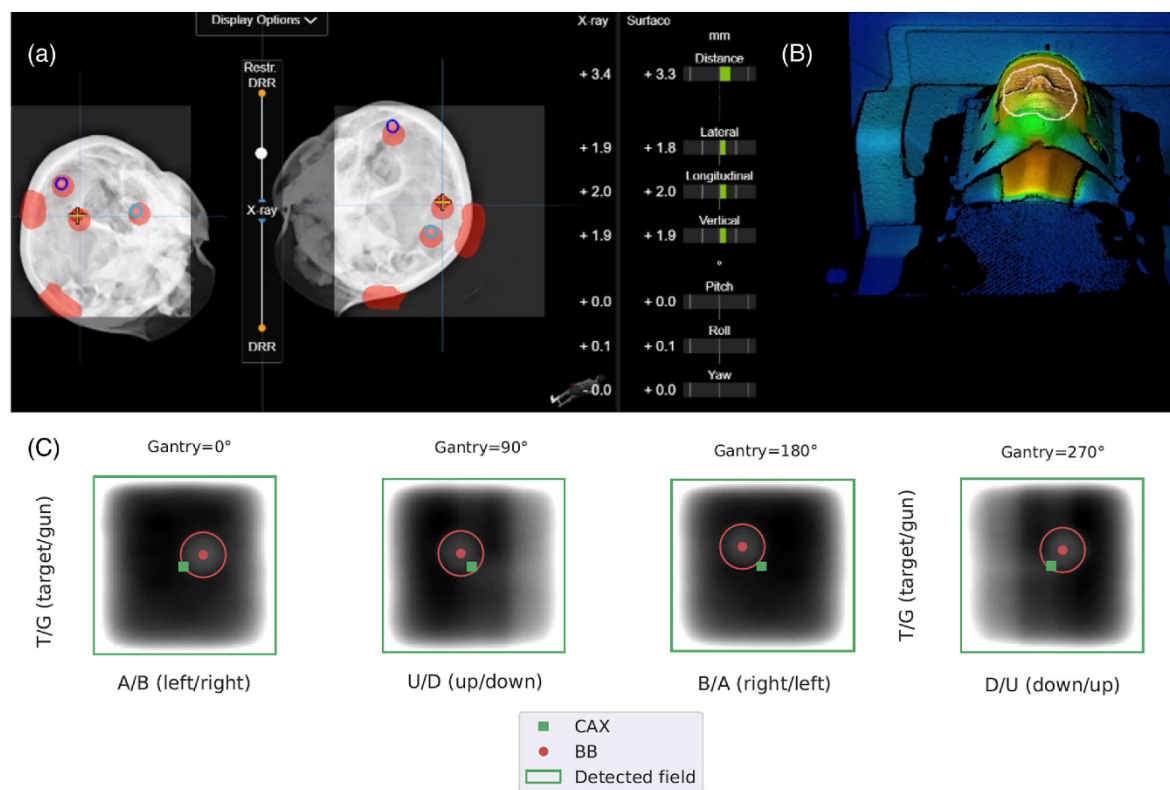


**FIGURE 7** Different methods of monitoring the phantom's position: (a) stereoscopic X-ray imaging and (b) optical/thermal imaging. The values in the center indicate the distance from the planned and the current position of the phantom provided by both systems; (c) EPID images processed with Pylinac, indicating the irradiated  $2 \times 2\text{-cm}^2$  MV beam from all four gantry angles, the MV beam center (CAX), and the position of the detected BB

**TABLE 4** Residual difference (median and IQR) between image-guided radiotherapy (IGRT)-aligned isocenter (BB's center) and MV radiation field center (median and IQR), in a  $2 \times 2$ -cm<sup>2</sup> field (25 MU, 6-MV photons)

Gantry angle	0°		90°		180°		270°	
	$\Delta d_{WL,X}$ (mm)	$\Delta d_{WL,Y}$ (mm)	$\Delta d_{WL,Z}$ (mm)	$\Delta d_{WL,Y}$ (mm)	$\Delta d_{WL,X}$ (mm)	$\Delta d_{WL,Y}$ (mm)	$\Delta d_{WL,Z}$ (mm)	$\Delta d_{WL,Y}$ (mm)
Median	0	0.4	0.2	0.2	0	−0.7	0	0.2
IQR	[−0.2; 0.2]	[0.2; 0.5]	[0; 0.2]	[0; 0.2]	[0; 0.2]	[−0.7; −0.5]	[−0.1; 0.2]	[0; 0.2]

Note: Results representing 40 IGRT-positioned phantom exposures, acquired throughout 1 year.

**TABLE 5** Difference between the positioning values reported by optical/thermal- and stereoscopic X-ray imaging monitoring: Mean values for all translations and rotations over 806 recorded values, with the corresponding standard deviations, standard errors of mean, and 95% confidence intervals

	Mean	Standard deviation	Standard errors of mean	95% Confidence interval
$\Delta d_{PAT,X}$ (mm)	0.02	0.35	0.01	[−0.01; 0.04]
$\Delta d_{PAT,Y}$ (mm)	0	0.35	0.01	[−0.02; 0.02]
$\Delta d_{PAT,Z}$ (mm)	0	0.40	0.01	[−0.03; 0.03]
$\Delta d_{PAT,PITCH}$ (°)	0	0.10	0	[0; 0.01]
$\Delta d_{PAT,ROLL}$ (°)	0	0.08	0	[−0.01; 0]
$\Delta d_{PAT,YAW}$ (°)	0	0.09	0	[0; 0.01]

#### Couch rotation

The four applied couch displacements, in the lateral ( $s_X$ ) and longitudinal ( $s_Y$ ) directions, and the differences between the positioning values, reported by optical/thermal- and stereoscopic X-ray imaging, respectively, and the displacement of the BB center from the MV beam center (Equations 4 and 5), are shown in Table S3. The maximal displacement observed was for couch angle 315°, for both imaging modalities, compared to MV portal imaging, in the lateral direction:  $\Delta d_{MV-IGRT,ST,X}$  reached 0.7 mm, whereas  $\Delta d_{MV-IGRT,Xray,X}$  was 0.6 mm. Nevertheless, the 3D displacement was always below 1-mm difference for all the measurements.

#### 3.2.4 | Hidden target test

The median differences between the BB center and the MV beam center, as well as the IQR for all 40 measurements, are shown in Table 4. The median differences in all directions did not exceed −0.7 mm, observed in the longitudinal direction for a gantry angle 180°. However, considering the same direction, a difference of 0.4 mm was found for gantry angle 0. In the lateral direction, the median difference was 0 mm, whereas in the vertical direction, the median did not exceed 0.2 mm. The magnitude of the range of the differences was not higher than 0.4 mm.

#### 3.2.5 | End-to-end IGRT test

The median differences and the IQR range are shown in Table S4. The resulting values are in submillimeter range and agreed with the ones shown in Table 4.

#### 3.3 | Patient data

The differences between optical/thermal- and stereoscopic X-ray imaging positioning values are shown in Table 5. The mean of the differences was close to 0 in all directions and the standard deviation always below 0.5 mm for translations and below 0.5° for rotations.

### 4 | DISCUSSION

The deviations between CBCT and EXTD positioning systems were found to be in the submillimeter range. Furthermore, both systems proved to be stable over time as experiments repeated 10 months later showed similar results with differences below 1 mm. Due to the regular and independent recalibration of the IGRT isocenters to the radiation isocenter and the inherent uncertainty, they could not be exactly the same. As SRS treatments are performed at this machine, the tolerated deviation between imaging and radiation isocenters

is less than 1 mm and therefore the maximal difference between both imaging isocenters could be up to 2 mm. Li et al.<sup>5</sup> performed a very similar study using a head phantom and 10 isocenter locations, where the absolute differences in the calculated couch residual errors between ExacTrac X-ray imaging registration and TrueBeam CBCT (Varian Medical Systems, Palo Alto, CA) imaging registration in translational and rotational directions were analyzed, and average residual error differences were found to be <0.5 mm and <0.4°, which agrees with our results. Zollner et al. also investigated the discrepancies between ExacTrac X-ray and CBCT (Elekta AB, Stockholm, Sweden) imaging positioning for a head phantom, as well as for patients.<sup>40</sup> They reported median differences below 0.5 mm for all translations, which is similar to our findings. Kim et al. compared the positional accuracy of ExacTrac and on-board CBCT (Varian Medical Systems, Palo Alto, CA) using a pelvic phantom.<sup>4</sup> The differences for the translational directions were slightly larger compared to our results, nonetheless comparable and in the range of 1 mm. A similar study with both cranial and pelvis phantoms was performed by Chow et al. to investigate the positional differences detected by EXT D X-ray and CBCT (Varian) imaging, and comparable results were reported (deviations <0.6 mm and <0.6°).<sup>26</sup>

To assess the influence of the thermal imaging, several tests with phantoms at different temperatures were performed. Spatial drift was investigated over 70 min, for both warm and cold surfaces, after disabling the blue projector light for 30 min. The deviations were higher for a cold surface, reaching ~0.8 mm, as opposed to 0.4 mm for a warm surface, which suggests a benefit when a patient-like temperature is present. The largest deviations were observed in the longitudinal direction for both cases. Possible reasons for this finding may be the cylindrically symmetric surface of the abdominal region<sup>26,41</sup> or the lower resolution of the CT scan of this phantom in the longitudinal. However, more measurements are necessary to determine if there is a permanent tendency for larger discrepancies in the longitudinal direction. Lehmann et al. conducted a similar study on system drift for the C-Rad Catalyst HD system and reported drifts with a magnitude between 0.7 and 1 mm, comparable to our results for a cold surface.<sup>42</sup>

The investigation of the stability of the optical/thermal positioning values during the delivery of a VMAT plan on a cold and a warm head phantom showed very similar values in all DoFs for both temperature levels. The statistical test indicated significant differences for the lateral and vertical translations as well as for pitch and yaw, between a cold and a warm phantom. The discrepancy was however below 0.08 mm and 0.05°. It should, moreover, be noted that when patients with intracranial tumors receive RT treatment, stereoscopic X-rays are

performed every 90° gantry rotation, and consequently a new optical/thermal imaging reference is taken. In this case, an eventual surface temperature change would not influence the optical/thermal values because they are being constantly recalibrated. As in our experiment optical/thermal positioning values were recorded continuously during 12 min, the reference was thus never updated.

The correlation between optical/thermal- and stereoscopic X-ray imaging positioning values was also investigated. For the head phantom (cold and warm surface), a similar performance was observed with maximal deviations of 0.4 mm and no significant difference between both temperature levels regarding the distribution of the differences between optical/thermal- and X-ray imaging positioning values ( $p > 0.05$ ). Repeated measurements produced similar results. When investigating different couch angles, the maximal deviation was also 0.4 mm, and no significant difference between positioning values for couch 0° and noncoplanar couch angles was found ( $p > 0.05$ ). For the abdominothoracic phantom, the median differences for both surface temperatures were very similar and below 0.2 mm. The largest deviations were observed in the longitudinal direction. However, no significant difference between a cold and a warm surface was found ( $p > 0.05$ ). All these results led to the conclusion that there is a good agreement between optical/thermal- and X-ray imaging. As it was not possible to switch off the thermal camera while performing the measurements with a cold surface, for the cold surface thermal information was also considered. This could be one of the reasons why no significant differences were found between a cold and a warm surface ( $p > 0.05$ ). Another investigation to determine the effectiveness of optical/thermal imaging as an image guidance tool was carried out, claiming that the thermal camera was able to detect surface deviations when a warm surface was present.<sup>43</sup>

The geometric congruence between the IGRT-derived isocenter and the radiation isocenter, for coplanar and noncoplanar treatments, was also tested, using the head phantom with a warm surface, simulating an SRS treatment. For all couch angles, the differences for both imaging positioning modalities in comparison to MV portal imaging positioning were comparable, always within the submillimeter range. Arp and Carl performed a similar study where the deviation between the linac radiation isocenter and the ExacTrac X-ray isocenter was investigated.<sup>44</sup> The reported deviations were slightly higher, in the range from 0.31 to 1.07 mm, but still in good agreement with ours. Huang et al. performed several tests to estimate the targeting accuracy when using image guidance with ExacTrac X-ray for coplanar and noncoplanar couch angles, with results also consistent with ours, with an overall deviation of  $0.5 \pm 0.1$  mm.<sup>45</sup>

A good agreement between the IGRT-aligned isocenter and the radiation isocenter was found while analyzing the hidden target tests, as well as the end-to-end IGRT test, as the differences between both isocenters did not exceed 0.7 mm. The largest discrepancy was found in the longitudinal direction for gantry angle 180°, with a median difference of −0.7 mm, in contrast to gantry 0°, for which a discrepancy of 0.4 mm was observed. This difference can be attributed to the gantry sag of this specific linac, which is known to be ~1 mm.

It is important to mention that regarding the skin tone, an adjustment for every patient/phantom individually is possible. This setting is used as an additional information for surface reconstruction. In our experiments, several phantoms with different surface tones were used, and the settings were adjusted accordingly. During our experiments, however, no difference between skin tones was detected in the matter of surface reconstruction, although we did not aim to evaluate this aspect.

The patient study took intra-fraction motion into account and compared the position of the patient during treatment with the planned position, with both optical/thermal- and stereoscopic X-ray imaging information. It aimed to investigate and compare the constant monitoring capability of the SGRT system with the stereoscopic X-ray imaging. Values from both systems are in good agreement, as the difference between stereoscopic X-ray and optical/thermal imaging was very close to 0 in all translational directions and below 0.5° for rotations.

This study investigated the geometric accuracy of EXT-D and its IGRT components under different initial setup conditions, using phantoms representing different anatomical regions with different amounts of visible bony anatomy information on the X-ray images. The magnitude of the displacements between all systems, reported in this study, was within the submillimeter range. This suggests that the image guidance provided by EXT-D is accurate at any couch angle, and therefore relevant dosimetric differences in surrounding critical structures and target coverage during the treatment of a patient are not expected.

Additionally, the patient study demonstrated good agreement between the monitoring values of both imaging systems, already demonstrated by our phantom measurements. These findings suggest that the optical/thermal positioning system can be an efficient tool for detecting intra-fractional motion during therapy.

However, only rigid anthropomorphic phantoms with a fixed relationship between the surface as a surrogate for tumor position and the isocenter were used. This can be considered a limitation of this study, especially in the thoracic and abdominal region, where surface deformation, due to patient organ motion, is clinically observable. Furthermore, results from a larger patient cohort as well as an extension to other treatment sites should also be considered in future investigations.

## 5 | CONCLUSIONS

In our institution, CBCT represents the benchmark for patient positioning. EXT-D showed to be in close agreement within 0.4 mm with CBCT and is therefore considered a legitimate alternative in specific indications. This is mostly true in cases where positioning relies only on bony structures, and for which patient setup can be accelerated. Especially for treatments with noncoplanar angles, where no CBCT acquisition is possible, the EXT-D system presents an advantage. The optical/thermal- and stereoscopic X-ray imaging were found to be in agreement with a maximal deviation of 0.4 mm. When comparing optical/thermal- and stereoscopic X-ray imaging with MV portal imaging positioning, the differences were not larger than 0.7 and 0.6 mm respectively. This study showed that EXT-D with its new optical/thermal imaging system is an efficient tool for positioning and monitoring during RT.

## ACKNOWLEDGMENTS

The authors would like to thank Michael Eder, Matthias Söhn, Christian Thieke, and Brainlab AG for their assistance during this project.

Open access funding enabled and organized by Projekt DEAL.

## CONFLICT OF INTEREST

The Department of Radiation Oncology of the University Hospital of LMU Munich has research agreements with Elekta, Inc. and Brainlab AG. SC, MN, and PF received speaker honoraria/travel support by Brainlab. PF is currently employed by Brainlab AG. However, at the time of the conception of the article and the analysis of the results, PF was not employed by Brainlab AG. PF declares that his employment had no influence on the study design, the collection, analysis or interpretation of data, on the writing of the manuscript or the decision to submit the manuscript for publication.

## AUTHOR CONTRIBUTIONS

Vanessa Da Silva Mendes and Philipp Freisleder performed the measurements and analysis of data, performed the statistical analysis, and drafted the manuscript. Lili Huang and Katrin Straub assisted in the analysis, reviewed the manuscript, and helped to finalize it. Maximilian Niyazi, Stefanie Corradini, and Daniel Reitz assisted in clinical data collection, reviewed the manuscript, and helped to finalize it. Michael Reiner, Guillaume Landry, Christopher Kurz, and Philipp Freisleder helped design the study, supervised the analysis, reviewed the manuscript, and helped finalize it. Claus Belka, Maximilian Niyazi, and Stefanie Corradini conceived the study, supervised the analysis, reviewed the manuscript, and helped to finalize it. All authors read and approved the final manuscript.



## REFERENCES

- Manger RP, Paxton AB, Pawlicki T, Kim G-Y. Failure mode and effects analysis and fault tree analysis of surface image guided cranial radiosurgery. *Med Phys*. 2015;42(5):2449-2461.
- Dang A, Kupelian PA, Cao M, Agazaryan N, Kishan AU. Image-guided radiotherapy for prostate cancer. *Transl Androl Urol*. 2018;7(3):308-320.
- Sterzing F, Engenhart-Cabillic R, Flentje M, Debus J. Image-guided radiotherapy: a new dimension in radiation oncology. *Dtsch Arztebl Int*. 2011;108(16):274-280.
- Kim J, Jin J-Y, Walls N, et al. Image-guided localization accuracy of stereoscopic planar and volumetric imaging methods for stereotactic radiation surgery and stereotactic body radiation therapy: a phantom study. *Int J Radiat Oncol Biol Phys*. 2011;79(5):1588-1596.
- Li J, Shi W, Andrews D, et al. Comparison of online 6 degree-of-freedom image registration of varian TrueBeam cone-beam CT and BrainLab ExacTrac X-ray for intracranial radiosurgery. *Technol Cancer Res Treat*. 2017;16(3):339-343.
- Hamada K, Fujibuchi T, Yoshida N, Ohura H. Examination of a dose evaluation method for floor-mounted kV X-ray image-guided radiation therapy systems. *Radiol Phys Technol*. 2020;13(3):288-295.
- Ma J, Chang Z, Wang Z, Jackie Wu Q, Kirkpatrick JP, Yin F-F. ExacTrac X-ray 6 degree-of-freedom image-guidance for intracranial non-invasive stereotactic radiotherapy: comparison with kilo-voltage cone-beam CT. *Radiother Oncol*. 2009;93(3):602-608.
- Kügele M, Mannerberg A, Bekke SN, et al. Surface guided radiotherapy (SGRT) improves breast cancer patient setup accuracy. *J Appl Clin Med Phys*. 2019;20(9):61-68.
- Rusu I, Thomas TO, Roeske JC, Mescioglou I, Melian E, Surucu M. Failure mode and effects analysis of linac-based liver stereotactic body radiotherapy. *Med Phys*. 2020;47(3):937-947.
- Lau SKM, Patel K, Kim T, et al. Clinical efficacy and safety of surface imaging guided radiosurgery (SIG-RS) in the treatment of benign skull base tumors. *J Neurooncol*. 2017;132(2):307-312.
- Zhao B, Maquilian G, Jiang S, Schwartz DL. Minimal mask immobilization with optical surface guidance for head and neck radiotherapy. *J Appl Clin Med Phys*. 2018;19(1):17-24.
- Ma Z, Zhang W, Su Y, et al. Optical surface management system for patient positioning in interfractional breast cancer radiotherapy. *Biomed Res Int*. 2018;2018:1.
- Freisleder P, Kügele M, Öllers M, et al. Recent advances in surface guided radiation therapy. *Radiat Oncol*. 2020;15(1):187.
- Hombrock G, Promberger C, Germany BA. Accessed July 1, 2021. [https://potential-and-challenges-of-sgrt\\_brainlab.pdf](https://potential-and-challenges-of-sgrt_brainlab.pdf)
- Swinnen ACC, Öllers MC, Loon Ong C, Verhaegen F. The potential of an optical surface tracking system in non-coplanar single isocenter treatments of multiple brain metastases. *J Appl Clin Med Phys*. 2020;21(6):63-72.
- Graulieres E, Kubler S, Martin E, Ferrand RG. Positioning accuracy of a single-isocenter multiple targets SRS treatment: a comparison between Varian TrueBeam CBCT and Brainlab ExacTrac. *Physica Med*. 2020;80:267-273.
- Gao J, Liu X. Winston-Lutz-Gao test on the True Beam STx linear accelerator. *Int J Med Phys, Clin Eng Radiat Oncol*. 2019;08: 9-20.
- Wen N, Snyder KC, Scheib SG, et al. Technical Note: Evaluation of the systematic accuracy of a frameless, multiple image modality guided, linear accelerator based stereotactic radiosurgery system. *Med Phys*. 2016;43(5):2527.
- Jin J-Y, Ryu S, Faber K, et al. 2D/3D image fusion for accurate target localization and evaluation of a mask based stereotactic system in fractionated stereotactic radiotherapy of cranial lesions. *Med Phys*. 2006;33(12):4557-4566.
- Gevaert T, Verellen D, Tournel K, et al. Setup accuracy of the Novalis ExacTrac 6DOF system for frameless radiosurgery. *Int J Radiat Oncol Biol Phys*. 2011;82:1627-1635.
- Takakura T, Mizowaki T, Nakata M, et al. The geometric accuracy of frameless stereotactic radiosurgery using a 6D robotic couch system. *Phys Med Biol*. 2010;55(1):1-10.
- Koubuchi S, Takakura T, Nakamura M, Mizowaki T, Nakata M, Hiraoka M. Accuracy of positional correction for the floor-mounted kV X-ray IGRT system in angled couch positions. *Radiol Phys Technol*. 2014;7(2):373-378.
- Pazos M, Walter F, Reitz D, et al. Impact of surface-guided positioning on the use of portal imaging and initial set-up duration in breast cancer patients. *Strahlenther Onkol*. 2019;195(11):964-971.
- Carl G, Reitz D, Schönecker S, et al. Optical surface scanning for patient positioning in radiation therapy: a prospective analysis of 1902 fractions. *Technol Cancer Res Treat*. 2018;17:153303381880600.
- Reitz D, Carl G, Schönecker S, et al. Real-time intra-fraction motion management in breast cancer radiotherapy: analysis of 2028 treatment sessions. *Radiat Oncol*. 2018;13(1): 128.
- Chow VUY, Cheung MLM, Kan MWK, Chan ATC. Shift detection discrepancy between ExacTrac Dynamic system and cone-beam computed tomography. *J Appl Clin Med Phys*. 2022;23(5): e13567.
- Willoughby T, Lehmann J, Bencomo JA, et al. Quality assurance for nonradiographic radiotherapy localization and positioning systems: report of Task Group 147. *Med Phys*. 2012;39(4):1728-1747.
- Schmitt D, Blanck O, Gauer T, et al. Technological quality requirements for stereotactic radiotherapy: expert review group consensus from the DGMP Working Group for Physics and Technology in Stereotactic Radiotherapy. *Strahlenther Onkol*. 2020;196(5):421-443.
- Jin J-Y, Yin F-F, Tenn SE, Medin PM, Solberg TD. Use of the BrainLAB ExacTrac X-Ray 6D system in image-guided radiotherapy. *Med Dosim*. 2008;33(2):124-134.
- Germany BA. Brainlab ExacTrac Dynamic – Clinical User Guide. Vol. Revision 1.1. 2020.
- Ackerly T, Lancaster CM, Geso M, Roxby KJ. Clinical accuracy of ExacTrac intracranial frameless stereotactic system. *Med Phys*. 2011;38(9):5040-5048.
- Company MI-E. Bedienungsanleitung (zur Verwendung mit digitalen Elekta Linearbeschleunigern) – HexaPOD evo RT system, M.I.-a.E. Company, Editor. 2008.
- Solberg TD, Balter JM, Benedict SH, et al. Quality and safety considerations in stereotactic radiosurgery and stereotactic body radiation therapy. Supplemental material. *Pract Radiat Oncol*. 2011:1-49.
- Solberg TD, Balter JM, Benedict SH, et al. Quality and safety considerations in stereotactic radiosurgery and stereotactic body radiation therapy: executive summary. *Pract Radiat Oncol*. 2012;2(1):2-9.
- Klein EE, Hanley J, Bayouth J, et al. Task Group 142 report: quality assurance of medical accelerators. *Med Phys*. 2009;36(9):4197-4212.
- Benedict SH, Yenice KM, Followill D, et al. Stereotactic body radiation therapy: the report of AAPM Task Group 101. *Med Phys*. 2010;37(8):4078-4101.
- Al-Hallaq HA, Cerviño L, Gutierrez AN, et al. AAPM task group report 302: surface-guided radiotherapy. *Med Phys*. 2022;49(4):e82-e112.
- Zaila A, Adili M, Bamajboor S. Pylina: a toolkit for performing TG-142 QA related tasks on linear accelerator. *Physica Med*. 2016;32:292-293.

39. Pylinac Full scale analysis. Accessed October 20, 2021. Available from: <https://pylinac.readthedocs.io/en/stable/overview.html>
40. Zollner B, Heinz C, Pitzler S, et al. Stereoscopic X-ray imaging, cone beam CT, and couch positioning in stereotactic radiotherapy of intracranial tumors: preliminary results from a cross-modality pilot installation. *Radiat Oncol*. 2016;11(1):158.
41. Kojima H, Takemura A, Kurokawa S, et al. Evaluation of technical performance of optical surface imaging system using conventional and novel stereotactic radiosurgery algorithms. *J Appl Clin Med Phys*. 2021;22(2):58-68.
42. Lehmann J, Standen TS, Kaur G, Wolf J, Wilfert A, Simpson J. Methodology of thermal drift measurements for surface guided radiation therapy systems and clinical impact assessment illustrated on the C-Rad Catalyst+ HD system. *Techn Innov Patient Support Radiat Oncol*. 2022;21:58-63.
43. E K Horgan LKW, Noble C, Ramachandran P. Commissioning Brainlab's ExacTrac Dynamic X-ray & 4D thermal-surface imaging system. 2021.
44. Tideman Arp D, Carl J. EXACTRAC x-ray and beam isocenters-what's the difference?. *Med Phys*. 2012;39(3):1418-1423.
45. Huang Y, Zhao B, Kim J, Wen N, Chetty IJ, Siddiqui S. Targeting accuracy at couch kick for a frameless image guided radiosurgery system. *J Radiosurg SBRT*. 2018;5(2):123-129.

#### SUPPORTING INFORMATION

Additional supporting information can be found online in the Supporting Information section at the end of this article.

**How to cite this article:** Da Silva Mendes V, Reiner M, Huang L, et al. ExacTrac Dynamic workflow evaluation: Combined surface optical/thermal imaging and X-ray positioning. *J Appl Clin Med Phys*. 2022;e13754. <https://doi.org/10.1002/acm2.13754>



## 7. Conclusions

The term “radiotherapy” was first introduced in 1903 and since then this field has developed steadily, becoming indispensable in the treatment of cancers [24]. Besides treating tumours by sterilising the tumour cells, radiotherapy also aims to spare the surrounding normal tissues from the damaging effects of the ionising radiation. In order to achieve a precise and accurate treatment delivery several techniques, such as IGRT, have been developed and continuously improved. IGRT provides information that enables the detection and adjustment of patient positioning, patient movement, organ motion and organ variations during therapy, allowing the reduction of the treatment margins without compromising the clinical output.

The Viewray MRIdian MR-linac and the ExacTrac Dynamic were the two systems of interest in the current work and while both represent good examples of innovative clinical technology, they also integrate different IGRT strategies with complex sub-systems. There is the need to investigate these systems individually as well as a whole, in order to guarantee a precise and accurate delivery of a radiotherapy treatment, and this was the goal of this work.

In our first project the evaluation and comparison of the performance of IMRT and VMAT plans was performed. While the VMAT plans were clinical linac-based plans, the IMRT plans were planned in the MRIdian TPS to be delivered at a low-field strength MR-guided linac [12]. The comparison study showed that, when applying the same PTV margins, the low-field strength MR-guided linac system is capable of delivering clinically equivalent prostate cancer treatment plans, with a comparable quality as VMAT plans, planned to be delivered in a conventional linac [12]. Additionally, due to the possibility of online ionising radiation-free image guidance, the irradiated volume can be reduced at the MR-linac, allowing for the delivery of less dose to the surrounding OARs and normal tissue, thus facilitating a better sparing [12].

Since it is still a relatively new technique, there are several other studies that can be performed to further investigate the performance of MRgRT, such as the investigation of the dose accumulation when a patient is treated in an MR-linac. The dose distribution, accumulated over several fractions or the whole treatment can be then also compared to the dose distribution originated by a conventional VMAT treatment plan, when using the same image dataset.

Regarding our second project, the performance of the EXT-D system in terms of positioning accuracy was investigated, including evaluations at the level of the different subcomponents. This study demonstrated that this system, combining two distinct imaging techniques, is an effective device for patient positioning and position monitoring during radiotherapy [88]. The EXT-D was in good agreement with the conventional positioning system, CBCT, and therefore considered a proper substitute in particular indications [88]. Furthermore, this system presents an advantage for treatments with non-coplanar angles, for which it is impossible to acquire a CBCT scan [88].

A limitation of our study was the use of rigid phantoms, which were not able to represent realistic body motion, for instance respiratory motion [88]. An investigation on how motion would affect



dose delivery, using a phantom that reproduces the respiratory motion, is important and is also being planned for the near future, as it resembles a more realistic situation [88].

Both studies and their findings showed the benefits brought by these two recently introduced clinical IGRT techniques. As a result, clinical workflows at the Department of Radiation Oncology of the LMU University Hospital were improved. A continuous collaboration between manufacturers and researchers is needed to further refine such systems, as well as further investigations in order to maximise the benefit of IGRT in daily routine.

## References

1. Bray, F., et al., *The ever-increasing importance of cancer as a leading cause of premature death worldwide*. 2021. **127**(16): p. 3029-3030.
2. World Health Organization (WHO). *Global Health Estimates 2020: Deaths by Cause, Age, Sex, by Country and by Region, 2000-2019*. 2020; Available from: <https://www.who.int/data/gho/data/themes/mortality-and-global-health-estimates/ghe-leading-causes-of-death>.
3. Ferlay, J., et al., *Estimating the global cancer incidence and mortality in 2018: GLOBOCAN sources and methods*. 2019. **144**(8): p. 1941-1953.
4. Charmsaz, S., et al., *Novel Strategies for Cancer Treatment: Highlights from the 55th IACR Annual Conference*. Cancers, 2019. **11**(8): p. 1125.
5. Khan, F.M., *Khan's Lectures - Handbook of the Physics of Radiation Therapy*. 2011.
6. Tejpal, G., et al., *IMRT and IGRT in head and neck cancer: Have we delivered what we promised?* Indian J Surg Oncol, 2010. **1**(2): p. 166-85.
7. Bortfeld, T. and C. Thieke, *Optimization of Treatment Plans, Inverse Planning*, in *New Technologies in Radiation Oncology*, W. Schlegel, T. Bortfeld, and A.-L. Grosu, Editors. 2006, Springer Berlin Heidelberg: Berlin, Heidelberg. p. 207-220.
8. Dang, A., et al., *Image-guided radiotherapy for prostate cancer*. Transl Androl Urol, 2018. **7**(3): p. 308-320.
9. Tetar, S.U., et al., *Clinical implementation of magnetic resonance imaging guided adaptive radiotherapy for localized prostate cancer*. Physics and Imaging in Radiation Oncology, 2019. **9**: p. 69-76.
10. Sterzing, F., et al., *Image-guided radiotherapy: a new dimension in radiation oncology*. Deutsches Arzteblatt international, 2011. **108**(16): p. 274-280.
11. Yan, D., et al., *Adaptive radiation therapy*. Phys Med Biol, 1997. **42**(1): p. 123-32.
12. Da Silva Mendes, V., et al., *Dosimetric comparison of MR-linac-based IMRT and conventional VMAT treatment plans for prostate cancer*. Radiation Oncology, 2021. **16**(1): p. 133.
13. Corradini, S., et al., *MR-guidance in clinical reality: current treatment challenges and future perspectives*. Radiation oncology (London, England), 2019. **14**(1): p. 92-92.
14. Freisleder, P., et al., *Characteristics of gated treatment using an optical surface imaging and gating system on an Elekta linac*. Radiation Oncology, 2015. **10**(1): p. 68.
15. Enmark, M., S. Korreman, and H. Nyström, *IGRT of prostate cancer; is the margin reduction gained from daily IG time-dependent?* Acta Oncologica, 2006. **45**(7): p. 907-914.
16. Mittauer, K., et al., *A New Era of Image Guidance with Magnetic Resonance-guided Radiation Therapy for Abdominal and Thoracic Malignancies*. Cureus, 2018. **10**(4): p. e2422.
17. Malika Ouzidane, J.E., Toufik Djemil, *Stereotactic Radiosurgery and Stereotactic Body Radiation*, in *Stereotactic Radiosurgery and Stereotactic Body Radiation*, D.J.S. Stanley H. Benedict, Steven J. Goetsch, Brian D. Kavanagh, Editor. 2015, CRC Press.
18. Kainz, E.B.P.K., *Radiation Oncology Physics: a Handbook for Teachers and Students*. Vol. 33. 2006, Vienna: INTERNATIONAL ATOMIC ENERGY AGENCY.
19. P. Mayles, A.N., J. C. Rosenwald, *Handbook of Radiotherapy Physics - Theory and Practice*. 2007: Taylor & Francis Group.
20. Krieger, H., *Grundlagen der Strahlungsphysik und des Strahlenschutzes*. 2012: Vieweg+Teubner Verlag.

21. Rogers, D.W.O. and R.W. Townson, *On calculating kerma, collision kerma and radiative yields*. 2019. **46**(11): p. 5173-5184.
22. Troeller, A., *Normal Tissue Complication Probability Modelling: Influence of Treatment Technique, Fractionation and Dose Calculation Algorithm*. 2016, Ludwig-Maximilians-Universität München. p. 137.
23. cherry, P., *Practical Radiotherapy Second Edition: Physics and Equipment*. Second Edition ed. 2009: Wiley-Blackwell.
24. Murat Beyzadeoglu, G.O., Cuneyt Ebruli *Basic Radiation Oncology*. 1 ed. 2010: Springer Berlin, Heidelberg.
25. Elekta. *Elekta Versa HDTM - Ultimate power and versatility*. 2017; Available from: [https://www.elekta.com/dam/jcr:14cae385-9b40-4f9b-a805-79a0ecff249e/LPCIYE170601\\_VHD\\_FLG\\_A4ls\\_f\\_revised\\_7.19.17.pdf](https://www.elekta.com/dam/jcr:14cae385-9b40-4f9b-a805-79a0ecff249e/LPCIYE170601_VHD_FLG_A4ls_f_revised_7.19.17.pdf).
26. Cosgrove, V., et al., *Physical characterisation of a new concept design of an Elekta radiation head with integrated 160-leaf multi-leaf collimator*. 2009.
27. Kantz, S., et al., *Impact of MLC properties and IMRT technique in meningioma and head-and-neck treatments*. *Radiat Oncol*, 2015. **10**: p. 184.
28. Bedford, J.L., M.D. Thomas, and G. Smyth, *Beam modeling and VMAT performance with the Agility 160-leaf multileaf collimator*. *J Appl Clin Med Phys*, 2013. **14**(2): p. 4136.
29. Elekta. *Elekta. Agility— Intelligent beam shaping.*; Available from: [https://www.elekta.com/dms/elekta/Elekta-Oncology/treatment-techniques/Beam-Shaping/brochures/Agility\\_Brochure\\_0933\\_03-12/Agility%E2%84%A2%20brochure%20\\_Intelligence%20beam%20shaping.pdf](https://www.elekta.com/dms/elekta/Elekta-Oncology/treatment-techniques/Beam-Shaping/brochures/Agility_Brochure_0933_03-12/Agility%E2%84%A2%20brochure%20_Intelligence%20beam%20shaping.pdf).
30. Viewray, *Physics Essentials Guide: Technical Manual for the MRIdian linac system*, in *ViewRay Technical Manual L-0092 Rev B*. 2019.
31. Klüter, S., *Technical design and concept of a 0.35 T MR-Linac*. *Clinical and Translational Radiation Oncology*, 2019. **18**: p. 98-101.
32. Viewray. *Media Kit*. [cited 2022; Available from: <https://viewray.com/media-kit/>].
33. W. Schlegel, T.B., A.-L. Grosu, *New Technologies in Radiation Oncology*. 2006: Springer Berlin Heidelberg New York.
34. Burnet, N.G., et al., *Defining the tumour and target volumes for radiotherapy*. *Cancer Imaging*, 2004. **4**(2): p. 153-61.
35. Thomas Bortfeld, R.S.-U., Wilfried De Neve, David E. Wazer, *Image-Guided IMRT*. 2006: Springer, Berlin, Heidelberg.
36. Center, M.o.t.s.o.M.S.-K.C., *A Practical Guide to Intensity-Modulated Radiation Therapy*. 2003: Medical Physics Publishing.
37. IAEA, I.A.E.A.-. *Transition from 2-D Radiotherapy to 3-D Conformal and Intensity Modulated Radiotherapy*. 2008, Vienna: INTERNATIONAL ATOMIC ENERGY AGENCY.
38. Teoh, M., et al., *Volumetric modulated arc therapy: a review of current literature and clinical use in practice*. *The British journal of radiology*, 2011. **84**(1007): p. 967-996.
39. Palma, D.A., et al., *New developments in arc radiation therapy: a review*. *Cancer Treat Rev*, 2010. **36**(5): p. 393-9.
40. Galvin, J.M., et al., *Implementing IMRT in clinical practice: a joint document of the American Society for Therapeutic Radiology and Oncology and the American Association of Physicists in Medicine*. *Int J Radiat Oncol Biol Phys*, 2004. **58**(5): p. 1616-34.
41. Hegemann, N.-S., et al., *Hypofractionated radiotherapy for prostate cancer*. *Radiation Oncology*, 2014. **9**(1): p. 275.
42. Jones, B., et al., *The Role of Biologically Effective Dose (BED) in Clinical Oncology*. *Clinical Oncology*, 2001. **13**(2): p. 71-81.

43. Fowler, J.F., *21 years of biologically effective dose*. Br J Radiol, 2010. **83**(991): p. 554-68.
44. Cahlon, O., et al., *Ultra-high dose (86.4 Gy) IMRT for localized prostate cancer: toxicity and biochemical outcomes*. Int J Radiat Oncol Biol Phys, 2008. **71**(2): p. 330-7.
45. Mahur, M., et al., *Evaluation of Effect of Different Computed Tomography Scanning Protocols on Hounsfield Unit and Its Impact on Dose Calculation by Treatment Planning System %J Iranian Journal of Medical Physics*. 2017. **14**(3): p. 149-154.
46. Schoknecht, G., *[The description of radiation fields by separation of primary and scattered radiation. 3. The tissue-air ratio and the depth dose course for gamma and x-ray radiations in the range of 0.6 to 42 Mev]*. Strahlentherapie, 1968. **136**(1): p. 24-32.
47. Fippel, M., *Fast Monte Carlo dose calculation for photon beams based on the VMC electron algorithm*. Med Phys, 1999. **26**(8): p. 1466-75.
48. Ahnesjö, A., *Collapsed cone convolution of radiant energy for photon dose calculation in heterogeneous media*. Med Phys, 1989. **16**(4): p. 577-92.
49. Chetty, I.J., et al., *Report of the AAPM Task Group No. 105: Issues associated with clinical implementation of Monte Carlo-based photon and electron external beam treatment planning*. Med Phys, 2007. **34**(12): p. 4818-53.
50. Liang, Y., et al., *A general-purpose Monte Carlo particle transport code based on inverse transform sampling for radiotherapy dose calculation*. Scientific Reports, 2020. **10**(1): p. 9808.
51. Jabbari, K., *Review of fast monte carlo codes for dose calculation in radiation therapy treatment planning*. Journal of medical signals and sensors, 2011. **1**(1): p. 73-86.
52. Reynaert, N., et al., *Monte Carlo treatment planning for photon and electron beams*. Radiation Physics and Chemistry, 2007. **76**(4): p. 643-686.
53. Schneider, W., T. Bortfeld, and W. Schlegel, *Correlation between CT numbers and tissue parameters needed for Monte Carlo simulations of clinical dose distributions*. Phys Med Biol, 2000. **45**(2): p. 459-78.
54. Nahum, A.E., *Condensed-history Monte-Carlo simulation for charged particles: what can it do for us?* Radiat Environ Biophys, 1999. **38**(3): p. 163-73.
55. Kawrakow, I. and M. Fippel. *VMC++, a fast MC algorithm for Radiation Treatment planning*. 2000. Berlin, Heidelberg: Springer Berlin Heidelberg.
56. Roche, M., et al., *Agility MLC transmission optimization in the Monaco treatment planning system*. Journal of applied clinical medical physics, 2018. **19**(5): p. 473-482.
57. W. Schlegel, A.M. *3D conformal radiation therapy: Multimedia Introduction to Methods and Techniques*. 2007.
58. Czajkowski, P. and T. Piotrowski, *Registration methods in radiotherapy*. Reports of Practical Oncology & Radiotherapy, 2019. **24**(1): p. 28-34.
59. Rabe, M., *Investigation of time-resolved volumetric MRI to enhance MR-guided radiotherapy of moving lung tumors*. 2021, Physics Faculty, LMU Munich: Munich, Germany.
60. Bushberg, J.T., *The essential physics of medical imaging*. Third edition ed. 2012, Philadelphia: Wolters Kluwer Health/Lippincott Williams & Wilkins.
61. Suetens, P., *Fundamentals of Medical Imaging*, in *Fundamentals of Medical Imaging*, P. Suetens, Editor. 2009, Cambridge University Press: Cambridge.
62. Schlegel, W. and J. Bille, *Medizinische Physik 2: Medizinische Strahlenphysik*. 2002.
63. Blink, E.J., *Basic MRI Physics*.
64. Wolfgang Schlegel, C.P.K., Oliver Jäkel, *Medizinische Physik: Grundlagen – Bildgebung – Therapie – Technik*. 2018: Springer Spektrum.
65. Sebastian Hirsch, J.B., Ingolf Sack, *Magnetic Resonance Elastography: Physical Background and Medical Applications*. 2017: Wiley-VCH Verlag GmbH.

66. Jones, D., *ICRU Report 50—Prescribing, Recording and Reporting Photon Beam Therapy*. 1994. **21**(6): p. 833-834.
67. Jaffray, D.A., *Image-guided radiotherapy: from current concept to future perspectives*. *Nature Reviews Clinical Oncology*, 2012. **9**(12): p. 688-699.
68. Glide-Hurst, C.K., et al., *Adaptive Radiation Therapy (ART) Strategies and Technical Considerations: A State of the ART Review From NRG Oncology*. *International Journal of Radiation Oncology\*Biography\*Physics*, 2021. **109**(4): p. 1054-1075.
69. De Los Santos, J., et al., *Image Guided Radiation Therapy (IGRT) Technologies for Radiation Therapy Localization and Delivery*. *International Journal of Radiation Oncology\*Biography\*Physics*, 2013. **87**(1): p. 33-45.
70. Goyal, S. and T. Kataria, *Image guidance in radiation therapy: techniques and applications*. *Radiol Res Pract*, 2014. **2014**: p. 705604.
71. Foroudi, F., et al., *Comparison of Margins, Integral Dose and Interfraction Target Coverage with Image-guided Radiotherapy Compared with Non-image-guided Radiotherapy for Bladder Cancer*. *Clinical Oncology*, 2014. **26**(8): p. 497-505.
72. Hunt, A., et al., *Adaptive Radiotherapy Enabled by MRI Guidance*. *Clinical Oncology*, 2018. **30**(11): p. 711-719.
73. Nierer, L., et al., *Dosimetric benefit of MR-guided online adaptive radiotherapy in different tumor entities: liver, lung, abdominal lymph nodes, pancreas and prostate*. *Radiat Oncol*, 2022. **17**(1): p. 53.
74. Henke, L., et al., *Phase I trial of stereotactic MR-guided online adaptive radiation therapy (SMART) for the treatment of oligometastatic or unresectable primary malignancies of the abdomen*. *Radiother Oncol*, 2018. **126**(3): p. 519-526.
75. El-Bared, N., et al., *Dosimetric Benefits and Practical Pitfalls of Daily Online Adaptive MRI-Guided Stereotactic Radiation Therapy for Pancreatic Cancer*. *Pract Radiat Oncol*, 2019. **9**(1): p. e46-e54.
76. Brown, J.M., D.J. Carlson, and D.J. Brenner, *The tumor radiobiology of SRS and SBRT: are more than the 5 Rs involved?* *International journal of radiation oncology, biology, physics*, 2014. **88**(2): p. 254-262.
77. Ma, C.-M., *Physics and Dosimetric Principles of SRS and SBRT*. *Mathews Journal of Cancer Science*, 2019. **4**.
78. Halvorsen, P.H., et al., *AAPM-RSS Medical Physics Practice Guideline 9.a. for SRS-SBRT*. 2017. **18**(5): p. 10-21.
79. Willoughby, T., et al., *Quality assurance for nonradiographic radiotherapy localization and positioning systems: Report of Task Group 147*. 2012. **39**(4): p. 1728-1747.
80. Al-Hallaq, H.A., et al., *AAPM task group report 302: Surface-guided radiotherapy*. 2022. **49**(4): p. e82-e112.
81. Mutic, S. and J.F. Dempsey, *The ViewRay System: Magnetic Resonance–Guided and Controlled Radiotherapy*. *Seminars in Radiation Oncology*, 2014. **24**(3): p. 196-199.
82. Green, O.L., et al., *First clinical implementation of real-time, real anatomy tracking and radiation beam control*. *Med Phys*, 2018.
83. Bieri, O. and K. Scheffler, *Fundamentals of balanced steady state free precession MRI*. *J Magn Reson Imaging*, 2013. **38**(1): p. 2-11.
84. Rankine, L.J., et al., *Three-Dimensional Dosimetric Validation of a Magnetic Resonance Guided Intensity Modulated Radiation Therapy System*. *Int J Radiat Oncol Biol Phys*, 2017. **97**(5): p. 1095-1104.
85. Thiyagarajan, R., et al., *Respiratory gated radiotherapy-pretreatment patient specific quality assurance*. *Journal of medical physics*, 2016. **41**(1): p. 65-70.
86. Germany, B.A., *Brainlab ExacTrac Dynamic - Clinical User Guide*. Vol. Revision 1.1. 2020.

87. Germany, B.A., G. Hombrink, and C. Promberger, <potential-and-challenges-of-sgrt\_brainlab.pdf>.
88. Da Silva Mendes, V., et al., *ExacTrac Dynamic workflow evaluation: Combined surface optical/thermal imaging and X-ray positioning*. 2022. **n/a**(n/a): p. e13754.
89. Germany, B.A. *ExacTrac Dynamic - Precision Patient Monitoring for Radiotherapy* [cited 2022 14.07.2022]; Available from: <https://www.brainlab.com/radiosurgery-products/exactrac/>.

## Acknowledgements

I would like to acknowledge and to express my special appreciation and gratitude to my primary supervisor, Prof. Guillaume Landry, without whom I would not be able to complete this research project. His guidance and feedback throughout this project and all valuable knowledge and advice were crucial. Additionally, I am grateful for having taken the time to read and correct all the different versions of my thesis and manuscripts.

I would also like to thank both Dr. Matthias Söhn and Dr. Christian Thieke for their insightful thoughts, meaningful questions, and kind support throughout the project.

This work would also not be possible without Dr. Michael Reiner, the Head of Physics of the Department of Radiation Oncology. I would like to thank him for sharing his vast knowledge, for all the help and for all creative solutions at the linac. Even a simple cup of warm water can be the key for a successful measurement.

I would like to acknowledge Dr. Christopher Kurz and Dr. Florian Kamp for their thorough ideas and suggestions and for all the time spent discussing this research project.

I am also thankful to Prof. Claus Belka, the Head of the Department of Radiation Oncology and Prof. Maximilian Niyazi for the opportunity to be part of this project and by all the support given.

All my former and current colleagues from the Medical Physics team at the Department of Radiation Oncology, working in our research group and in the clinic, were a very important part on this chapter of my life, with their great support, patience and all the laughs and jokes we shared during our coffee breaks. Specifically, I want to thank Dr. Philipp Freisleder, Roel Shpani, Amra Mekic-Krejovic, Jan Hofmaier, Lukas Nierer-Kohlhase, Dr. Daniel Reitz, Lili Huang, Winfried Hoischen, Robert Kießling, Dr. Sylvia Garny and Dr. Christoph Losert for their kind support, all the stimulating discussions, pushing me further than I thought I could go.

Moreover, I am grateful to all the physicians, therapists and other co-workers at the LMU, who have contributed to my thesis, for their assistance during this project.

On a more personal note, I would like to thank my closest friends who were there for me, wanting to help in any way possible, who encouraged me in pursuing my goals and helping me survive all the stress. A special thanks to Alexandra Conde, Joana Neves, Sara Vicente, Vânia Batista, Joel Oliveira, Nádia Correia and André Valente who were present in the most difficult and happy moments.

Last but not least, I would like to express my gratitude to my parents and family for the love, wise counsel and unconditional support.